

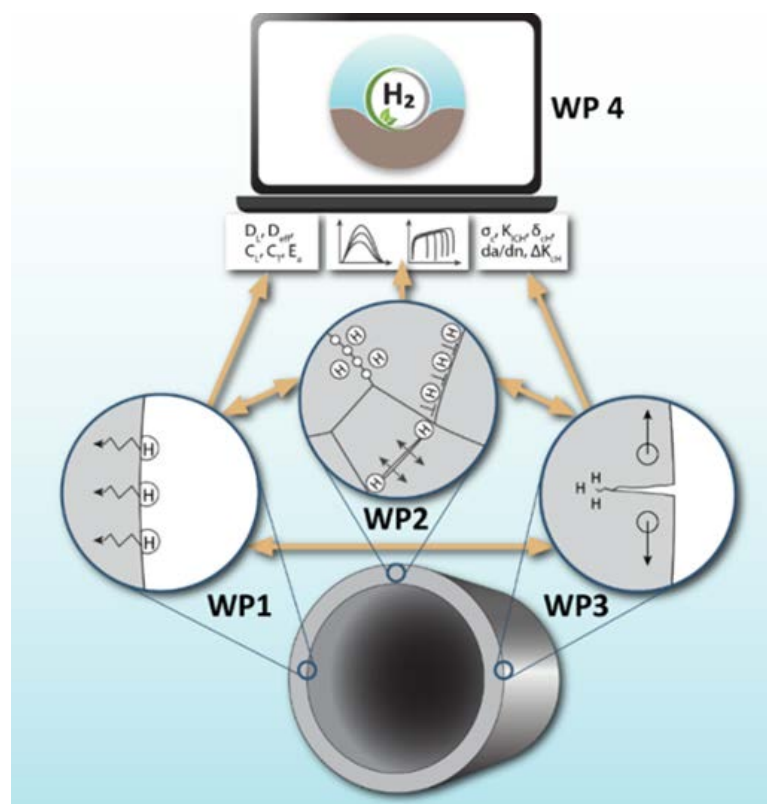
# Report

## Hydrogen Influence on Mechanical Properties in Pipeline Steel

State of the art

### Author(s)

Anette Brocks Hagen  
Antonio Alvaro



# Report

## Hydrogen Influence on Mechanical Properties in Pipeline Steel

State of the art

**KEYWORDS:**  
Pipeline steel  
Hydrogen  
embrittlement  
Hydrogen-affected  
fatigue  
Metallurgy

<b>VERSION</b>	<b>DATE</b>
1	2020-14-02

<b>AUTHOR(S)</b>
Anette Brocks Hagen Antonio Alvaro

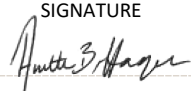
<b>CLIENT(S)</b>	<b>CLIENT'S REF.</b>
RCN, Gassco, Equinor, TechnipFMC, NEL, Air Liquide, Tenaris Dalmine	Andreas Bratland, RCN

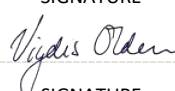
<b>PROJECT NO.</b>	<b>NUMBER OF PAGES/APPENDICES:</b>
102017484-5	111 + 1 appendix


### ABSTRACT

#### Hydrogen effect on pipeline steels

The state-of-the-art report consist of an overview and a summary of the mechanical behaviour of pipeline steels (in the range of X42-X70) when exposed to electrochemical charging and gaseous hydrogen environment. Experimental data from tensile-, fracture - and fatigue tests in air and hydrogen environment are addressed and presented in correlation with the identifications of the possible key mechanisms behind hydrogen embrittlement degradation. In addition, the effect of parameters such as metallurgy, temperature, pressure, gas composition and load conditions are included.

<b>PREPARED BY</b>	<b>SIGNATURE</b>
Anette Brock Hagen	

<b>CHECKED BY</b>	<b>SIGNATURE</b>
Vigdis Olden	

<b>APPROVED BY</b>	<b>SIGNATURE</b>
Magnus Eriksson	

<b>REPORT NO.</b>	<b>ISBN</b>	<b>CLASSIFICATION</b>	<b>CLASSIFICATION THIS PAGE</b>
2020:00130	978-82-14-06311-0	Unrestricted	Unrestricted

# Document history

---

VERSION	DATE	VERSION DESCRIPTION
1	2020-02-14	Complete draft report

## Table of contents

<b>1</b>	<b>Introduction .....</b>	<b>5</b>
1.1	Hydrogen Sources .....	8
1.2	Adsorption and Absorption.....	8
1.3	Transport.....	12
1.4	Trapping .....	14
1.5	Damage Mechanisms.....	17
<b>2</b>	<b>Materials and Metallurgy.....</b>	<b>19</b>
2.1	Classification of Pipeline Steel .....	19
2.2	Chemical Composition of Pipeline Steel .....	20
2.3	Microstructures in Pipeline Steels .....	21
2.3.1	Base Metal (BM) .....	21
2.3.2	Heat-Affected Zone (HAZ).....	25
<b>3</b>	<b>Test Methods for Hydrogen Embrittlement .....</b>	<b>26</b>
3.1	Electrochemical Hydrogen Charging.....	27
3.2	Gaseous Hydrogen Charging .....	28
<b>4</b>	<b>Tensile Properties.....</b>	<b>29</b>
4.1	Hydrogen Influence on Tensile Properties.....	29
4.2	Grain size Effect on Tensile Properties .....	33
4.3	Effect of Microstructure Banding.....	36
4.4	The role of Grain Boundary Character and Texture.....	37
4.5	Hydrogen Effect on HAZ Tensile Properties.....	39
<b>5</b>	<b>Fracture Mechanical Properties .....</b>	<b>42</b>
5.1	Fracture Toughness.....	42
5.2	The Influence of Microstructure .....	46
5.3	Effect of Current Density.....	48
5.4	Fracture Toughness in Welds and HAZ .....	50
5.5	Effect of Orientation .....	60
5.6	Effect of Inhibitors .....	62
<b>6</b>	<b>Fatigue Performance .....</b>	<b>69</b>
6.1	Fatigue Life .....	70
6.2	Short Cracks .....	72

6.3	Hydrogen Assisted Fatigue Crack Growth.....	73
6.3.1	Effect of Hydrogen Gas Pressure .....	76
6.3.2	Effect of Frequency.....	81
6.3.3	Effect of Stress Ratio.....	87
6.3.4	Effect of Microstructure and Yield Strength.....	91
6.3.5	Effect of Gas Composition .....	95
6.3.6	Effect of Temperature .....	96
6.3.7	FCGR of Pipeline HAZ.....	98
6.3.8	Representative FCGR Curves for Pipeline Steel.....	99
<b>A</b>	<b>Chemical composition of reviewed materials .....</b>	<b>101</b>
<b>7</b>	<b>Bibliography.....</b>	<b>102</b>

APPENDICES

---

---

## 1 Introduction

The Norwegian oil and gas pipeline subsea network are the main infrastructure for the transport of unprocessed oil and natural gas in Norway and Europe. Carbon manganese steels are attractive structural materials for these applications because of their weldability and formability in addition to their superior properties for normalizing heat treatments and rolling processes. Newer low carbon pipeline steels contain small additions of elements such as niobium and vanadium, that in combination with controlled rolling, provide high strength and increased fracture resistance at low temperatures. Despite excellent mechanical properties under normal operating conditions, the presence of hydrogen is known to degrade the mechanical properties in pipeline steels.

In a larger degree, hydrogen is foreseen as an alternative energy carrier and as a renewable energy storage medium at the utility level. When hydrogen is converted to electric energy in a fuel cell, it produces only a clean bi-product – pure water, which makes it an important agent to decarbonizing the worlds energy supply. Currently, hydrogen is becoming widely used in several industrial applications (petroleum refineries, fuel cells, power plants, etc.) and the demand is expected to increase. This highlights the importance of enabling safe, environmentally friendly and cost-efficient transportation of large quantities of hydrogen. Transporting gaseous hydrogen via existing pipelines is considered as the best low-cost option for a comprehensive and largescale use of hydrogen as an energy source.

Norway has an important role as an energy provider to the rest of Europe. On the Norwegian shelf, Gassco operates one of the world's most extensive and integrated transport systems for natural gas that consists of more than 8800 km of subsea natural gas pipelines, primarily made of carbon manganese steel with a strength grade typical SMYS 400 – 450 MPa . Recently, higher strength steels, up to 480 MPa (X70) have also been used, e.g. Europipe II, Langeled. The pipeline network is illustrated in Figure 1. Utilizing the existing natural gas piping systems for hydrogen transport is envisioned as a cost-efficient option, promoting the increase for production of renewable energy systems. However, most of the subsea pipelines on the Norwegian continental shelf are designed according to the code DNV-OS-F101, which does not address hydrogen transport service.

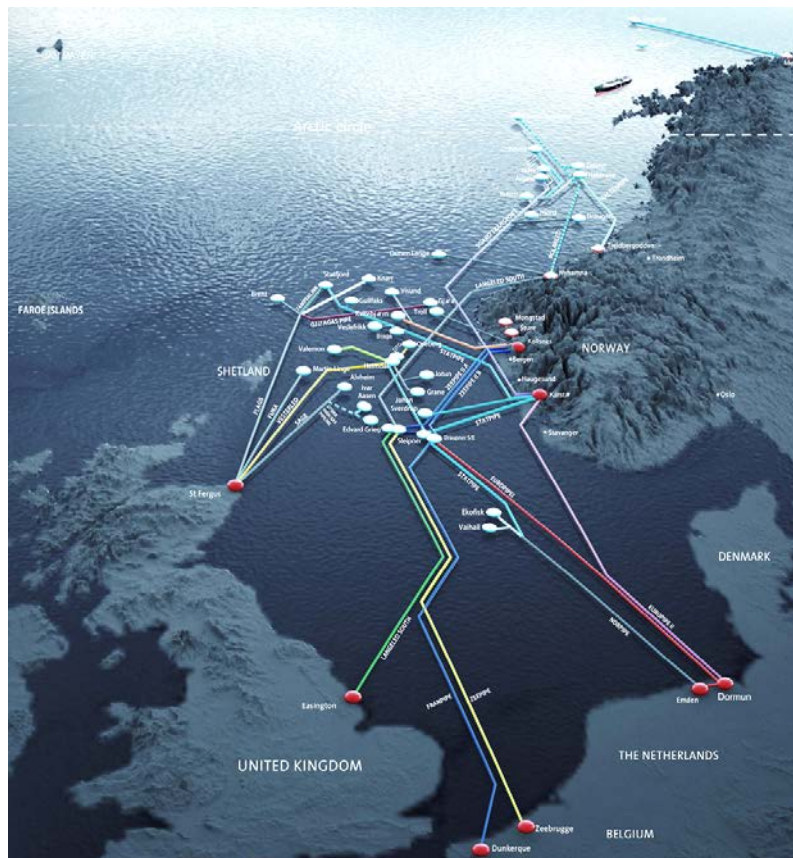


**Figure 1: The gas transport system from Norway to UK and Europe, including 8800 km of pipelines, platforms, processing plants and receiving terminals. The transport system is operated by Gassco.**

One of the key issues of transporting hydrogen in pipelines originally designed to transport natural gas is the hydrogen compatibility of the materials used. Moreover, transporting pressurized H<sub>2</sub> gas in the existing pipelines will introduce an additional source for hydrogen uptake. The pipelines are exposed to hydrogen from both aqueous solutions related to CP and dry low-pressure hydrogen gas inside the pipe. Hydrogen atoms can easily enter and diffuse into the lattice structure of the pipeline material due to its small size and can eventually result in the phenomenon recognized as "*hydrogen embrittlement*" (HE). Hydrogen embrittlement has a detrimental effect on the metallic mechanical properties mainly involving a loss in mechanical ductility, reduced fracture toughness and degradation of fatigue properties [1, 2]. This may lead to unexpected failures and considerable maintenance problems at loads significantly below the design load. Several metallic materials are susceptible to hydrogen embrittlement, particularly those with a body-centered cubic (bcc) structure, such as the ferritic steels (carbon steel, carbon manganese steel and low alloy steel) used in pipelines. The current report is therefore restricted to these materials.

In order to assess the technical feasibility of hydrogen transport through the existing offshore pipelines, typically three different microstructural zones, a base metal (BM), weld metal (WM) and a heat affected zone (HAZ), needs to be considered in terms of hydrogen susceptibility. The presence

of certain microstructural features can more easily promote hydrogen-induced failures. For example, harder phases such as martensite and bainite [3] or banded microstructures of pearlite [4]. Traditional ferritic steels consist of a microstructure with ferrite and pearlite. As a result of processing methods, harder phases, such as acicular ferrite and bainite can be present in the microstructure. Often, failure in pipelines are initiated at or close to the welds due to the presence of geometrical stress concentrators, weld defects, residual stresses and sensitive microstructure, particularly related to the HAZ. In particular, the HAZ is of great concern as the high peak temperature during welding results in extensive grain growth [5]. During cooling, transformation to microstructures (martensite and bainite) with a local reduced fracture toughness and high sensitivity to HE, occurs.

The presence of hydrogen in pipeline steels has proven to be a concern that has received a significant amount of attention over the last century. Nevertheless, no consensus has been reached when it comes to the existence of a unique underlying mechanism able to explain the phenomenon encouraging a great number of scientific works on this topic. Today, a comprehensive list of publications concerning hydrogen embrittlement in ferritic steels is available. Current knowledge and findings of hydrogen embrittlement in ferritic steels will be addressed in this State of the art-report, including the identifications of the key mechanisms that lead to HE, discussed in correlation with mechanical properties, fracture, and fatigue behaviour.

*Chapter 1 include the theoretical principles of a source, absorption, transportation and trapping of hydrogen in metallic materials. The chapter also briefly presents the latest theories and models of hydrogen embrittlement (HELP, HEDE; AIDE).*

*Chapter 2 presents the classification of pipeline steel and consider the microstructural features for base metal, weld metal and heat-affected zones for low carbon pipeline steels relevant for this study, i.e. X42-X70. Materials, microstructures and chemical compositions are accounted for and described.*

*Chapter 3 introduce some experimental procedures and relevant test methods used for investigation hydrogen embrittlement in metallic materials.*

*Chapter 4, 5 and 6 summarizes experimental results from the open literature of hydrogen influence on the tensile, fracture and fatigue properties of the relevant pipeline materials.*



## 1.1 Hydrogen Sources

Hydrogen can enter metals through the manufacturing and fabrication processes, direct exposure to hydrogen from storage of gaseous hydrogen or hydrogenated gas mixtures, cathodic protection and corrosion processes [6]. The major source of hydrogen in subsea pipelines are molecular water reduction from cathodic protection (CP). As the sacrificial anode corrodes, a reduction process occurs at the protected pipe material by means of oxygen and hydrogen reduction as shown in eq.1 and eq. 2 [7].



The water dissociation in eq.2 leads to the formation of hydrogen that surrounds the protected material. The hydrogen may either recombine and desorb from the surface as hydrogen gas or be available for hydrogen diffusion:



Subsea pipelines for hydrogen gas transport may be exposed to hydrogen both from the outside (from CP) and from the hydrogen gas on the inside the pipe. Subsea pipelines may be subjected to both to monotonic and low cycle dynamic loading. Hence, the combined effect of atomic hydrogen, microstructure and load conditions needs to be understood and controlled to reduce the risk of hydrogen assisted failures. An important part of this picture is the understanding of the mechanisms that are involved when hydrogen enters the steel. The following chapter presents the mechanisms of hydrogen entry into metals in both a gaseous atmosphere and aqueous atmosphere.

## 1.2 Adsorption and Absorption

The hydrogen as an element consist of one proton and one electron. In its natural state, it forms diatomic molecules of hydrogen gas, H<sub>2</sub>. The hydrogen molecule is too large to diffuse interstitially in metals, hence it needs to dissociate into its monoatomic form, H, on the metal surface, thereby diffusing into the metal, illustrated in Figure 2(a). Hydrogen entry into the material consist of two distinct steps, *adsorption* and *absorption*.

The adsorption (gas-metal interaction) includes the mechanisms of *physisorption* and *chemisorption* before eventually absorption and/or desorption occurs. These two processes differ from each other in terms of bonding energy. The energy situation is often visualized in a simplified potential energy

diagram, where the energy of the system is a function of the distance from the metal surface, Figure 2(b). As the H<sub>2</sub> molecule approaches the metal surface, weak van der Waals attractive forces becomes present (less than 0.5 eV) between H<sub>2</sub> molecule and the surface atoms and give rise to a small minimum in the energy-curve. At this point there is no sharing or transport of electrons between the H<sub>2</sub> molecule and the metal surface. Approaching the metal surface in its molecular form requires a lot of energy. This process is simplified when molecules dissociate into atoms which are individually attracted to the surface by chemisorption forces, illustrated as a deep energy minimum in the curve. The chemisorption occurs as a result of a chemical interaction due to covalent bonding between the adsorbent molecule (H<sub>2</sub>) and the surface atom.

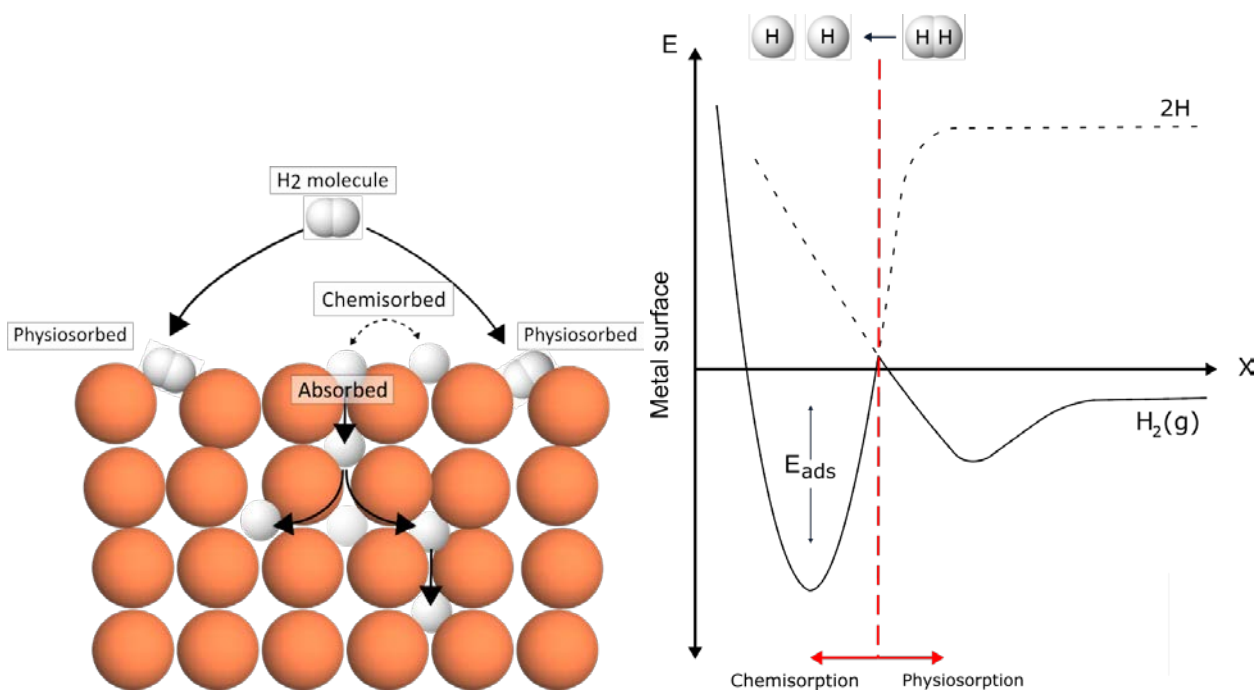
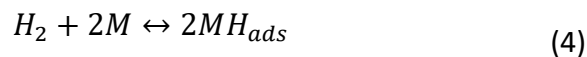


**Figure 2: a) Schematic illustration of the chemisorption and physisorption process and b) the energetic landscape, E, that a H<sub>2</sub>(g) molecule encounters when approaching a metal surface with a distance, X. Figure adopted from [8].**

When hydrogen atoms adsorbed on the metal surface, the following reaction occurs:



Which is a reversible reaction i.e. two hydrogen atoms can recombine to form H<sub>2</sub> molecule (Tafel mechanism).

Hydrogen entry into the material is highly dependent of several parameters, including surface conditions, pressure and temperature. The influence of pressure has a central part in the adsorption process for gaseous hydrogen when it comes to the quantification of the hydrogen uptake and the readily availability for diffusion in the material bulk. The solubility of hydrogen in a gaseous environment can be determined from thermodynamic laws such as Sieverts law [9]. The empirical relation shows that H in metals is proportional to the square root of the partial pressure of the gas in thermodynamically equilibrium, generally written as:

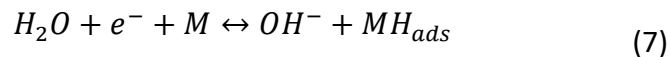
$$K^2 = \frac{S_H^2}{P_{H_2}} \quad (5)$$

where  $K$  is the equilibrium constant,  $S_H$  is the concentration of dissolved H and  $P_{H_2}$  is the partial pressure of gaseous hydrogen. The equilibrium condition is established when there is equivalence of chemical potential between H molecule and H atoms dissolved in the metal lattice. The concentration of dissolved hydrogen can be expressed by a classic Arrhenius law:

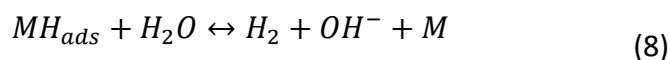
$$S_H = S_0 \sqrt{P_{H_2}} \exp\left(\frac{-\Delta H_s}{RT}\right) \quad (6)$$

$S_H$  is the total concentration of dissolved hydrogen in equilibrium with a gaseous pressure,  $P_{H_2}$ ,  $S_0$  is the Arrhenius pre-exponential factor and  $\Delta H_s$  is the dissolution enthalpy (J/mol).  $R$  denotes the gas constant and  $T$  is the absolute temperature.

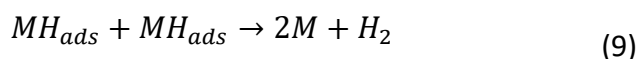
The adsorption by gaseous hydrogen differs from that of an electrolytic hydrogen system. Generally, the hydrogen entry into a metal in an acid and alkaline electrolyte is expressed in terms of the Hydrogen Evolution Reactions (HER) associated with adsorption/desorption. Initially, in an alkaline solution, the water molecule is cleaved into a hydroxyl ion (OH<sup>-</sup>) and an adsorbed hydrogen atom (Volmer step):



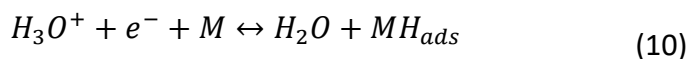
When the hydrogen is adsorbed on the metal surface, there are two possible pathways; Either via the interaction of the adsorbed hydrogen atom and the water molecule (Volmer-Heyrovsky: electrochemical desorption):



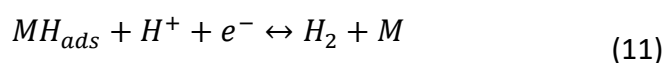
or by the combination of two adsorbed hydrogen atoms (Volmer-Tafel mechanism: chemical desorption):



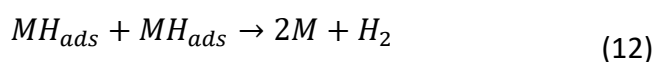
In both reactions, the hydrogen atoms recombine and release gaseous hydrogen to the environment. In an acid solution, the initial adsorption occurs when hydrogen protons from the solution form adsorbed hydrogen:



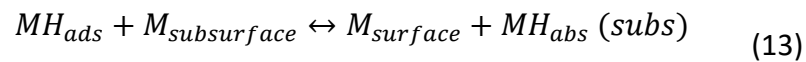
followed by the Volmer- Heyrovsky reaction, where a solvated proton from the solution reacts with the adsorbed hydrogen on the metal surface and form  $H_2(g)$ :



or two adsorbed surface hydrogens could react and form  $H_2$  in a similar manner as for the reaction in an alkaline medium, eq.9 (Volmer-Tafel).



The presence of hydrogen is not a challenge for the materials integrity before absorption of adsorbed hydrogen atoms occurs, which is a process competing with the other stages. Hydrogen atoms can also recombine in the surface-subsurface and diffuse into bulk described by the following equation:



### 1.3 Transport

Within the metal hydrogen atoms occupy interstitial sites in the metal lattice or locate at microstructural features. Here, the hydrogen atoms can jump from one site to the neighbour site over large distances through the metal. The probability for finding a new interstitial site to occupy, is high, leading to a high diffusion rate, i.e. rate of hydrogen transport. The hydrogen atom has a radius of  $5.3 \cdot 10^{-11}$  m, i.e. the same order of magnitude as the interstitial sites in the metallic face-centered cubic (fcc) -and bcc structure. This allows for interstitial diffusion and high mobility of the hydrogen atoms in bcc materials, allowing thermodynamic equilibrium to be reached within relatively short time even at ambient temperatures [7].

At room temperature, the diffusivity of hydrogen in pure bcc iron is about  $1 \cdot 10^{-10}$  m<sup>2</sup>/s, ten order of magnitudes higher than the diffusivity of carbon and nitrogen, i.e.  $1 \cdot 10^{-20}$  m<sup>2</sup>/s [10]. The main parameters affecting the diffusivity and solubility are temperature, chemical composition and crystal structure. Considering, low-carbon pipeline steels, the basic lattice structure consists of a bcc structure. Theoretical studies indicate that H is favoured at the octahedral sites (or tetrahedral sites) for austenite (fcc), while for ferrite, tetrahedral sites are the favourable position [11]. The interstitial sites in the bcc lattice are illustrated in Figure 3. In the fcc structure, octahedral sites are largest, and visa versa for the bcc structure, meaning less distortion occurs when H occupies the tetrahedral site in a bcc structure.

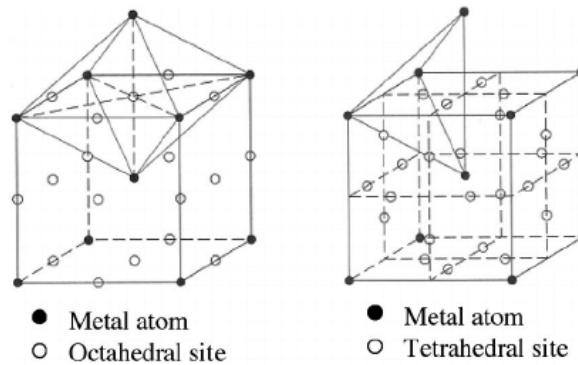


**Figure 3: Interstitial lattice sites in the bcc crystal structure [12].**

The dissolution energy for hydrogen in ferrite is larger than in austenite, resulting in a lower solubility of H in bcc. The solubility of hydrogen in iron are shown in Figure 4. There is a greater number of sites in the bcc structure, but the size of the interstitial sites is smaller than in fcc. However conflicting theoretical predictions of favourable occupancy sites are debated [13, 14]. The ferritic microstructure in pipeline steels will be modified in welded areas. Thus, it is important to evaluate the hydrogen diffusivity in different microstructures such as base metal, weld metal and the heat-affected zone (HAZ) [15, 16].

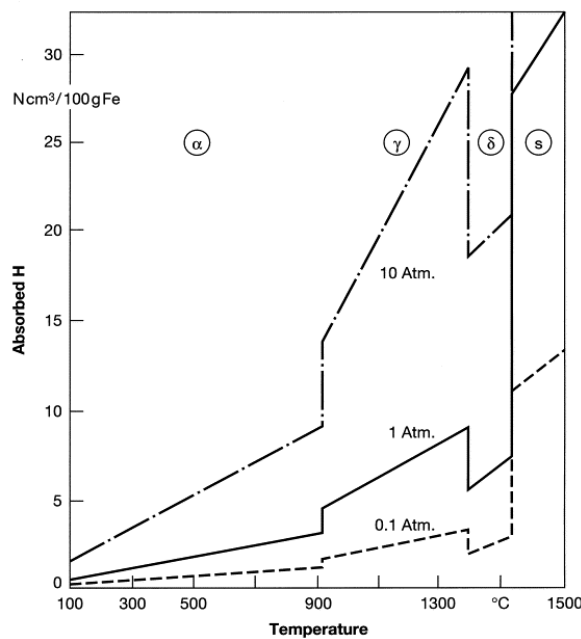


**Figure 4: Solubility of alpha and gamma iron as a function of temperature and pressure [6].**

The diffusion of hydrogen interstitials is given by Fick's first law describing the flux, J [17]:

$$J = -D\nabla C \tag{14}$$

with a magnitude that is proportional to the concentration gradient,  $\nabla C$ , where the  $C$  is the hydrogen density (hydrogen interstitials per unit volume). The negative sign in the diffusivity coefficient,  $D$ , indicates opposite directions of the concentration gradient and diffusion flux. The diffusion eventually leads to equilibrium state at  $\nabla C=0$ . Fick's second law describes the rate at which the concentration is changing at any given point in case of 3-dimensional diffusion:

$$\left(\frac{\partial C}{\partial t}\right) = -D\nabla^2 C \quad (15)$$

Each hydrogen atom is individually under a hydrostatic stress and cause a lattice distortion. Despite its small size, the hydrogen atom radius is still larger than the interstitial sites (0.53 Å vs 0.19 Å). The mean hydrostatic stress will affect the hydrogen solubility and diffusivity [18] as indicated in the following equation:

$$\left(\frac{\partial C_L}{\partial t}\right) = D\nabla^2 C_L + D\left(\frac{V_H}{R(T - T^Z)}\right)\nabla C_L \nabla p + D\left(\frac{V_H}{R(T - T^Z)}\right)C_L \nabla^2 p \quad (16)$$

Where  $V_H$  is the partial molar volume of hydrogen in the metal and  $p$  is the hydrostatic pressure. The equation states that the energy necessary to introduce a hydrogen atom in the lattice increases with the decrease of hydrogen concentration gradients and is decreased by dilatational hydrostatic stress: areas in front of cracks are therefore zones of strong accumulation for diffusible hydrogen. In a perfect lattice, hydrogen is accommodated in the interstitial sites of the crystal lattice. However, a material contains various lattice imperfections and microstructural features that either hinder diffusion or act as trapping sites [19, 20].

## 1.4 Trapping

Different microstructures are often present in a pipeline and consist of features which serve as potential traps for hydrogen. Potential locations for hydrogen trapping include dislocations, grain boundaries, second-phase particles, voids and interstitial solute atoms, as illustrated in Figure 5. [19, 21-23]. The traps will slow down the diffusion of hydrogen and reduce its energy state as the potential energy is lower than in normal interstitial sites. As shown in Figure 6, the traps can be visualized as a potential gap for hydrogen atoms [19]. As the hydrogen atoms diffuse towards the gap, they get trapped in an "energy sink".

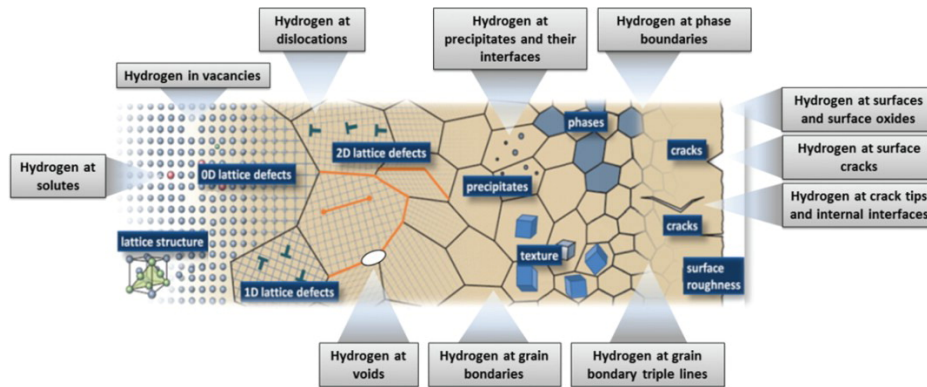


**Figure 5: Potential traps for hydrogen in steel [24].**

The strength of each trap is related to its binding energy, which is different among the structural defects and phases due to stress fields, temperature gradients, chemical potential gradients, and/or physical trapping. Depending on the value of the binding energy, two types of traps are distinguished: *reversible* and *irreversible traps*. Hydrogen can easily be released from reversible traps (vacancies, substitutional solved atoms, dislocations and grain boundaries) due to the weak binding energy of the structural defects. The irreversible traps have a stronger trapping effect and a higher activation energy is needed to release the hydrogen atom (e.g. the interface between non-metallic inclusions or precipitates). Temperature and time are important parameters for this classification. Table 1 shows the binding energy of hydrogen at sites for different traps.

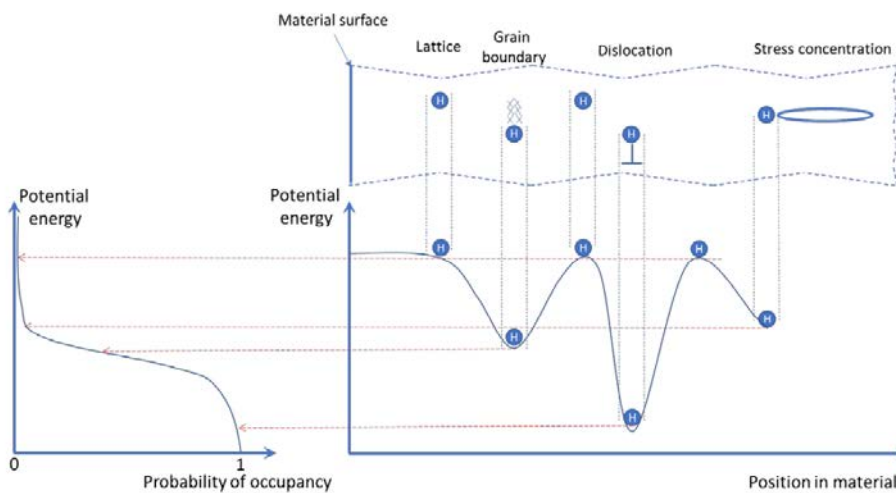


**Figure 6: Energy levels of hydrogen at different trapping sites.**

Hydrogen-induced failure in pipeline steels are mainly controlled by local hydrogen concentration, depending on where hydrogen is trapped. As H atoms strongly interact with hydrostatic stress fields, they get easily trapped in the dislocations generated prior to deformation, thus hindering diffusion. However, dislocation motion can also enhance the transport of hydrogen by forming "Cottrell



atmospheres" [25]. Dislocation trapping and transport are competing processes for the transport of hydrogen and have a strong influence on the evolution of hydrogen distribution in materials. The accumulation of dislocations at structural defects act as a barrier to their movement, hence the following dislocation stacking can promote initiation and/or propagation of a crack.

**Table 1: Binding energy for hydrogen in steel at various traps, adopted from [26, 27].**

Material	Hydrogen traps	Binding energy [eV]
α-Fe	Free surface	0.73
	Dislocation core	0.61
	Dislocation elastic stress field	0.21
	Grain boundary	0.10
	Interstitial (N)	>0.13
	Interstitial (C)	0.03
	Substitutional (Ti)	0.19
Bcc carbon steel	Vacancy	0.63
	Fe <sub>3</sub> phase interface	0.11

Hydrogen is either diffused into interstitial sites indicated with a concentration  $C_L$  or trapped in the material [22]. Oriani's model assumes equilibrium between these sites and both contributions represents the total amount of hydrogen in the metal [19]. The concept is described by the following relation:

$$C_T = \frac{K \frac{\alpha N_T}{\beta N_L} C_L}{1 + \frac{K}{\beta N_L} C_L} \quad (17)$$

$\alpha$  and  $\beta$  represent trapping and lattice sites, respectively.  $N_T$  and  $N_L$  are the available sites for hydrogen in traps and in lattice sites, respectively.  $N_L$  is found from:

$$N_L = \frac{N_A}{V_M} \quad (18)$$

Where  $N_A$  is the avogadro number ( $6.02214 \cdot 10^{23} \text{ mol}^{-1}$ ) and  $V_M$  is the molar volume of iron ( $7.116 \cdot 10^{-6} \text{ m}^3/\text{mol}$ )

$$K = \exp\left(\frac{-E_b}{RT}\right) \quad (19)$$

where  $E_b$  is the binding energy for the trapping sites [28].

## 1.5 Damage Mechanisms

Evidence of mechanisms responsible for the hydrogen effect on mechanical properties of steels have been purposed and discarded as new evidence has been uncovered. The HE term have been described of different aspects ranging from chemical bonding up to microstructural level. The overall opinion is that the interaction of several mechanism is responsible for the material degradation [29]. Theories have advanced as the more accepted ones for the case of hydrogen embrittlement/degradation in steel: Hydrogen Enhanced Decohesion (HEDE) and Hydrogen Enhanced Localized Plasticity (HELP). The main concept of these mechanisms is briefly explained below. A comprehensive list of publications regarding HE phenomena exists today. A generic overall insight on the HE phenomena can be found in the review by Djukic et al. [30]. They conducted an extensive review of the literature related to hydrogen embrittlement mechanisms, with particular focus on HELP and HEDE and their interplay in steels.

The concept of HEDE [31-33] suggest embrittlement due to localized reduction in cohesive strength of the iron lattice hence assist the separation of cleavage planes or grain boundaries under a lower stress. It is visualized as a tensile separation of atoms when a critical stress exceeds the local cohesive strength in the crack tip fracture process zone (FPZ), that is reduced due to the presence of hydrogen. The embrittlement is attributed to the weakening of interatomic bonds, resulting in separation of atoms instead of slip.

The HELP mechanisms [34, 35] assume that atomic hydrogen accelerate the dislocation mobility through an elastic shielding effect that cause a local reduction in shear stress. Hydrogen transport by dislocation motion could lead to localized high concentrations at distances further ahead of crack tip. Moreover, local high strains due to hydrogen clusters around dislocations, might disrupt interfaces and structures. The following stresses at these locations increase the risk for failure. When there is a sufficient hydrogen concentration, the local deformation process will eventually

lead to fracture of brittle behaviour macroscopically. Despite the comprehensive knowledge about HELP, it has always been difficult to link macro with micro scale and explain why the enhanced dislocation activity results in brittle fracture features.

HELP and HEDE have more recently been considered to act simultaneously in many cases. However, the universality of these models still needs to be confirmed. Recent advancements in fractographic analysis elucidate the role of hydrogen in localized mobility of dislocations around crack tip [36-38]. Undoubtedly, hydrogen susceptibility in steel is highly dependent on the type and morphology of inclusions and microstructure. Thus, in order to correctly address the susceptibility in relation to atomic hydrogen, the details of material requirements for pipeline steels with respect to the microstructural features are of paramount importance.

## 2 Materials and Metallurgy

### 2.1 Classification of Pipeline Steel

The offshore pipeline infrastructure consists of several pipeline-steel grades, predominantly categorized by the American Petroleum Industry (API) under the standard API 5L [39]. The various grades of steel are designated according to its minimum specified yield strength in ksi (kilo psi, 1 ksi= 6.9 MPa). Table 2 lists the yield strength and ultimate tensile strength requirements according to the API 5L standard. The X52 steels have been commonly in service for natural gas transport from the early 50`s, but as pipeline steels have gone through a continuous progress in terms of mechanical properties through improving metallurgical and material processing techniques, more modern alloys have been developed specifically for hydrogen application, such as *modern* X52, X60, X65 and X70. The main difference between a vintage X52 and its modern counterpart is the higher carbon content. Typically, the carbon content can be up to three times lower in modern steels to improve the weldability [40].

Similarly, higher strength modern steels such as X60, X65 and X70 have also been developed for the purpose of oil and gas transport in harsh environments and have even less carbon content. While currently X65 is the highest grade approved for sour gas application [41], higher grades of API 5L steels, such as X80, X100 and even X120 have in the recent years, received high attention for (onshore) pipeline applications due to their superior high mechanical strength, allowing for thinner pipeline walls and lower costs [42, 43]. However, these are mainly used for onshore applications and have different design and strength criteria and requirements from their applications and are therefore not included in the current review which focus on high strength steels up to 480 MPa (X70).

**Table 2: API 5L yield- and ultimate tensile strength requirements for X52-X70 line pipe steel [39].**

Grade	YS min. [MPa]	YS max. [MPa]	UTS min. [MPa]	UTS max. [MPa]
<b>X52</b>	359	531	455	758
<b>X56</b>	386	544	490	758
<b>X60</b>	414	565	517	758
<b>X65</b>	448	600	531	758
<b>X70</b>	483	621	565	758

The API`s material specifications are restrictive regarding chemical composition in order to obtain high levels of toughness and formability at a specific level of yield strength. It is important that the high yield strength is not accompanied by a decrease in fracture toughness and formability which would translate into lower resistance to stress induced cracking (SIC) and challenges in forming.

Thus, a low YS/UTS (<0.93) ratio is nowadays required for pipeline applications. This ratio is mainly affected by the microstructure. In order to obtain the aforementioned combination of mechanical properties for pipeline steels, a careful selection of alloying elements is necessary [39, 44]. For instance, a low carbon level and the carbon equivalent (CEV) is important for ductility and formability, but also to enhance the weldability and toughness. However, lowering the CEV cause a decrease in strength that needs to be optimized accordingly in terms of chemical composition and processing schedule [45]. To ensure the combination of compatible properties, thermo-mechanical controlled rolling (TMCR) has been widely implemented for the pipe processing technology due to its simple and cost-efficient methodology. TMCR is a complex process involving the interaction of chemical composition, temperature and deformation and different metallurgical phenomena [46]. The process allows the yield strengths of the pipeline to be tailored through the combination of grain refinement, precipitation hardening (micro-alloying), and phase transformations.

## 2.2 Chemical Composition of Pipeline Steel

The high strength which characterizes the pipeline steels for offshore applications is obtained through microalloying. The chemical composition in pipeline steels may vary for different thicknesses and grades to meet the requirements. Typically, a X65 pipeline steels will have a low carbon content, less than 0.1 wt % C in combination with a manganese (Mn) content up to 2.0 wt %. Additionally, the composition has small amounts of alloying elements such as silicon (Si), phosphor (P), chromium (Cr), niobium (Nb), molybdenum (Mo) and vanadium (V) etc. [15, 47]. Overall, the main function of these elements is to improve mechanical or physical properties, such as increase the strength by grain refinement, solid solution and precipitation hardening. An overview of the effect of some alloy elements in pipeline steel are schematically shown in Figure 7 [48]. Solid solution hardening is highly related to the alloy element content and precipitation hardening and grain refinement depend on the interaction between chemical composition and the thermomechanical controlled process (TMCP). Each element, in correlation with a specific cooling rate, will determine the type and the volume fraction of the resulting microstructure with optimized properties for its application. However, some alloying elements have adverse effects on the hydrogen embrittlement susceptibility of pipeline steels by introducing microstructural features that finally affect the hydrogen diffusion. This effect is highly dependent on the manufacturing process and heat treatment that results in different microstructures [49].

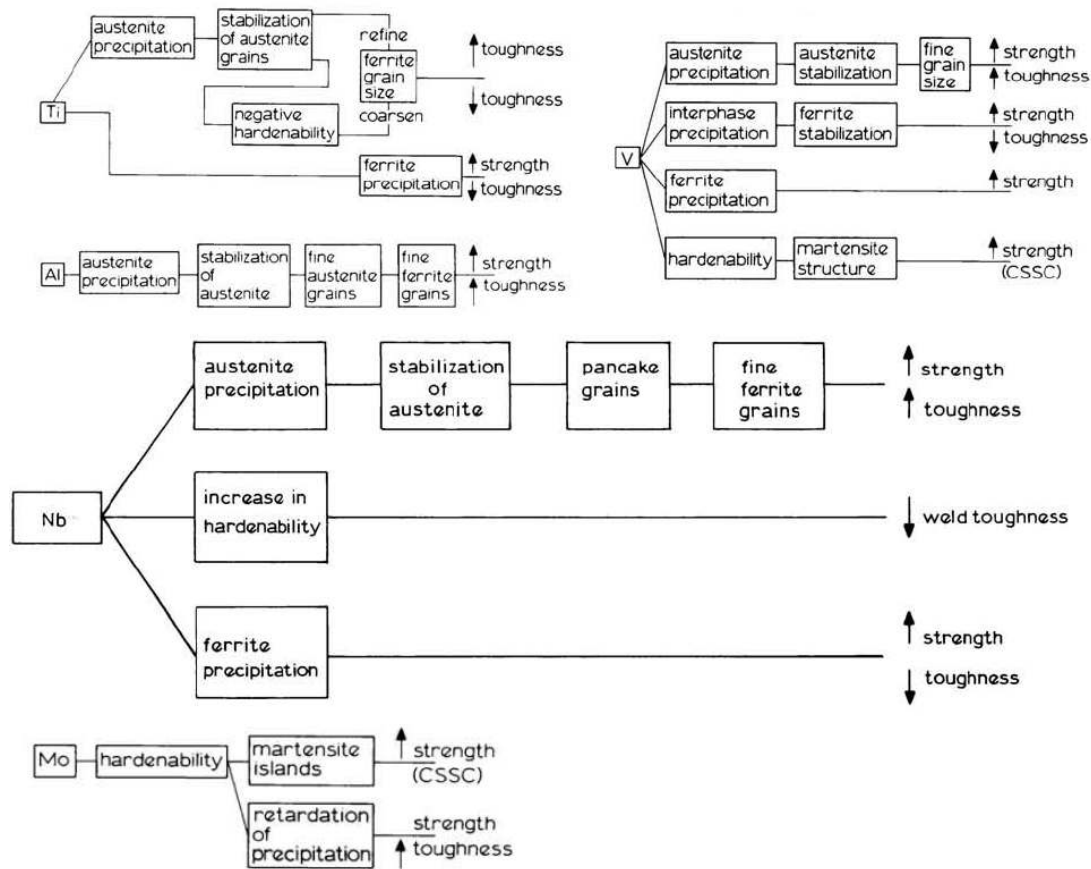


Figure 7: Effect of alloy elements in pipeline steel [48].

## 2.3 Microstructures in Pipeline Steels

The role of microstructure is one of the most important factors to consider in terms of susceptibility of pipeline steel to hydrogen degradation. Overall, for a welded line pipe, three different microstructural zones that need to be considered in terms of HE; the base metal (BM), weld metal (WM) and the heat-affected zone (HAZ). In general, microstructures found in low carbon steels are ferrite (polygonal and acicular), pearlite, bainite (lower and upper), acicular ferrite and martensite. Furthermore, additional second phases are often present in the HAZ [5].

### 2.3.1 Base Metal (BM)

X52 vintage steels usually have microstructures consisting of polygonal ferrite and pearlite, while modern steels, including X65 and X70, are likely made up of polygonal ferrite, acicular ferrite as well as possibilities for other formation products, such as bainite and acicular ferrite, as shown in Figure 8 for X52 vintage -and X52 modern steel [40, 50]. The grain size is shown to be significantly larger for the X52 vintage steel, Figure 9. Typical microstructures X60, X65 and X70 pipeline steels, are presented in Figure 10 and Figure 11. All microstructures are obtained using the thermomechanical

process, except for the X60 steel. The fine-grained microstructures providing the superior mechanical properties, are clearly prominent for the X65 and X70 steel. In contrast a more coarse-grained polygonal ferrite/pearlite microstructure is present for the X60 steel. The multiple heating sequences and rolling stages in TMCP can also favour other microstructural features such as M/A constituents. The presence of M/A islands and stringers are typically observed at the ferrite and bainite grain boundaries as well as in pearlite islands, as shown in Figure 12 for a X65 steel [51].

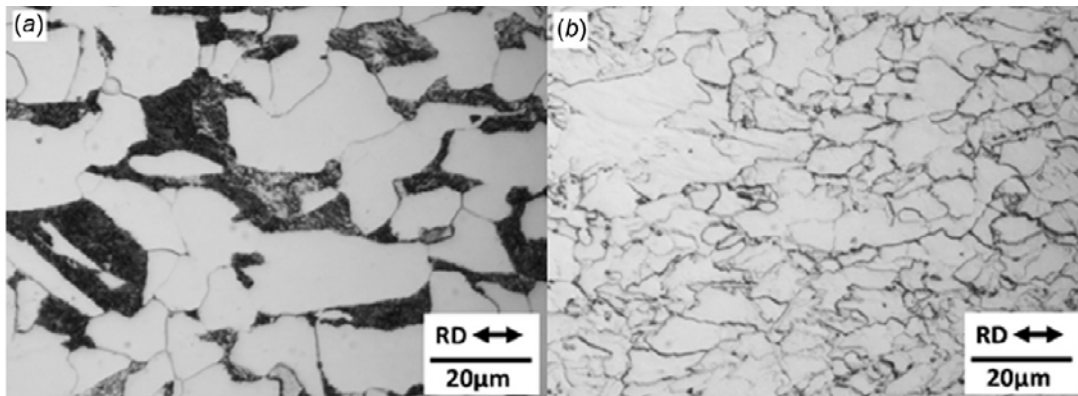


Figure 8: Optical microscope image in the longitudinal orientation of a) X52 vintage and b) X52 modern pipeline steel composed of polygonal ferrite (light phase) and pearlite (dark phase), and polygonal ferrite and acicular ferrite, respectively [40].

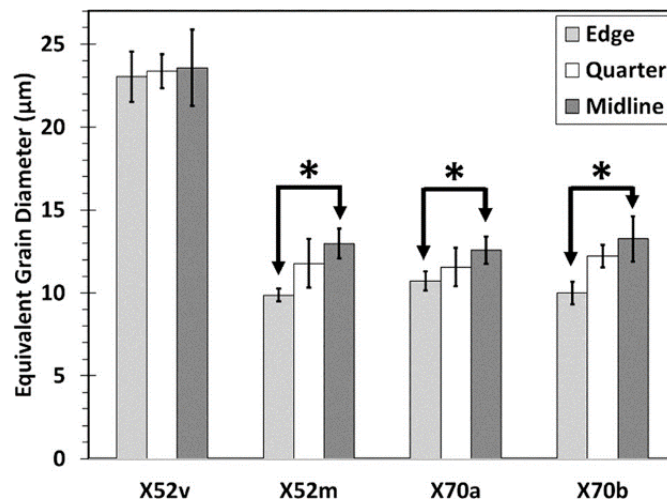
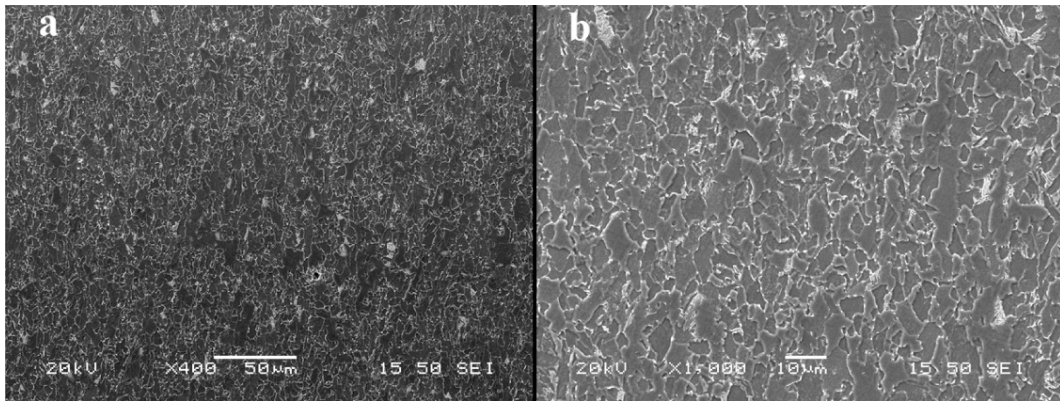
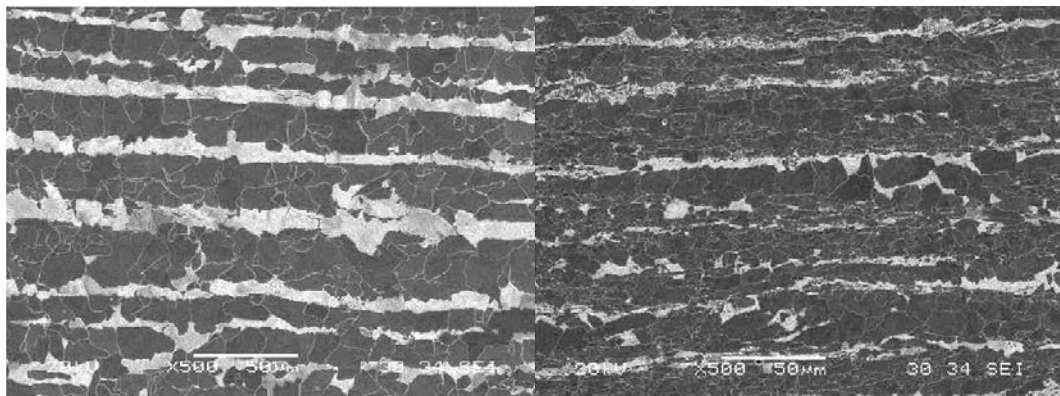


Figure 9: Grain size for X52 vintage and modern pipeline steel for three locations, compared with two higher strength steel, X70 [50].



**Figure 10: SEM micrographs at two magnifications of natal etched X65 steel composed of ferritic-bainitic microstructure with some pearlite islands [51].**



**Figure 11: SEM micrographs of a) X60 manufactured by traditionally hot rolling and normalising operations and b) X70 obtained from thermomechanical processing [52].**

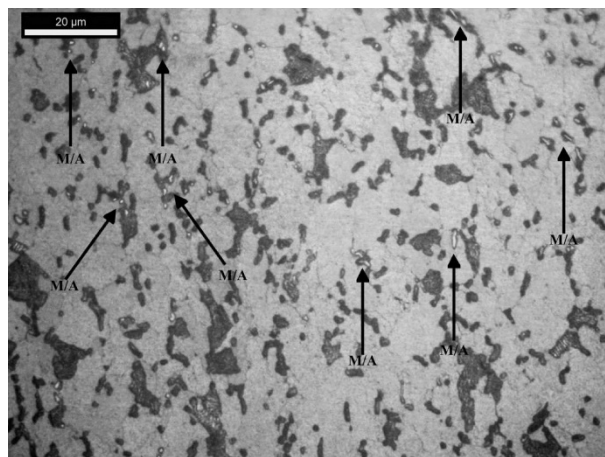


**Figure 12: Optical micrograph of X65 microstructure after etching, showing the presence of M/A-constituents (white) inside the pearlite phases [51].**

The ferritic microstructure is formed at low cooling rates from austenite at the highest transformation temperature (over 650 °C). The ferritic grains precipitate on austenitic grain



boundaries and result in a polygonal or equiaxed morphology that is identified by a low dislocation density and absence of substructures. At higher cooling rates, different phases and characters of ferrite will form, such as Widmanstätten ferrite (WF), polygonal ferrite (PF), granular ferrite (GF), acicular ferrite (AF) and martensite, as shown in the continuous-cooling transformation plot for HSLA steels, Figure 13 [53, 54]. In general carbon diffusion is hindered at higher cooling rates during the phase transformation,  $\gamma \rightarrow \alpha$ , resulting in various crystal structures [55].

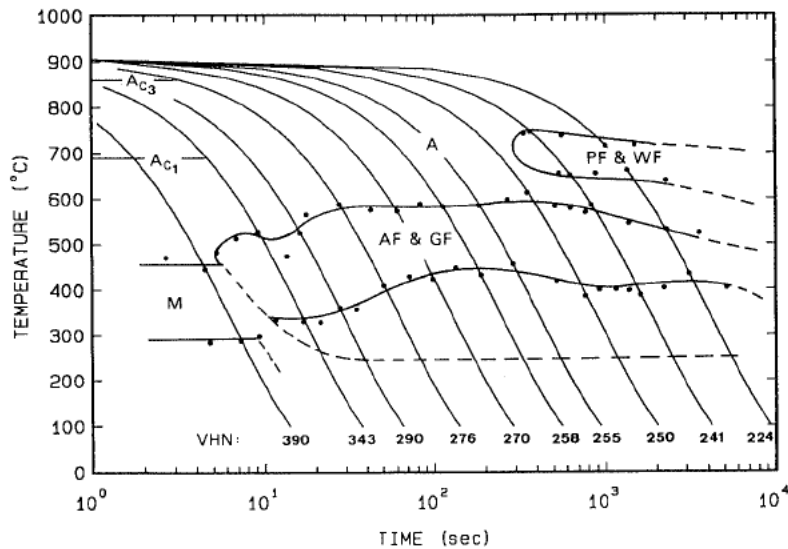


**Figure 13: Continuous-cooling transformation (CCT) diagram for HSLA steel [54, 56].**

The occurrence of pearlite phases in the ferritic matrix, depends on the cooling rate and carbon content. At sufficiently low cooling rates, carbon has sufficient time to diffuse and form cementite ( $\text{Fe}_3\text{C}$ ) and ferrite, in a striped appearance. The pearlite appears as dark bands in the rolling direction at sufficient levels of carbon. Figure 14 shows an example of the resulting microstructure at different pearlite contents for a X52 -and X65 pipeline steel [57]. Reduction of carbon corresponds to a decrease in pearlite content. The banded pearlite character is in general more distinct in the mid-thickness due to the segregation of carbon during solidification. The optical micrographs in Figure 14 are from  $\frac{1}{4}$  thickness.

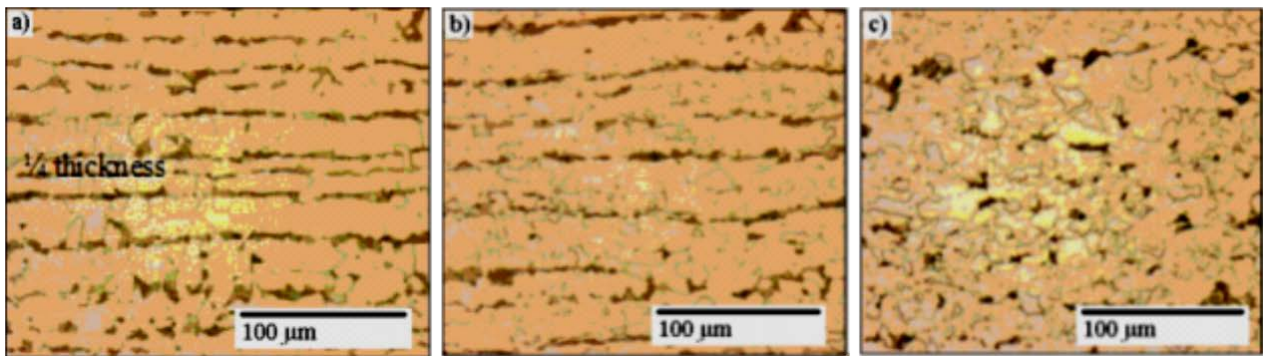


Figure 14: Ferrite-pearlite microstructure with reduced pearlite content in a) X52 (0.12 wt% C), b) X65 (0.1 wt% C) and c) X65 (0.08 wt% C) steel [57].

### 2.3.2 Heat-Affected Zone (HAZ)

The subsea pipeline infrastructure that transport gas consists of nearly 9000 km pipelines in distance. The network of pipelines consists of smaller pipe sections welded together, where the typical length per section is 12 m (40 ft.). This is elucidating the large number of welds needed to span a large distance of pipelines. Moreover, multiple weld passes are often necessary, from 2 and up to 10 cycles, as the pipelines often have a wall thickness up to 40 mm. Welding of pipeline steels introduce a heat-affected zone (HAZ) that are exposed to several heating and cooling cycles. Consequently, microstructural changes occur that can be critical to the materials integrity, particularly, due to the loss in toughness. An overview of the various HAZ regions are shown in Figure 15 (a).

Overall, the HAZ consists of four distinct zones from single pass welding, whereas the region displaying the lowest toughness is the coarse-grained zone (CGHAZ), consisting of a bainite/martensitic microstructure. As a result of the multi-pass welding procedure, HAZ is reheated and undergo microstructural changes that results in the formation of localized and brittle phases, schematically shown in Figure 15 (b). The CGHAZ is roughly subdivided into four characteristics zones according to the peak temperature of subsequent thermal cycles during the multi-pass welding procedure; the unaltered (UA) CGHAZ, reheated to grain growth temperatures or not reheated at all, the super-critically reheated (SC) CGHAZ, reheated just above  $A_{C3}$ , the inter-critically reheated (IC) CGHAZ, reheated to austenite/ferrite two phase region ( $A_{C1} < T_{P2} < A_{C3}$ ) and finally, the subcritically- reheated (SCR) CGHAZ for  $T_{P2} < A_{C1}$ .

Among these, the intercritically-reheated coarse-grained zone (IC CG HAZ), have demonstrated to be the most challenging in low carbon steels [5]. The critical microstructural change occurs due to the transformation from ferrite to austenite during the heating process, subsequently followed by a transformation from carbon-rich austenite to martensite with retained austenite by rapid cooling. The resulting microstructure consisting of a mixture of martensite and retained austenite are often referred to as M-A constituents, shown in Figure 16. These are identified as hard and brittle zones

due to the inherent hardness and brittleness of martensite and often appear as blocky and/or lath constituents formed along austenite grain boundaries. The poor properties of the M-A constituents makes them a candidate for crack initiation due to the local reduced fracture toughness and high susceptibility to hydrogen embrittlement [58].

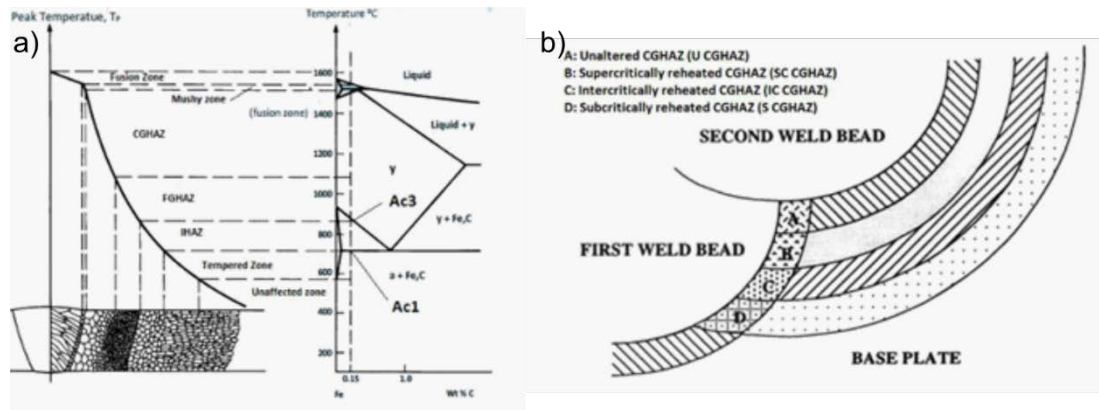


**Figure 15: (a) Schematic representation of the HAZ regions in a weld corresponding to the Fe-C binary phase diagram adapted from [59] and the HAZ with a multipass weld [5].**

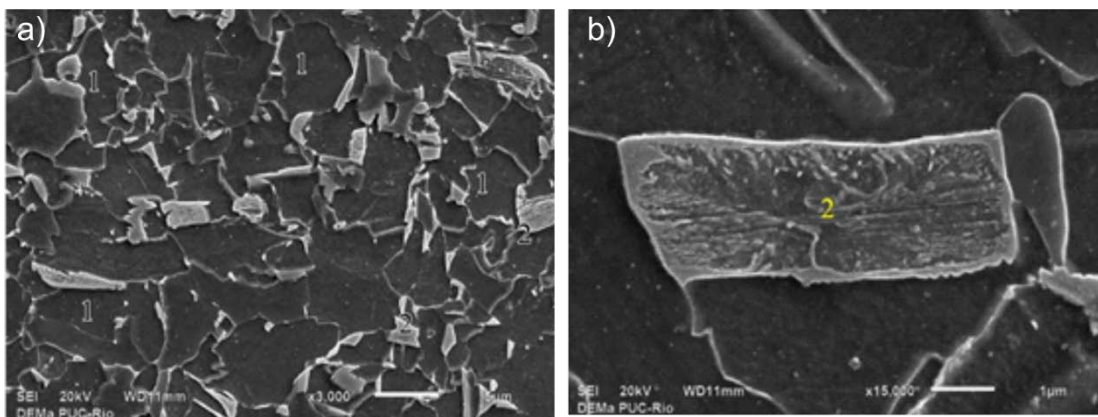


**Figure 16: M-A constituent, annotated 2, in a X80 pipeline steel with magnification (a) x3000 and (b)x 15.000 [60].**

### 3 Test Methods for Hydrogen Embrittlement

The presence of hydrogen in pipelines may introduce critical challenges when it comes to the overall performance: the mechanical properties (in particular the ductility), the toughness and the fatigue performance are, to a different extent, degraded which may ultimately pose a serious threat to the structural integrity of the pipeline. Hydrogen can enter the materials from both internal and external sources. The former is related to the processing, i.e. welding or steelmaking manufacturing. In addition, oil and gas exploration in deep waters introduce challenges when it comes to weld repair. The pressurized welding process, i.e. hyperbaric welding, include higher cooling rates and alter

material properties. Together with hydrogen dissociation out of the moisture from welding atmosphere, this can cause high susceptibility to hydrogen embrittlement [61]. On the other hand, hydrogen absorption into the material may occur from external sources, such as electrolytic from cathodic protection or gas charging. Hydrogen uptake from cathodic protection is often regarded as the main hydrogen source to subsea pipelines. Transport of pressurized hydrogen gas in pipelines originally designed for natural gas transportation will generate an additional external hydrogen source.

In this respect, test methods and technologies that simulate the operation environmental conditions the pipelines are exposed to, are crucially important to study to quantify the impact of hydrogen degradation and help preventing catastrophic failures. The charging of hydrogen into test specimens are commonly performed by either electrochemical charging or exposure to high pressure hydrogen gas [62, 63]. Additionally, both methods are often performed with in-situ hydrogen charging that has proven to be important for the evaluation of hydrogen induced degradation in bcc steels, due to the high diffusion coefficient that could result in significant hydrogen escape from the steel with ex-situ charging [63]. Theoretically, the same amount of hydrogen can enter the metal by the different methods, if the appropriate parameters are chosen. As soon as the hydrogen is absorbed into the steel lattice structure, the mechanisms responsible for hydrogen embrittlement, for a given microstructure, are the same [64].

### 3.1 Electrochemical Hydrogen Charging

Hydrogen embrittlement testing of pipeline steel used at deep sea levels normally involves electrolytic hydrogen charging of a specimen in a solution to simulate galvanic coupling or cathodic protection either before (pre-charging) and/or during a mechanical test. The technique is based on an electrochemical cell, where the steel specimen, act as the cathode and a wire of platinum act as the anode, both submerged in an electrolyte, i.e. the medium of the current transfer. When an electrochemical potential is applied across the electrodes, the electrolytic solution decomposes and hydrogen ions (protons) are produced, that can be measured from the reference electrode SCE (Saturated Calomel Electrode). The applied potential creates a flux that generates a high concentration of hydrogen ions in the specimen surface and act as a driving force for hydrogen diffusion into the bulk [65]. Generally, the necessary considerations for electrochemical charging are the environmental conditions i.e. electrolyte, temperature, cathodic potential, charging conditions (current density and time). Parameters are often chosen so that the practical application of interest are reproduced as close as possible or to eventually evaluate the influence of cathodic charging on the mechanical response of the material under investigation.

Usually, since absorption, adsorption and diffusion are all thermally activated phenomena, pre-charging performed at elevated temperatures will increase the hydrogen uptake rate [66]. Pre-charging and ex-situ testing have the drawback with hydrogen outgassing that results in hydrogen

concentration gradient or complete hydrogen escape within short time [67]. Therefore, it is important to charge the sample during deformation to obtain the constant hydrogen interaction with the pipeline. During in-situ hydrogen charging testing, the test setup is simulating a realistic condition where an in-service pipeline transfers hydrogen from the cathodic protection and constantly expose the pipeline to hydrogen with a given pressure or current. In addition, the development of microstructural defects, crack embryos, discontinuities as well as the kinematic related to dislocations in the materials induced by the solicitations inherent to the mechanical test performed, will be accounted for with respect to the consequent different hydrogen transport/distribution in these regions.

### 3.2 Gaseous Hydrogen Charging

Traditionally, gaseous hydrogen charging is performed in an oxygen-free, high-conductivity copper chamber with tantalum hydride ( $TaH_5$ ). As the tantalum hydride decomposes, a high partial pressure of hydrogen gas rises at high temperatures ( $>973$  K) and hydrogen diffusion into the specimen takes place [66, 68, 69]. The use of high-pressure hydrogen autoclave is another charging technique, supplemented with high temperature to decrease the charging time. Commonly, specimens are charged for a long period, up to several weeks at the target pressures and temperatures [66].

Nevertheless, high pressure gaseous hydrogen charging needs more considerations with regards to the procedures for conducting the test compared to electrochemical cathodic charging tests. Testing in in-situ pressurized hydrogen charging needs to be performed in strictly controlled facilities due to the risk of explosion [70]. The diffusion of hydrogen after charging can be described by the solution of Fick's second law, [eq.15](#), with the resulting hydrogen concentration profiles depending on parameters such as time, temperature and surface conditions (concentration of hydrogen.) This test method is appropriate for a wide array of applications relevant for hydrogen energy technology, including pipelines that are/can be exposed to mechanical loading while transporting hydrogen gas. As for the case of electrochemical charging, in-situ testing is regarded as the most reliable way of testing to reproduce the real application case [70].

Several mechanical tests have been used to study the effect of hydrogen gas on different mechanical properties: tensile testing, disk rupture, fracture threshold and fatigue crack growth tests being the most frequent in literature. Tensile and disk rupture tests as usually regarded as screening type of testing which provide a qualitative input for evaluating the relative behaviour of alloys. However, these tests do not provide quantitative data to fully assess the performance of the pipeline in service. Here, fracture mechanic testing address crack initiation and hydrogen-assisted propagation growth under cyclic or quasi-static loading and provide data that can be used in structural life assessments [70].

## 4 Tensile Properties

### 4.1 Hydrogen Influence on Tensile Properties

It is important to understand the influence of hydrogen on the tensile properties for the assessment of pipeline in-service performance. The yield strength, the ultimate strength, the total elongation and reduction in cross-sectional area, are obtained by uniaxial loading in tension until failure, by using one of the established approaches: the slow strain rate (SSR) test or the linearly increasing stress test (LIST). The specimens can either be a smooth, notched or a plain strain specimen. The *ductility* of a material is an important property and can be qualified by the fracture strain,  $\epsilon_f\%$ , the engineering strain at which a specimen fracture during a uniaxial tensile test, or by the reduced area at fracture,  $R_A\%$ , from the following equation [71]:

$$R_A \% = \frac{A_i - A_f}{A_i} \cdot 100\% \quad (20)$$

with the initial and final fracture areas,  $A_i$  and  $A_f$ , respectively. Hydrogen related degradation usually manifest in the form of ductility loss and can be measured in terms of area reduction after a tensile test and/or the different values of fracture strain obtained with or without hydrogen charging are evaluated [72-75]. An embrittlement index,  $EI$ , are often defined to evaluate the hydrogen embrittlement (HE) [76, 77]:

$$EI = \frac{RA_{air} - RA_H}{RA_{air}} \cdot 100 \quad (21)$$

where the  $RA_{air}$  and  $RA_H$  are the reduced area at fracture in air and in a hydrogen atmosphere. A high index is correlated to a higher hydrogen susceptibility of the material investigated. The most prominent trend is the strong decrease in sample elongation and reduction of area with increasing hydrogen content and is generally used to quantify the degree of HE.

Tensile tests of smooth specimens in carbon steels tested in hydrogen gas, reveal that the reduction of area is degraded in the presence of hydrogen. The ultimate tensile strength on the other hand, are barely affected. San Marchi et al. [78] have summarized tensile properties (longitudinal) from tests in hydrogen gas (6.9 and 69 MPa) for a wide range of carbon steels [79-81]. The data from the relevant pipeline steels are shown in Table 3. The reduction of area obtained in hydrogen gas are shown to be very consistent (measurements ranging from 35-47%) for nearly all carbon steels. Moreover, the loss of reduction of area relative to values measured in air, can be as high as 50 %.

Notched specimens obtain similar trend in hydrogen gas as shown in smooth tensile test specimens, i.e. high reduction of area and limited changes in tensile strength. Data from tensile tests of various carbon steel notched specimens (X52, X60, X65, X70 + other carbon steels) [79], summarized by San Marchi [78], reveal this comparable behaviour. Consistent values of the reduction in area are in the range of 5 to 9 %. However, the relative area loss, to values measured in air is more pronounced from tests of notched specimens (than for smooth specimens), i.e. up to 80%, Table 4.

**Table 3: Tensile properties from smooth specimens of pipeline steels tested in 6.9 MPa hydrogen gas (and air for comparison) at room temperature. Data from [79-81].**

Steel	Test environment	Strain rate [ $s^{-1}$ ]	$\sigma_y$ [MPa]	$\sigma_{UTS}$ [MPa]	$El_t$	RA [%]
<b>X42</b>	Air	$1 \times 10^{-4}$	366	511	21	56
	6.9 MPa H <sub>2</sub>		331	483	20	44
<b>X42 (T)</b>	Air		311	490	21	52
	6.9 MPa H <sub>2</sub>		338	476	19	41
<b>X52</b>	Air	$\sim 3 \times 10^{-4*}$	414	609	19	60
	6.9 MPa H <sub>2</sub>		429	597	15	37
<b>X60</b>	Air	$\sim 3 \times 10^{-4*}$	427	594	13	49
	6.9 MPa H <sub>2</sub>		422	590	10	27
<b>X65</b>	Air	$\sim 3 \times 10^{-4*}$	504	605	15	57
	6.9 MPa H <sub>2</sub>		506	611	15	36
<b>X70</b>	Air	$1 \times 10^{-4}$	584	669	20	57
	6.9 MPa H <sub>2</sub>		548	659	20	47
<b>X70 (T)</b>	Air		613	702	19	53
	6.9 MPa H <sub>2</sub>		593	686	15	38
<b>X70</b>	Air	$\sim 3 \times 10^{-4*}$	626	693	16	77
	6.9 MPa H <sub>2</sub>		566	653	14	37
<b>X70 (Arctic grade)</b>	Air	$\sim 3 \times 10^{-4*}$	697	733	14	77
	6.9 MPa H <sub>2</sub>		695	733	12	37

T=Transverse oriented specimen

\*Calculated based on displacement rate and specimen gauge length

**Table 4: Tensile properties from notched specimens of pipeline steels tested in 6.9 MPa hydrogen gas (and air for comparison) at room temperature. Data from [79].**

Steel	Sample geometry	Test environment	Displ. rate [mm/s]	$\sigma_y^*$ [MPa]	$\sigma_s$ [MPa]	RA [%]
X52	(a)	Air 6.9 MPa H <sub>2</sub>	8.5 x 10 <sup>-3</sup>	414	818	15
				429	707	7
X60	(a)	Air 6.9 MPa H <sub>2</sub>	8.5 x 10 <sup>-3</sup>	427	847	23
				422	782	8.4
X65	(a)	Air 6.9 MPa H <sub>2</sub>	8.5 x 10 <sup>-3</sup>	504	806	21
				506	758	6.1
X70	(a)	Air 6.9 MPa H <sub>2</sub>	8.5 x 10 <sup>-3</sup>	626	946	45
				566	845	8.7
X70 (Arctic grade)	(a)	Air 6.9 MPa H <sub>2</sub>	8.5 x 10 <sup>-3</sup>	697	1027	42
				695	949	8.6

\*Yield strength of smooth tensile specimen

(a) V-notched specimen: 90° included angle; min diameter = 2.44 mm; max. diameter = 2.87 mm; notch root radius = 0.025 to 0.051 mm.

Nanninga et al. [82] showed that elongation and reduction area of the pipeline steels X52, X65 and X100, had a significant reduction after tensile test in a pressurized hydrogen gas (13.8 MPa). This is consistent with the influence of hydrogen on the ductility of the electrolytic hydrogen charged X52 steel, tested by Delafosse and Magnin [83], shown in Figure 17 for various potentials, indicating that the steel was highly vulnerable to HE with a magnitude proportionally to the applied potential. However, their results showed that the presence of electrolytic hydrogen had only a small influence on the yield -and ultimate strength. This agrees with the results from the three pipeline steels investigated by Nanninga et al. [82]. It was stated that gaseous hydrogen did not have a significant influence on either the yield -or tensile strength but most of the loss in ductility can be attributed to high crack-growth rates during tensile test in hydrogen. The results presented by Park et al. [84] also shows a small decrease in yield strength and ultimate strength by 2% and 7 %, respectively. While the decrease in failure elongation was about 40%. Similar trend is also confirmed by other studies for X52 [82, 85, 86] and X65 [82, 85, 86]. Boukourt et al. [87] highlighted the aforementioned effect of hydrogen on the tensile properties, where the effect on yield -and ultimate strength is very poor while the decrease in elongation to failure for various pipeline steels is significant as shown in Figure 18.

However, even if the UTS is generally stable with hydrogen content, the UTS of notched specimens seem to follow the same behaviour as reduction of area with hydrogen. The presence of a notch generates a triaxial stress region ahead of it and a high strain region at the notch root. This results



in a great hydrogen accumulation to these regions and cause increased localized embrittlement of the steel [88].

The altered behaviour of steels when exposed to hydrogen have been described [19, 65] and often referred to as hydrogen-assisted cracking (HAC) or hydrogen-induced cracking (HIC). When the steel specimen undergo tension, a stress concentration gradient causes atomic hydrogen to migrate to locations with greatest stress. As higher concentrations of hydrogen migrate at these locations and causing the embrittlement. The crack continues to grow as hydrogen migrate to the tip of the propagating crack, until the sample is reaching a critical load and finally fractures at an elongation significantly lower than its strength determined without the presence of hydrogen. Brass and Chene [89] stated that the onset of yielding has to occur before hydrogen has an effect since the absorbed hydrogen transported by the dislocations related of plastic yielding play the major role.

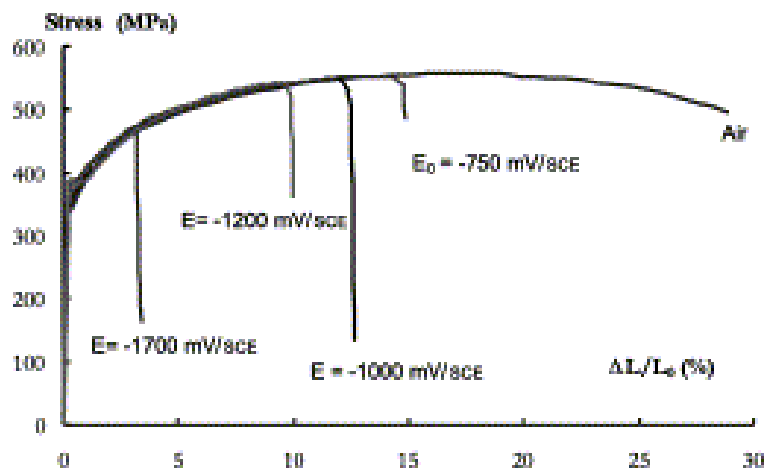


**Figure 17: Stress-strain curves for X52 pipeline steel in air and at different values of electrochemical potential [83].**

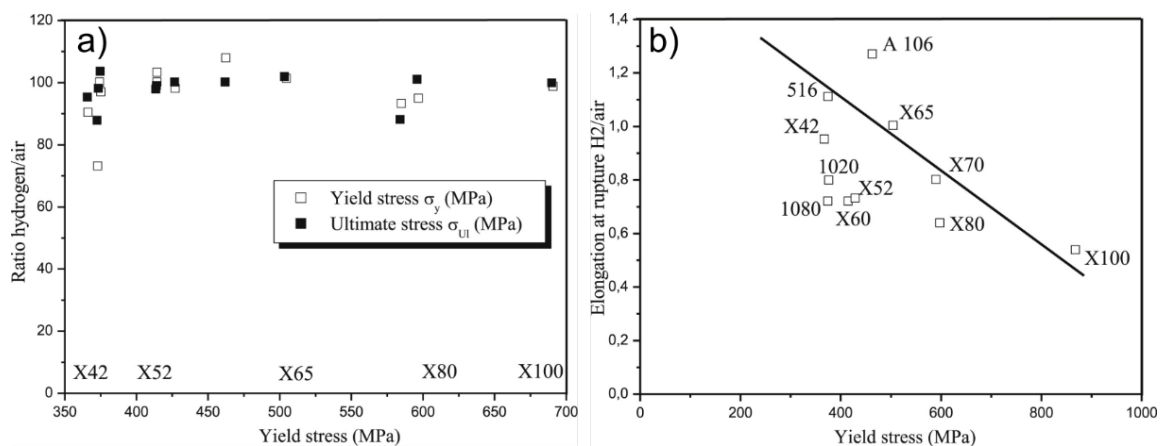


**Figure 18: Influence of a) yield strength on UTS and ratio of UTS in hydrogen and air and b) ratio of elongation at failure in air and hydrogen for different types of pipeline steels [87].**

## 4.2 Grain size Effect on Tensile Properties

Grain refinement is known to reduce internal stresses in the material bulk and remove impurities located along grain boundaries. Also, it plays an important role for hydrogen embrittlement as grain refinement introduce more grain boundaries that can act as barriers for dislocation-induced hydrogen transport. On the other hand, grain boundaries can act as hydrogen trapping sites as well as localized metallurgical features with low decohesion energy. For this reason several studies have investigated the correlation between grain size and HE sensitivity and ultimately it is still a controversial topic [76, 84, 90, 91]. Ghosh and Mondal [90] found no significant variations of tensile and ductility values with hydrogen charging and heat treatment resulting in grain refinement for a ferrite-pearlite micro-alloy steel ( $Y_S=520$  MPa). On the contrary, Chen et al. [91] reported a significant increase in HE resistance with a grain size reduction from  $95\ \mu\text{m}$  to  $32\ \mu\text{m}$  for Fe-Ni steels ( $Y_S=670$  MPa), even though the hydrogen concentration was higher in the small-grained specimens (increase in boundary areas). Takasawa et al. [76] studied the grain size and dislocation density effect in a 45 MPa hydrogen atmosphere in high strength ferritic steels. A reduction in grain size and dislocation density were found to reduce the susceptibility to hydrogen embrittlement. Park et al. [84] performed slow strain rate testing of X60 steel in air and on electrochemically hydrogen charged samples. Their results showed significantly increased HE resistance in fine-grained specimen (Figure 19 (a)) compared to coarse-grained specimen (Figure 19 (b)). Regardless of hydrogen charging,  $Y_S$  is almost constant for each grain size. On the other hand, the displacement and UTS decreased significantly for each grain size. For instance, the total displacement loss was 16.3%, 23% and 40% for the grain sizes of  $14\ \mu\text{m}$ ,  $26\ \mu\text{m}$  and  $35\ \mu\text{m}$ , respectively, as reported shown in Figure 20.

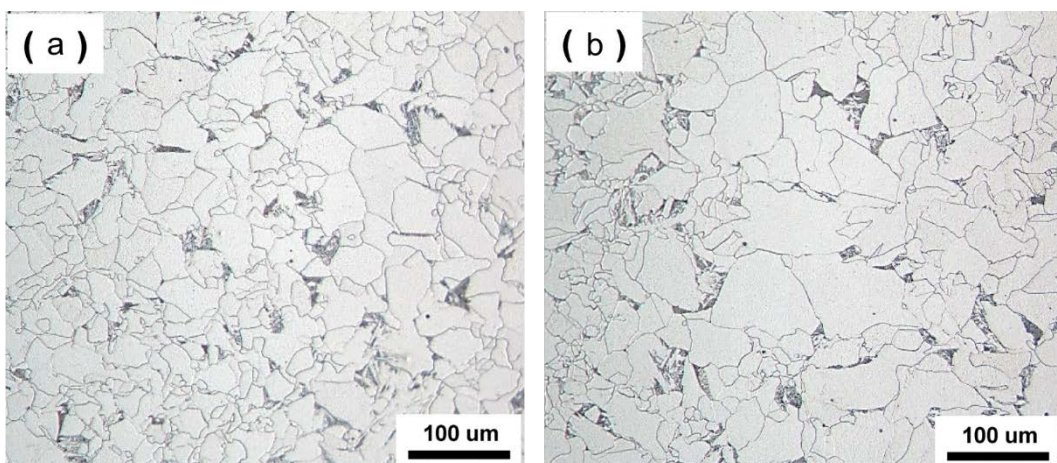


**Figure 19: Light optical micrographs X60 steel , heat-treated for a) 1 h and b) 40h, resulting in average grain sizes of  $14\ \mu\text{m}$  and  $35\ \mu\text{m}$ , respectively [84]. The microstructure consists of polygonal ferrite and pearlite.**

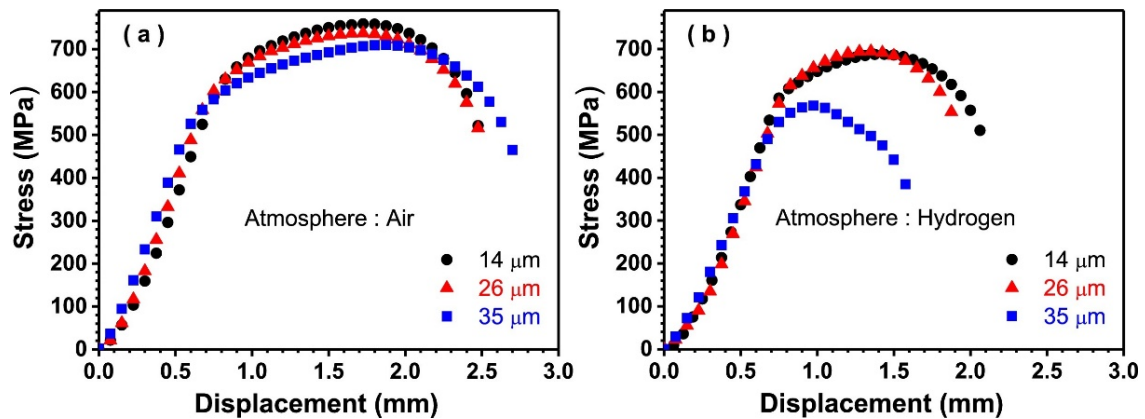


**Figure 20: Engineering tensile-stress-displacement curves for X60 pipeline steel with various grain sizes from tensile tests a) in air and under b) cathodically charged hydrogen condition [84].**

The loss of ductility was also confirmed from their Kernel average mapping (KAM) of EBSD, where the local plastic strain of the sub-fracture surface was measured for the various grain sizes. This method represents the average misorientation of each measurement point with respect to the other neighbouring points within a grain, and correlate plastic deformation (i.e. dislocation density) to misorientation within the microstructure. As shown in Figure 21 (c-e), the red-coloured areas, representing the highest strained zone, was specifically seen in the fine-grained specimen (Figure 21 (c)). In contrast, the specimens with larger grain sizes (26 and 35 μm), displayed nearly no plastic deformation at the fracture surface, indicating less plasticity and dislocation density before fracture.

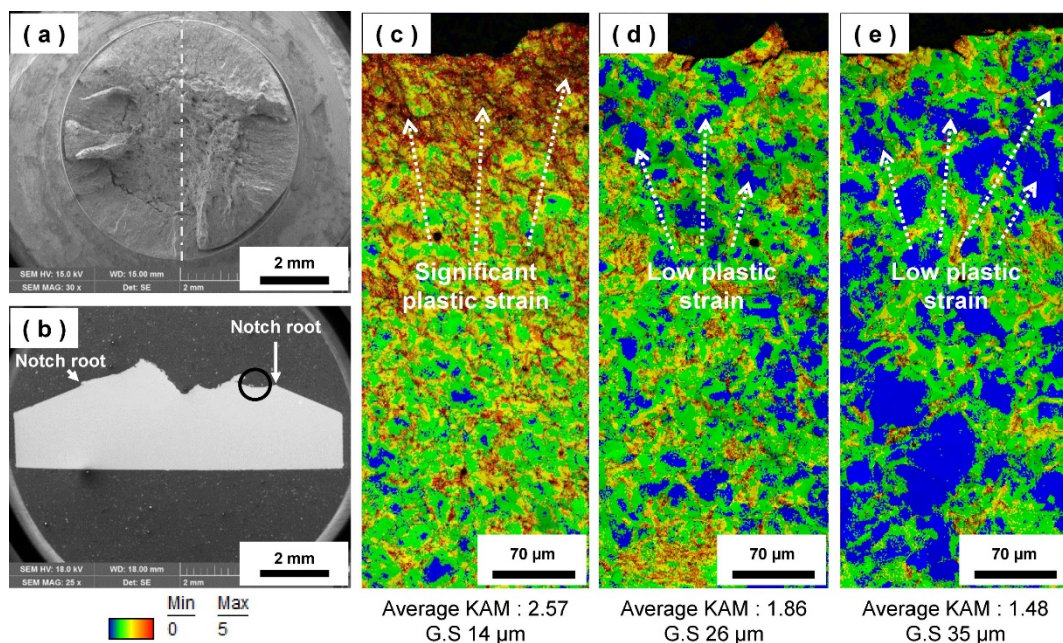


**Figure 21: Kernel average misorientation (KAM) analysis of the b) cross-section below the fracture surface showing decreasing fracture strain with increasing grain size (c-e) [84].**

The aforementioned investigations shows a decrease in YS and UTS with increasing grain size, regardless of hydrogen content, which is in agreement with the Hall-Petch theory [92]. When hydrogen is present, a drastic reduction in elongation at fracture is observed, and this behaviour is even more prominent when the grain size increased. In contrast, the most fine-grained microstructures exhibit superior tensile properties despite having the highest total hydrogen content [84, 91]. The authors correlate the higher hydrogen diffusion in fine-grained microstructures, to the larger grain boundary area with decreasing grain size. Thus, the diffusible hydrogen are believed to be more effectively distributed in the grain boundaries and reduce the normalized amount of hydrogen trapped per unit length of grain boundary [84].

Interestingly, grain refinement is also shown to have contradictory effects on the hydrogen diffusivity. Firstly, as the grain size decrease, the hydrogen mobility will increase due to the larger grain boundary area. On the other hand, there can also be an increased hydrogen trapping effect due to the larger grain boundary network. A microstructure consisting of several fine-grained grains, also have a much higher density of triple junctions, which is the most favourable traps for hydrogen atoms (lowest trapping energy) [93], and will then reduce its mobility [94]. As a result of the two-fold effects, the hydrogen diffusion coefficient will be maximized for a specific grain size, referred to as *the grain boundary cross effect* [95]. It has been shown for pipeline steel, that the maximum diffusion occurs at intermediate grain sizes, and slower diffusion rates occurs for fine and very coarse microstructures. One example of this is shown in the work by Yazdipour et al. [94], who investigated the grain size effect on hydrogen diffusivity of X70 steel with various grain sizes, using cellular automation (CA) modelling. A 3D demonstration of their results, showing a peak value of diffused hydrogen atoms in the intermediate grain size of 12.2  $\mu\text{m}$ , are shown in Figure 22.

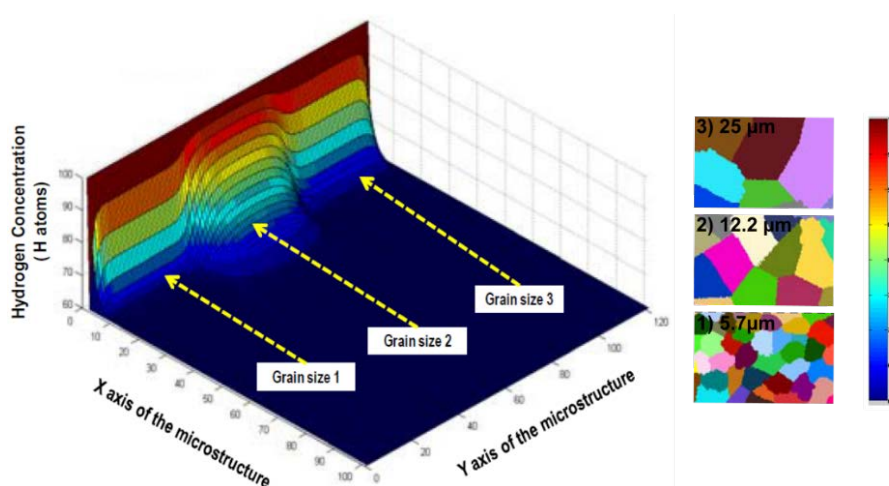


**Figure 22: Progress of hydrogen diffusion as a function of increasing grain size (from 5.7  $\mu\text{m}$  to 25  $\mu\text{m}$ ) for X70 pipeline steel, adopted from [94].**

### 4.3 Effect of Microstructure Banding

Commercial pipeline steels usually consist of banded microstructures in which alternating layers of ferrite and pearlite are elongated in the rolling direction [96]. This results in a microstructure that is highly anisotropic and mechanical properties are shown to vary as a function of orientation. Also, different degrees of HE susceptibility in steel can be dependent on the reciprocity of the loading direction with respect to the banding direction. However, this seems to still be a topic which without a full consensus.

From the work of Nanninga et al. [82] the influence of specimen orientation relative to the pipe axis was evident in the tensile stress-strain curves for X52 and X65, Figure 23. The microstructure consisting of ferritic grains and pearlite, were generally banded along the longitudinal direction of the pipe. The X52 steel appear to have less anisotropy than X65, suggested to be related to the higher degree of anisotropy in the ferrite grain morphology for X65. There is no indication of orientation-dependent hydrogen resistance from the stress-strain data, other than the expected effect from the pipe-forming process and hydrogen influence of the alloy in general. However, the fracture surface indicate that HE is more evident in the transverse direction, particularly for the X52 alloy, shown in Figure 24. The authors report quasi-cleavage fracture for both alloys. However, the cleavage packets were more significant in the transverse direction and slightly more ductile tearing was observed in the longitudinal directions. Additionally, smaller packet sizes were observed for X65 (X65 had a higher degree of morphological anisotropy). The authors assume an overall higher hydrogen diffusion rate and lower HE resistance in the transverse direction since hydrogen diffusion and cracking are suggested to occur more rapidly for this orientation since the elongated ferritic grains and pearlite bands are perpendicular to loading axis in the transverse direction but parallel to the crack propagation.

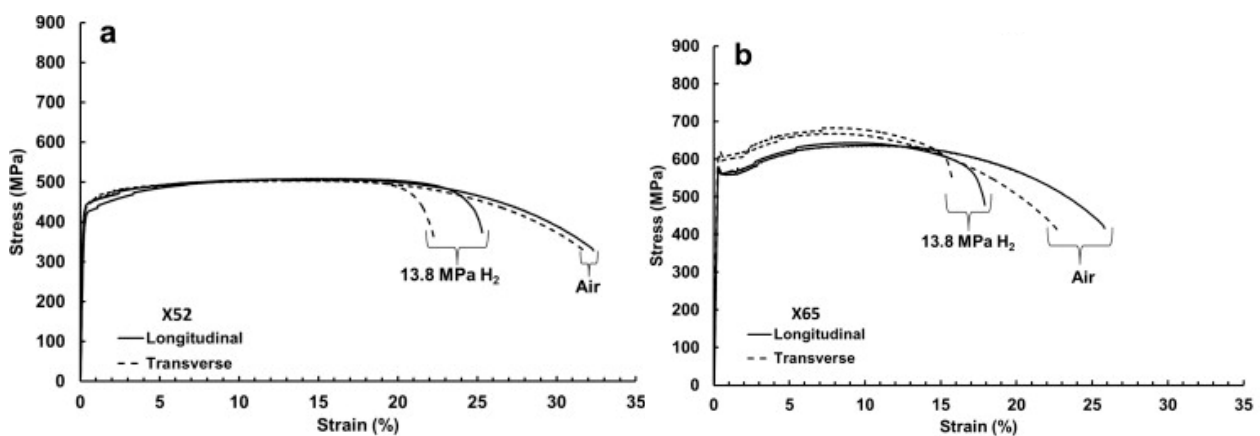


**Figure 23: Stress-strain curves from tensile tests in air and pressurized hydrogen (13.8 MPa hydrogen gas pressure) for a) X52 and b) X65 in both transverse and longitudinal direction [82].**

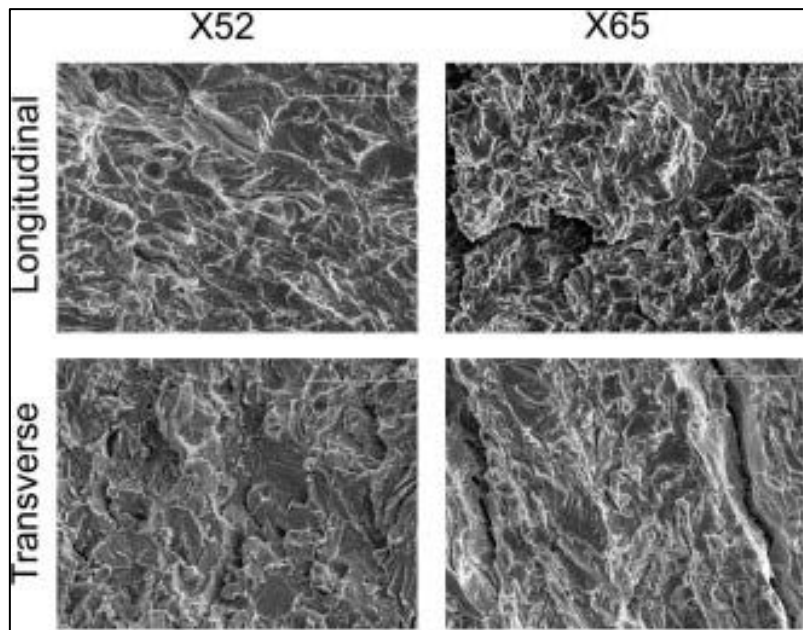


**Figure 24: SEM fractography of hydrogen tested X52 and X65 specimens in transverse and longitudinal direction [82].**

Marina et al. [97] performed slow strain rate tests of X65 pipeline steels produced by hot rolling and controlled rolling. A slightly higher diffusivity coefficient is obtained in the sample processed with controlled rolling. Furthermore, there were no evidence of anisotropy of the hydrogen diffusivity related to the rolling direction. The authors question if the specimen thickness is appropriate compared to the grain dimension (from 9.4 to 25  $\mu\text{m}$ ), to allow for examination of potential differences of the diffusivity in the different directions. However, it was verified that hydrogen diffusion coefficient was lower for ferritic-bainitic steel (X100) compared to a ferritic-pearlitic steel (X60). Moreover, the diffusion coefficient decreased with nearly 50% in the transverse direction for the X60 steel, while no change occurred in the X100 steel. The X60 steel consisted of a coarse microstructure with the presence of manganese sulphur inclusions, formed by hot rolling.

#### **4.4 The role of Grain Boundary Character and Texture**

Among several methods employed in the pipeline production, thermomechanical controlled processing (TMCP), a process that combine controlled hot rolling and accelerated cooling, is considered as one of the most reliable method for obtaining optimal mechanical properties [98]. The steel plate is exposed to both tensile and compressive stresses during the rolling process that may introduce microstructural inhomogeneity across the thickness of the pipeline steel. Grain Boundary Engineering and crystallographic texture control appear as a more innovative approach to improve the resistance to the pipeline's environment and ultimately reduce the risk of hydrogen-

assisted failures in service pipelines. It is well known that the role of microstructure and texture affects the role of cracking behaviour. For instance, high angle grain boundaries (HAB) have higher energy than low angle boundaries (LAB) and special coincident lattice site (CSL) boundaries, therefore they provide an easy path for crack propagation [99-103]. Moreover, it also plays a role in different types of cracking, e.g. fatigue cracking and hydrogen embrittlement [103, 104] as well as it directly influence the anisotropy of the mechanical properties, ductility and toughness [105].

Arafin et al. [102] investigated the influence of grain boundary character and crystallographic texture on the intergranular stress corrosion cracking (IGSCC) of a X65 pipeline by using SEM, EBSD and X-ray texture measurements. By using X-ray diffractometer it was revealed that the fraction of high angle boundaries (HAB) were much higher on the outer edge of the pipe and gradually decreased towards the mid-thickness region, where the low angle grain boundaries were dominant [102], as shown in Figure 25. Increased susceptibility to hydrogen damage at the top surface layer can be linked to higher strength and lower ductility, due to microstructural changes towards the mid-thickness. Both grain boundary character and texture were found to influence the cracking resistance. While HAB are susceptible to cracking, LAB and CSL are suggested to be more crack-resistant. Also, the boundaries of  $\langle 100 \rangle \parallel$  rolling plane (RP) textures grains were most susceptible, found to be most dominant along crack propagation paths. It was evident from the calculated elasticity modules, that the  $\langle 100 \rangle \parallel$  RP had the highest modulus of 230 GPa, and more likely to undergo cracking.

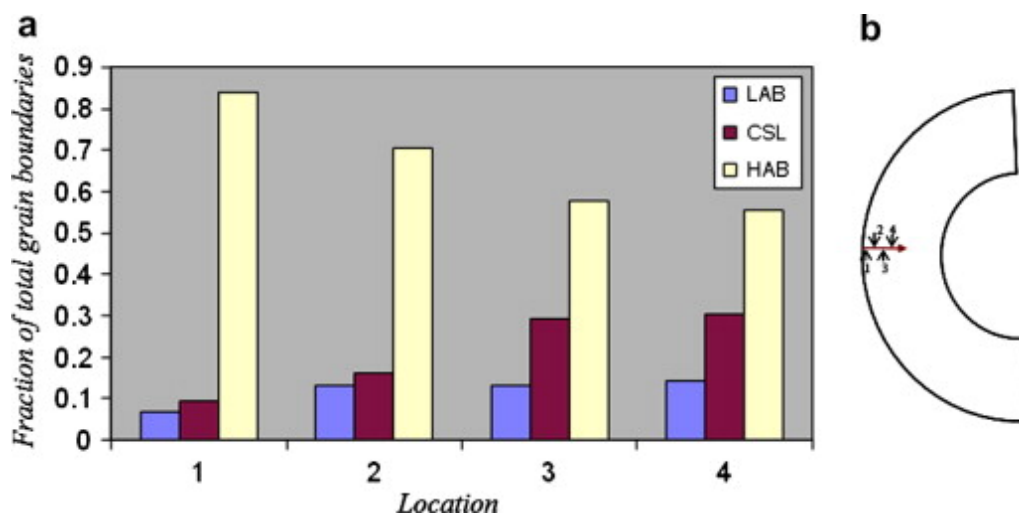


**Figure 25: (a) Grain boundary character distribution from the outer surface of the pipe towards the mid-thickness and (b) the corresponding measurement locations on the pipe [102].**

The work by Venegas et al. [103] showed that microstructure and texture have a strong effect on hydrogen assisted crack path for X46 steel by investigating the strain fields surrounding hydrogen-induced cracks, and the influence shear stress distribution on the crack propagation path. In agreement with the work by Arafin et al. [102] intergranular propagation path are mainly HAB.

Furthermore, for the X42 steel, the propagation path consisted of less than 18% of CSL and LAB's. This observation is consistent with the statement from Watanabe [100], that low angle boundaries and CSL's are more resistant to fracture than high-energy/high-angle boundaries. The correlation between the hydrogen assisted crack path and the crystallographic features was examined and showed the different nature of crack behaviour with the presence of suitable oriented crystallographic planes and HAB. Figure 26 shows that the hydrogen assisted cracks consist of many large strained areas due to interaction between approaching cracks. A darker colour scale indicates a higher deformed area. The crack tips, noted A, C and D does not show an extended plastic zone. In contrast, crack tip B, had a strained zone up to 30  $\mu\text{m}$ . EBSD analysis confirmed that the crack tips A, C and D had suitable oriented slip planes in the crack path. (45 degree between slip plane and normal), favouring deformation by shear. Thus, relaxation of the shear stress occurs. This was not the case for crack tip B, since there were no cleavage planes suitably oriented for planar propagation in and lack of HAB to propagate along. Instead, the crack tip propagates directly through HAB in its planar direction and into a ferritic grain where it arrests and subsequently developing local high stresses, indicated by the dark grey area in front of the tip in Figure 26 (a). Controlling crystallography texture and improving grain boundary engineering are suggested to be important methods for improving the HE resistance in pipeline steels. This could be achieved by thermomechanical treatments resulting in a lower fraction of HAB [103].

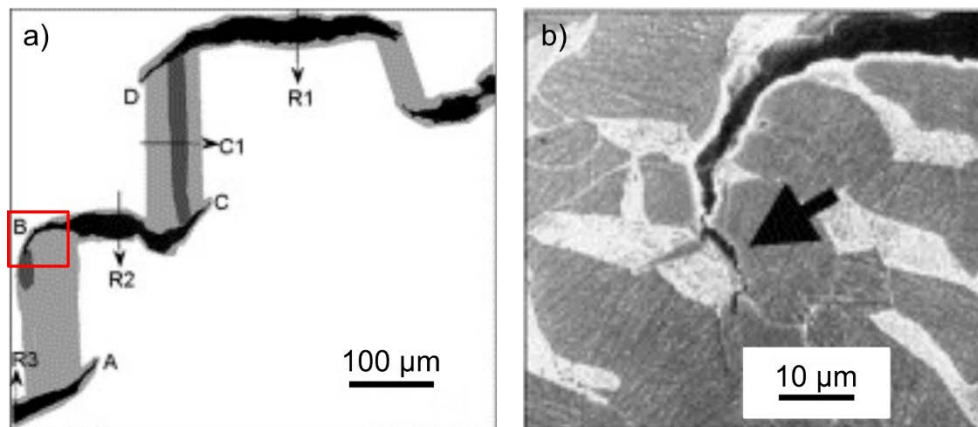


**Figure 26: (a) Strain fields surrounding the cracks (b) micrograph of crack tip from the inset in (a). Figure adopted from [103].**

#### 4.5 Hydrogen Effect on HAZ Tensile Properties

Hydrogen embrittlement occurring in pipeline steel is mainly associated with the presence of the presence of local brittle metallurgical features, typically in the HAZ, which is ascribes to the presence of martensite, commonly recognized as one of the most susceptible microstructure to HE [5]. It has been demonstrated that the solubility of hydrogen in HAZ is higher than in the base metal. The heat-affected zone introduced after welding consist of microstructures that can be prone to hydrogen embrittlement, such as acicular ferrite (AF), widmanstatten ferrite (WF) bainite and martensite



depending on the welding procedure and the inferred thermal cycles. Despite that this area of the pipeline is a great concern for the oil and gas industry due to the high risk of hydrogen defects in these areas, only a small amount of investigations focuses on the HAZ and welding properties. The few ones available highlight the importance and challenges of increased hydrogen embrittlement susceptibility in HAZ.

Davani et al. [86] investigated correlation between different microstructures resulting from thermomechanical processes on strength and hardness in the presence of hydrogen in both the base metal, weld metal and HAZ for X65 pipeline steel. Tensile strength decreased with an average of 6% and yield strength increased by about 5% for the base metal. Elongation of all base metal samples decreased by an average of 32% due to hydrogen charging. Percentage of ductile fracture was reduced by an average of 45%. For HAZ sample, tensile strength decreased about 4%, yield strength was about 7% higher and elongation was reduced by 40-70%, due to hydrogen charging. Similar trend was reflected in the microhardness tests with an increase of 13 % for HAZ and 10% for base metal immediately after charging, shown in Figure 27. The results also show evident loss of hydrogen in the sample after 5 min, resulting in a decrease in hardness as the reduction occurs. The percentage of ductile fracture decreased by an average of 48 % for HAZ samples. The fracture morphology clearly changed after the exposure to hydrogen, shown in Figure 28, going from a quasi-cleavage fracture to brittle fracture in the absence and presence of hydrogen, respectively.

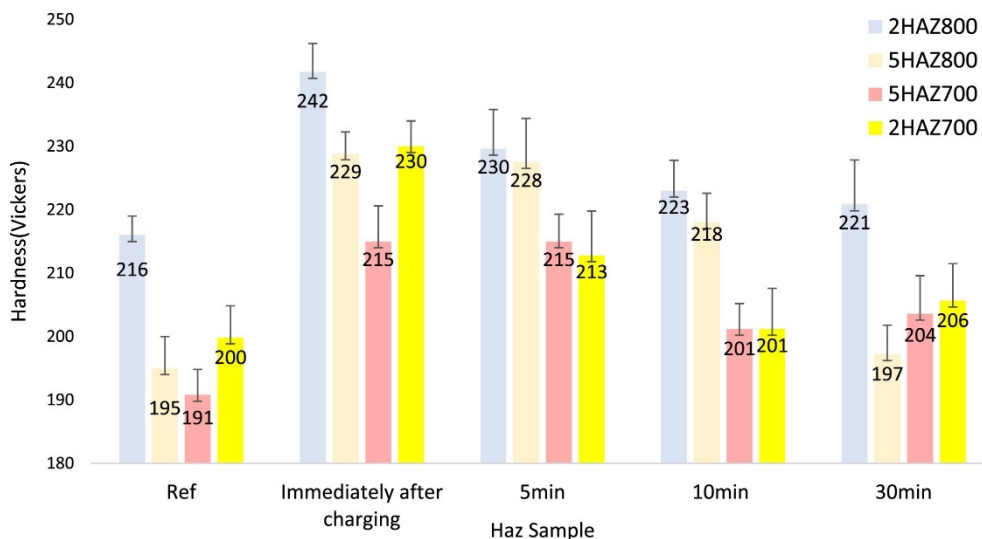


**Figure 27: Hardness values of HAZ with different rolling conditions in a X65 steel. The label for each sample indicate the number of rolling-passes (two or five) and the final rolling temperature (700°C or 800°C) [86].**

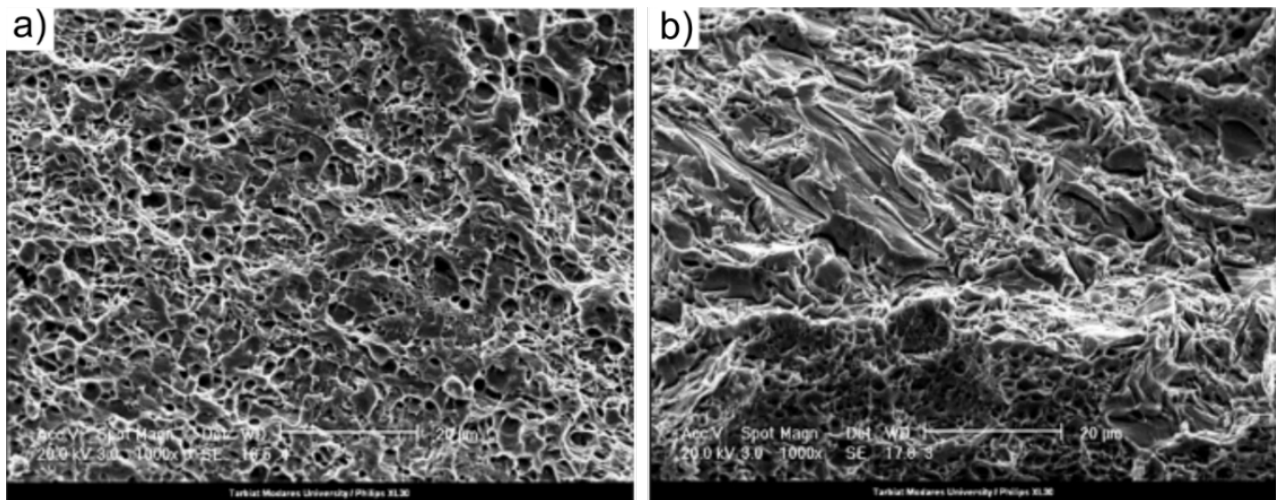


**Figure 28: SEM images of fracture surface of HAZ for X65 pipeline steel after tensile test a) without hydrogen and in b) hydrogen [86].**

The effect of hydrogen on strength properties of HAZ is shown to be higher than in the base metal, correlated to the higher amount of hydrogen absorption by the microstructure, which was mainly acicular ferrite (AF). The amount of diffusive hydrogen is also affected by the microstructure with the grain size and percentage of the hard phase of the base metal under different rolling conditions. The major microstructure in the HAZ is acicular ferrite. This microstructure contains several features that tends to trap hydrogen, such as high dislocation density, HAB and fine grains. The rate of hydrogen trapping in acicular ferrite is greater than in ferrite/pearlite.

Latifi [106] studied the effect of microstructure on hydrogen diffusivity by testing the base and weld metal of X65 pipeline steel. His results showed that the ferritic matrix and the pearlite/bainite islands in the base metal had the lowest hydrogen diffusion while the most diffusive hydrogen was related to the acicular ferritic microstructure in the weld metal.

## 5 Fracture Mechanical Properties

Fracture toughness values are typically presented in the literature in terms of  $K_{IC}$  (plane strain fracture toughness),  $J_{IC}$  (elastic-plastic fracture toughness in terms of J-integral), crack growth resistance or J-R curve and  $dJ/da$ , the slope of the fracture resistance curve related to the tearing capability of the material. The Elastic plastic method generally involve generation of J-R curve for the material, which is a plot of the materials resistance to crack extension using the J-integral as a function of stable crack extension. Specific requirements on the specimen geometry must be satisfied in order to determine the fracture toughness from the J-R curve, the plain-strain fracture toughness  $J_{IC}$ . Elastic plastic stress/strain intensity field in front of a crack, indicated with  $J$ , can be converted to the linear stress intensity factor from the following relation:

$$K = \sqrt{\frac{JE}{(1 - \nu^2)}} \quad (22)$$

where  $E$ , denoted that the stress intensity factor  $K$  was determined from a value of  $J$ , is the elastic modulus of the material and  $\nu$  is the Poisson's ratio of the material. Fracture toughness can be substantially affected in the presence of hydrogen. For this reason, fracture mechanical properties are very important property in the design of large steel components, such as pipeline steels, where the presence of small, non-detected cracks is often unavoidable.

It has been well documented that hydrogen can greatly reduce fracture toughness of pipeline steels and their weldments by promoting brittleness (in otherwise ductile materials) [81, 107]. The variation of the values of fracture toughness, both linear elastic ( $K_{IC}$ ) and elastic-plastic ( $J_{IC}$ ), with respect to temperature and hydrogen pressure generally follow the same trends seen in reduction of area in tensile test: decrease in toughness with increasing pressure and hydrogen charging. The presence of hydrogen results in significant loss in fracture toughness and crack propagation resistance. In the presence of hydrogen gas, this decrease is shown to continue with increasing hydrogen pressure.

### 5.1 Fracture Toughness

Fracture mechanical tests have been performed on a variety of steels, providing data for plane-strain fracture toughness,  $K_{IC}$  and elastic plastic fracture toughness,  $J_{IC}$ . In the earlier 1980's work, the current authors [80, 81, 108, 109] showed with fracture mechanical testing experiments, that the presence of hydrogen results in significant losses in fracture toughness and crack propagation resistance. However, many investigations showed that the requirements for elastic fracture mechanics validity in ASTM E1820 are not met, i.e., the maximum stress intensity factor for the tests in air and hydrogen are not valid plain strain fracture toughness, and therefore a conditional

toughness value as  $K_Q$  and  $K_{IH}$  respectively have been reported. Table 5 shows the fracture mechanical properties of several low-carbon steel tested up to a hydrogen pressure of 16 MPa.

Robinson and Stoltz (1981) [108] performed J-R curve testing using double-edged notched specimens of a A516 Grade 70 steel (0.21% C, 1.04% Mn) in air and at hydrogen pressures from 3.45 to 34.5 MPa. The crack resistance curve, shown in Figure 29, shows that the hydrogen effect is prominent even at low pressures, i.e. 3.45 MPa. This was also confirmed by the change in fracture mode. The crack initiation,  $J_{IC}$ , was related to fracture of ferrite that is controlled by the hydrogen-dislocation interaction.

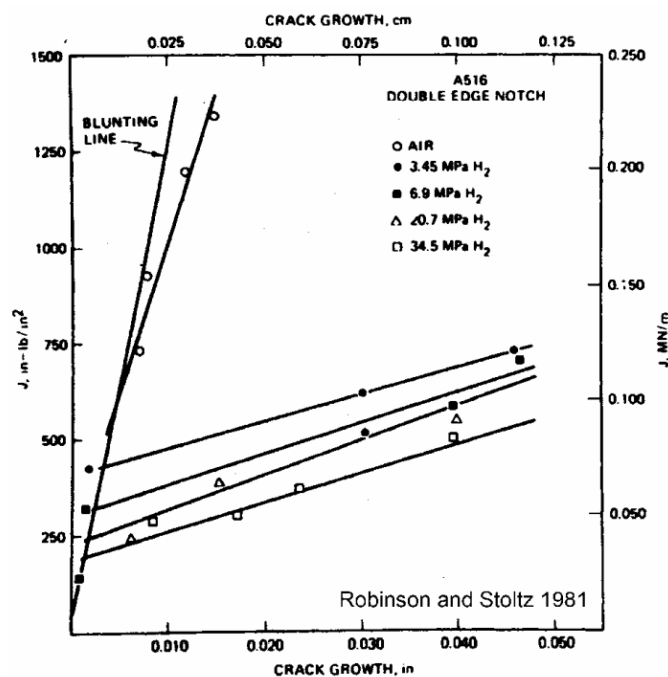


**Figure 29: Crack growth resistance curve for A516 Grade 70 in air and at hydrogen gas pressures from 3.45 to 34.5 MPa [108].**

Similar to the work by Robinson and Stoltz [108], fracture toughness was established from burst tests in the research by Gutierrez-Solana and Elices [110]. They investigated a spanning transmission pipeline material (comparable to X42 pipeline steel) in hydrogen pressures up to 16 MPa. The burst tests were conducted on pipes with various longitudinal machined cracks, from which the fracture toughness was estimated using plane strain fracture toughness,  $K_{IC}$ . In addition, three-point bend testing was performed in hydrogen pressures up to 6.5 MPa, in combination with finite element analysis to accommodate the experimentally obtained J-integral values. The data are shown in Figure 30 (a), together with results from the burst tests. Fracture toughness decreases as hydrogen pressure increases but appears to be approaching a threshold limit at a hydrogen pressure of 20 MPa. Furthermore, the toughness values were reported to also strongly depend on the loading rates, as shown in Figure 30 (b) presenting fracture toughness values in 4 MPa hydrogen pressure

at displacement rates from  $3 \times 10^{-5}$  to  $3 \times 10^{-3}$  mm/s. Fracture toughness is nearly constant from  $3 \times 10^{-5}$  to  $3 \times 10^{-4}$  mm/s, but increase with about 30% when displacement rate increases to  $3 \times 10^{-3}$  mm/s.

A comparison of both steels; the X42 and A516, from the work by Robinson and Stoltz [108] and Gutierrez-Solana and Elices [110], are shown in Figure 31. Both datasets clearly show that exposure to hydrogen gas can significantly lower the fracture toughness as the gas pressure increases, and eventually reach a threshold value that does not vary in relation to further increase of hydrogen pressure. It is noted that A516 obtain considerably higher fracture toughness values than X42, which is presumably an effect of the higher displacements rates used for this material, despite twice as much higher carbon content in A516 than X42.

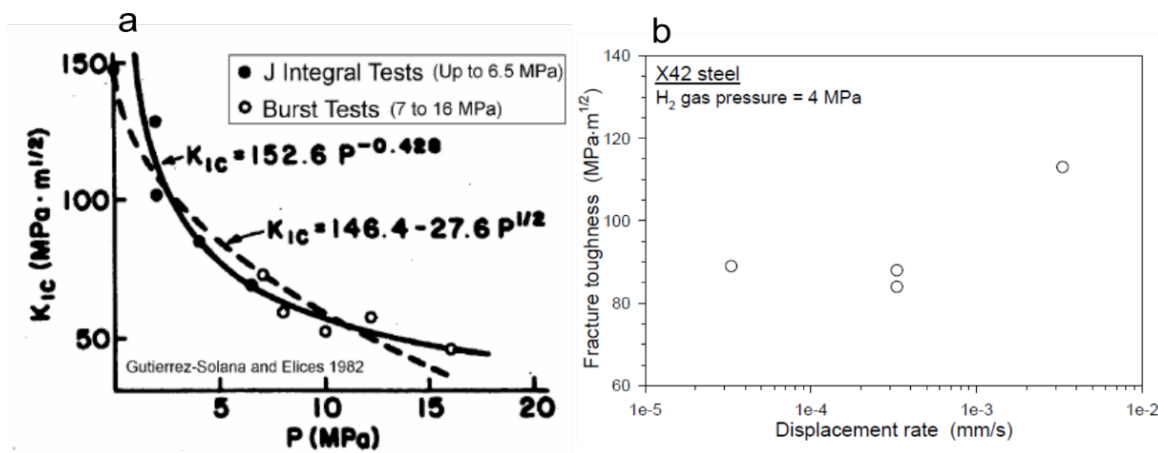


**Figure 30: (a) Fracture toughness from both J Integral tests and Burst tests in hydrogen gas. (b) Effect of displacement rate on fracture toughness in hydrogen gas for X42 steel [110].**

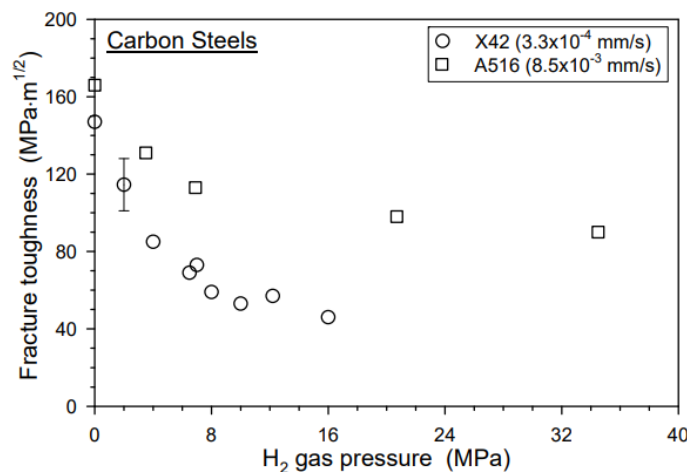


**Figure 31: Effect of hydrogen pressure on fracture toughness for a X42 [109] and a A516 [108] carbon steel at displacement rates of  $3.3 \times 10^{-4}$  mm/s and  $8.5 \times 10^{-3}$  mm/s, respectively.**

When performing testing in hydrogen gas, it is likely that the test environment contains some gas impurities such as oxygen. The degree of hydrogen gas purity is not identified in all available

literature. In order to correctly evaluate the effect of hydrogen on the material strength, it is critically important to control this. Work at Battelle Columbus Laboratories (Battelle) have been performed to confirm hydrogen degrading findings on pipeline steels from Sandia laboratories from the early 1980`s. The systematic investigation of the effect of inhibitors on fracture and fatigue of pipeline steels in hydrogen gas as a function of microstructure has been one of the major tasks. Some of the key point of their findings was the significant reduction in fracture toughness for medium strength steels, when exposed to hydrogen gas, as shown in Figure 32.

The investigation by Cialone and Holbrook (1988) [81] included *J*-resistance elastic plastic fracture testing of X42 and X70 pipeline steel in various gaseous environments, including methane, carbon monoxide and carbon dioxide with a total pressure of 6.9 MPa, independent of gas composition. The fracture toughness is about 50% lower in pure hydrogen gas versus the toughness in nitrogen or methane (used to simulate natural gas). Another key observation is that gas mixtures containing both hydrogen and carbon monoxide appear to have a minor effect on fracture toughness. The original toughness in the steel is restored in the tests when the hydrogen/CO ratio is 60/24 (Figure 32). The authors explain the positive effect of carbon monoxide in hindering hydrogen-assisted fracture by its role in limiting hydrogen uptake into the material.

Collectively, the studies from the 1980`s outlines the critical role of hydrogen in affecting the material resistance to cracking and highlights the need for a clarification and a deeper understanding of the interplay between microstructure and hydrogen influence, triggering the interest of several recent researchers to investigate this topic.

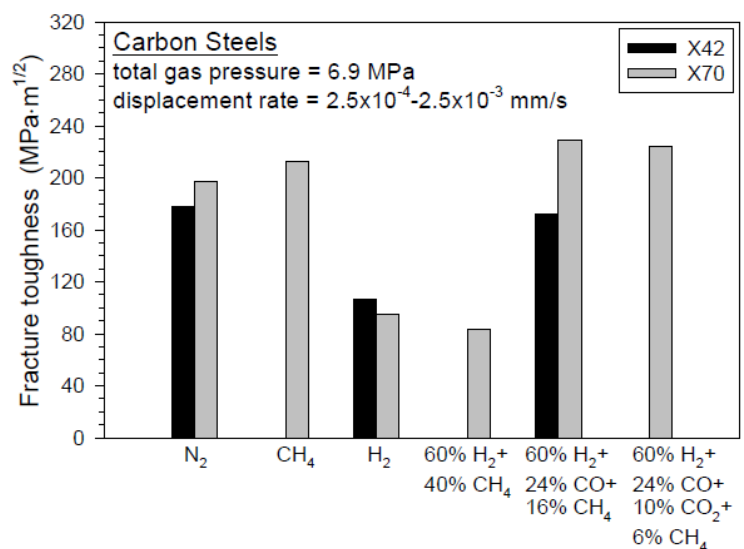


**Figure 32: Effect of gas composition of fracture toughness for API 5L X42 and X70 pipeline steels [81].**

## 5.2 The Influence of Microstructure

Zawierucha and Xu (2005) [111] performed Charpy V-notch impact tests, elastic-plastic fracture toughness test and constant load fatigue tests on a API 5L Grade B steel (0.18 % C, 1.06 % Mn) as-rolled and normalized. Young's modulus, UTS, elongation and reduction of area was increased from 299 MPa, 518 MPa, 28 % and 54.9 %, respectively, to 371 MPa, 539 MPa, 32.9% and 61% after normalization. The effects of hydrogen on the J-R curve and on  $J_{IC}$  as a function of increasing hydrogen pressure for this material is shown in Figure 33 (a) and (b), respectively. A gradually decreasing  $J_{IC}$  with increasing pressure is reported.

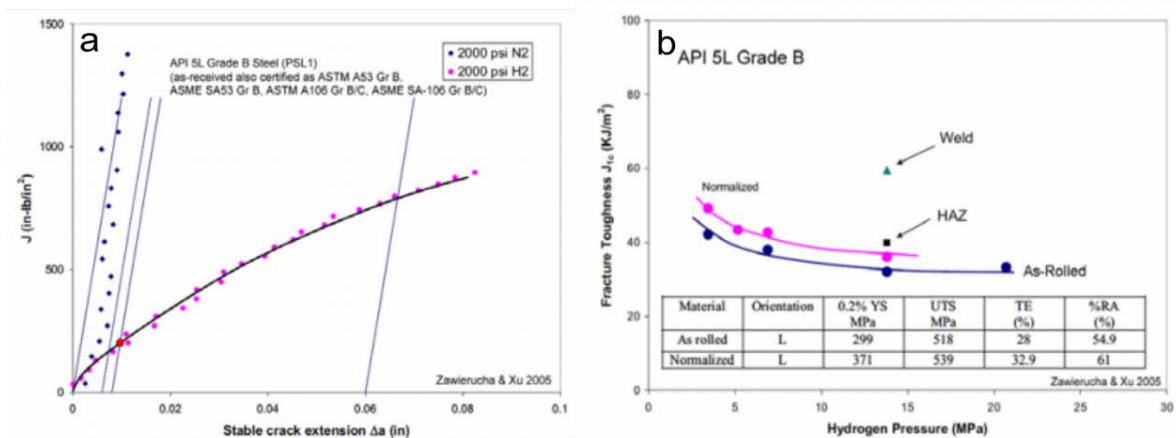


**Figure 33: (a) J-R curve for API 5L Grade B in 13.8 MPa nitrogen -and hydrogen pressure and (b) the  $J_{IC}$  as a function of increasing hydrogen pressure for both as-rolled and normalized condition [111].**

Capelle et al. [112] investigated the hydrogen effect on the fracture toughness (stress intensity factor at initiation since  $K_{IC}$  is not valid according to standard) for several pipeline steels, including X52, X70 and X100. Using Compact Tension (CT) specimens before and after electrochemical hydrogen charging in NS<sub>4</sub>, fracture toughness decreased with about 14 %, 5% and 1% for X52, X70 and X100, respectively. The fracture toughness measured in hydrogen charged environment was relatively close to that obtained in air, shown in Figure 34. Furthermore, the hydrogen sensitivity decreased with increasing yield strength of the pipeline steel. (It is noted that the X52 pipeline steel is produced in the 1960's, and steel properties are expected to be improved since then.) Hydrogen-air fracture toughness ratio from both electrolytic and 6.9 MPa gaseous hydrogen (circle) charging is shown in Figure 35 (Figure from [87]), versus the material yield strength. Data from other pipeline steels are also included for comparison (No reference to the other materials is given). The average value indicate that fracture toughness is reduced with 1/3 due to hydrogen damage. It should be noted that there is a considerable amount of scatter in the data plot. It has to be pointed out that no explanation about material and test procedures are given for this plot.

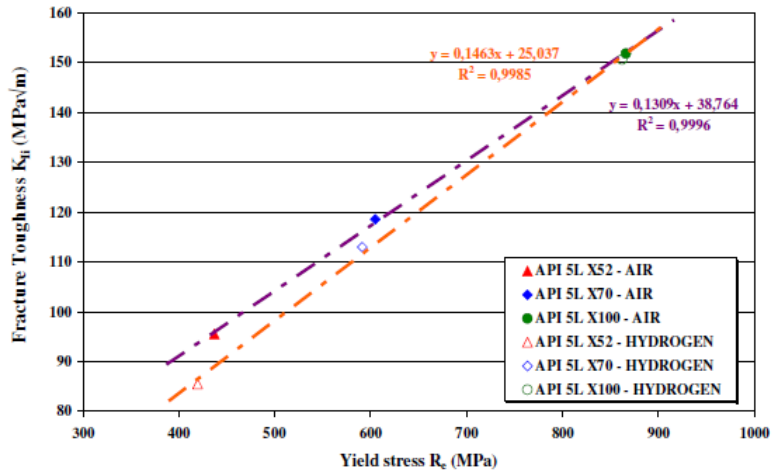


**Figure 34: Hydrogen effect on fracture toughness for API 5L X52, X70 and X100 pipeline steels [112].**

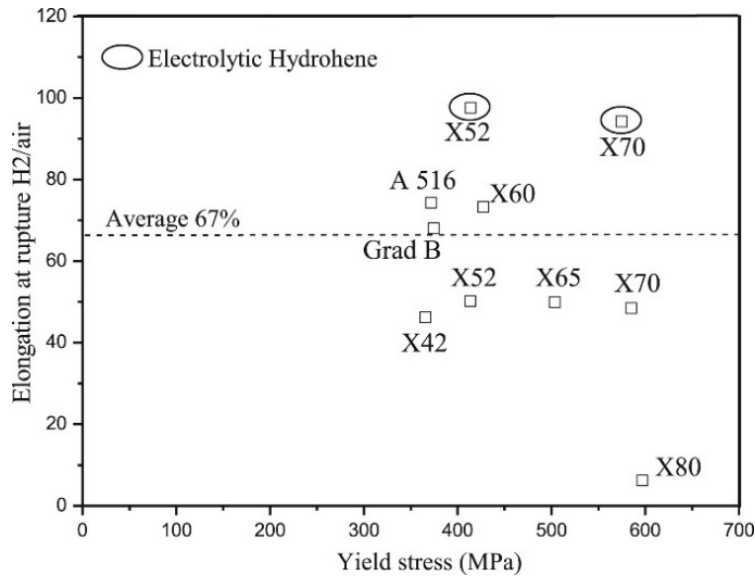


**Figure 35: Hydrogen-air toughness ratio versus yield strength for various pipeline steels [87]**

San Marchi et al (2010) [113] studied the resistance to hydrogen-assisted fracture of two pipeline steels in high-purity hydrogen gas at the pressures of 5.5 MPa and 21 MPa using EPFM methods consistent with the methodology outlined in ASTM E1820-09. The measured fracture toughness values are denoted  $J_Q$  and  $K_{I,Q}$  since they don't meet the requirements of ASTM E1820 for a straight crack extension. The two alloys used in this study, are referred to as alloy B (X70/X80) and D (X60) with yield strength of 565 and 434 MPa, respectively (Details of chemical composition and mechanical properties are shown in *Appendix A*). From the CT testing, the fracture toughness of the two alloys were in the range 80-100 MPa√m in gaseous hydrogen. Although the fracture toughness measured for the X80 pipeline steel was higher than that obtained in X60, values from both materials are in agreement with previous reported values for pipeline steel in the same pressure range [114], shown in Table 5.



Increasing pressure from 5.5 MPa to 21 MPa did not induce any significant changes in toughness values. The average values are presented in Figure 36 from specimens both precracked in hydrogen and in air. The change in fracture toughness is mainly related to the hydrogen pressure and precracking in this work. However, it is noted that the datasets contains some uncertainty (indicated by error bars in Figure 36), indicating that the differences are relative small. In particular for the X60 (alloy D). Nevertheless, since hydrogen diffusion is relatively fast in ferritic steels, this is not considered as a major contributor do degrading the fracture toughness. Both of these alloys predominantly consist of a polygonal ferrite. Although, alloy B (X80) contains 10% coarse acicular ferrite. Hydrogen trapping efficiency have been found to be more prominent in acicular ferrite [15] than in degenerated pearlite and bainite/ferrite.

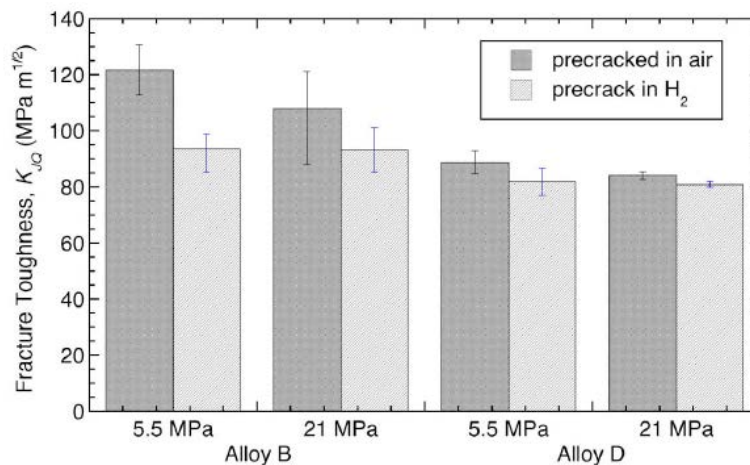


**Figure 36: Fracture toughness of alloy B(X70/80) and D (X60 HAC).**

### 5.3 Effect of Current Density

Electrochemical hydrogen charging, that is, cathodic polarization of the specimens in electrolytes in either galvanostatic or potentiostatic way, is one of the methods commonly used for hydrogen charging. The electrochemically charged hydrogen content can be controlled by changing the solution and the current density or polarization potential. The dominance of one or more HE mechanisms depends on the total hydrogen diffusion and concentration near the crack tip during the experimental hydrogen charging. The accumulation of hydrogen is a critical factor to consider in order to understand the HE mechanisms occurring. This is strongly dependent on the material, mechanical loading conditions and environment.

Previous work indicate that pipeline steel may exhibit large degradation of mechanical properties up to an applied current density of approximately 10 mA/cm<sup>2</sup>. In particular, Hardie et al. [115] investigated X60, X80 and X100 cylindrical specimens and observed a significant loss in ductility in terms of reduction in area, after cathodic charging. The degree of embrittlement for the X60 steel, reached a maximum at 10 mA/cm<sup>2</sup> after a loss of 64% RA. (More details from this study are found

in the previous section "*Tensile Properties*".) Moreover, one of the experimental studies by R.Wang [116] indicated that a non-mediated appearance of both HEDE and HELP occurred in a low carbon pipeline steel, X70, depending on the charging method. The study included fracture toughness testing (in accordance with ASTM E399-90) of single edge notch specimens under hydrogen pre-charging and dynamic hydrogen charging conditions, using current densities in the range of 1-1000 mA/cm<sup>2</sup> and 1-100 mA/cm<sup>2</sup>, respectively. During hydrogen pre-charging, hydrogen-assisted fracture toughness,  $K_{IQ}$ , obtained linear decrease in relationship with increasing hydrogen concentration above *the critical charging current density*, i.e.  $i=25\text{mA/cm}^2$ . The critical current density corresponds to the critical hydrogen concentration of 1 ppm, at which below hydrogen-assisted hardening dominated and increased the  $K_{IQ}$  up to a maximum. The increase of  $K_{IQ}$ , during hardening occurs as a result of the interaction between hydrogen atoms and dislocations, leading to solute strengthening from interstitial atoms of hydrogen and restricts the movement of dislocations [117].

The variation of fracture toughness with current densities (at a pre-charging time of 48 hours) are shown in Figure 37 (a). The fracture morphology, shown in the insets, revealed microvoid coalescence fracture, with a reduction of dimple size with increasing current. Such reduction was attributed to the HELP mechanisms; the increasing hydrogen concentration reduce the critical stress and strain of void nucleation, hence the reduction of formation energy of vacancy and free surface, accelerates the void nucleation and subsequently the dimples on the fracture surface become smaller [118].

The X70 steel demonstrate a different behaviour with dynamic hydrogen charging; for current densities between 1 and 10 mA/cm<sup>2</sup> the reduction of the fracture toughness parameter,  $K_Q$  is fast and slow above applied current density of 10 mA/cm<sup>2</sup>, as shown in Figure 37 (b). The fracture toughness parameter,  $K_{IQ}$ , decreases with 30% from current density 1 to 10 mA/cm<sup>2</sup>. Even 1 mA/cm<sup>2</sup> is enough to embrittle the pipeline steel in this test. In contrast, for the pre-charged condition, hardening is present at 1 mA/cm<sup>2</sup> and increase the toughness. Between 10 and 100 mA/cm<sup>2</sup>,  $K_{IQ}$  decreased only with additional 12%. This lack of dependence on fracture toughness after 10 mA/cm<sup>2</sup> is supported by other investigators as well [51, 67, 115]. This is often related to the fact that, during dynamic hydrogen charging, a strong interaction should exist between hydrogen diffusion and local stress ahead of the crack in the pre-cracked specimens. The hydrostatic stress formed at a distance ahead of the crack tip will assist hydrogen diffusion. Compared to the pre-charged condition, dynamic hydrogen charging lowers the fracture toughness considerably. Moreover, the fracture surface morphology consisted of typical cleavage facets, attributed to brittle fracture as a result of the mechanism of HEDE, shown in SEM insets in Figure 37 (b).

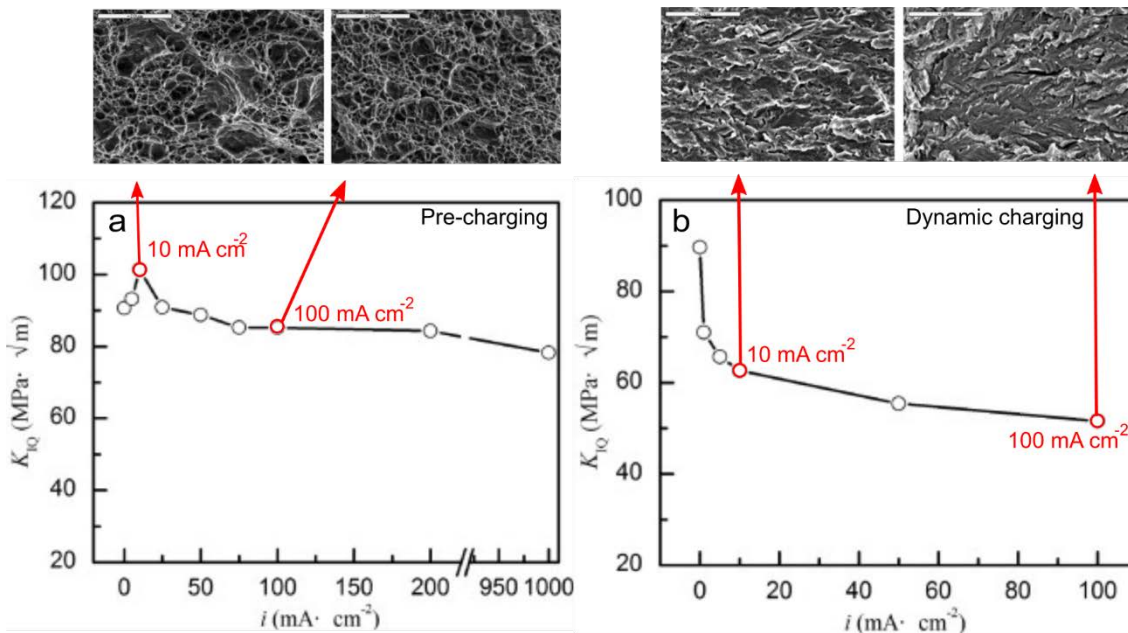


**Figure 37: Effect of current density on the fracture toughness for X70 pipeline steel under a) hydrogen pre-charging and b) dynamic hydrogen charging (in-situ charging). SEM fracture surface micrographs from tests at current densities of 10 and 100 mA/cm<sup>2</sup>, are indicated with the red arrows for each charging condition. Figure adopted from [116].**

#### 5.4 Fracture Toughness in Welds and HAZ

In pipelines, failures often originate from small crack defects. Defects incubators in pipelines are often located in the heat-affected zones and welds: generally, it is observed that a reduced plasticity in the presence of hydrogen highly correlates to the different microstructures. From the available literature, microstructure is one of the most important parameters to consider for the selection of a pipeline steel in service in a hydrogen environment.

The hydrogen effect on existing defects in pipeline of X52 and X70 welds, base- and HAZ metal have been investigated by Chatzidouros et al. [67] (2011), using in-situ electrolytic hydrogen charging with three different current densities. Based on the studies by Hardie et al. [115] and R. Wang [116] which indicate that pipeline steels exhibit degradation of mechanical properties at current density around 10 mA/cm<sup>2</sup>, Chatzidouros and co-workers performed electrolytic hydrogen charging at the current densities of 1, 5 and 10 mA/cm<sup>2</sup>. Three-point bending tests (following the ISO 12135 standard) were conducted on BM and HAZ from the longitudinal seam weld, that were cut out from previous in-service pipes. An illustration of the specimen, with a pre-machined notch are shown in Figure 38.

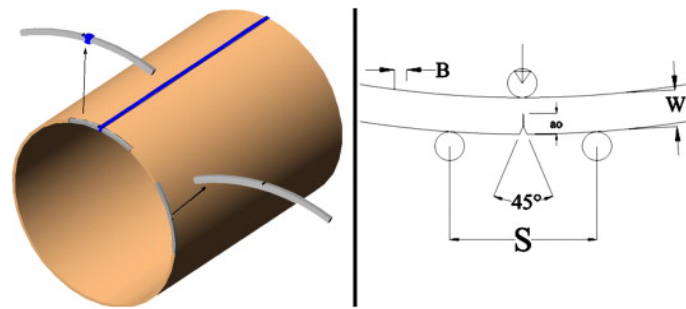


**Figure 38: Pipeline with location of test specimens, including test geometry [67].**

The reduction in toughness for the X70 base metal, expressed as the reduction of  $J_0$ , were substantially larger than that obtained in X70 HAZ. At 10 mA/cm<sup>2</sup>, the base metal exhibited a reduction of 64%, in contrast to 34.3 % reduction of  $J_0$  for the X70 HAZ, as reported in Figure 39 (a). The larger hydrogen-induced reduction of  $J_0$  in X70 base metal, were related to a synergistic effect of microstructural features and the presence of inclusions. The X70 base metal consisted of a banded ferritic and mixed bainitic-pearlitic microstructure with elongated grains, shown in Figure 40 (a-b). On the other hand, the X70 HAZ featured a banded structure, consisting of ferrite and a bainitic-pearlitic-ferritic microstructure, whereas the cementite content is lower than that seen in the bainite-pearlite bands in the base metal, illustrated in the high-magnification images in Figure 40. Continuous ferrite-cementite interphases along grain boundaries of banded microstructures and pearlite grains are shown to act as barriers to the hydrogen diffusion path [119-121]. Furthermore, the presence of MnS and Al<sub>2</sub>O<sub>3</sub> inclusions along bands were observed in the X70 BM. These can facilitate microcracks and hydrogen trapping along and between the bands of ferrite-mixed bainite-pearlite interface. Another feature influencing hydrogen trapping is the larger deformation gradient between the bands in X70 base metal than in X70 HAZ. For instance, microhardness measurements confirmed a difference of 85 HV and 61 HV between bands for X70 base -and HAZ metal, respectively.

The X52 base metal possess similar behaviour as the X70 base metal in terms of increased hydrogen susceptibility with increasing current density, with a 51% reduction of  $J_0$  for the current density 10 mA/cm<sup>2</sup>, shown in Figure 39 (b). Furthermore, X52 base metal exhibit greater relative reduction of ductility, than the X52 HAZ. Also, the authors relate the higher hydrogen susceptibility of the base metal to a synergistic effect; hydrogen diffusion in the banded structure and a larger deformation gradient between ferrite-pearlite bands in the X52 base metal, than in ferrite-pearlite grains in the X52 HAZ, Figure 41. Previous work has shown that a greater permeability occur in a randomly distributed ferrite-pearlite microstructure than in a microstructure consisting of pearlite bands perpendicular to the diffusion direction [119], indicating that pearlite bands can act as blockers for hydrogen diffusion and permeation depending on its alignment [121]. The continuous structure in the base metal forces the hydrogen trapping and the diffusion along the ferrite bands. Moreover, the large deformation gradient between the ferrite and pearlite bands results in a high hydrogen

saturation in the interfaces. The banded microstructure observed in base metal is less pronounced towards the HAZ and weld. The non-banded microstructure in HAZ possess a different behaviour due to a small deformation gradient between the ferrite and pearlite grains. Hence, the specimens exhibit higher resistance to hydrogen reduction of  $J_0$ , closer to *Zone I*, i.e. closer to the weld, illustrated in Figure 42.

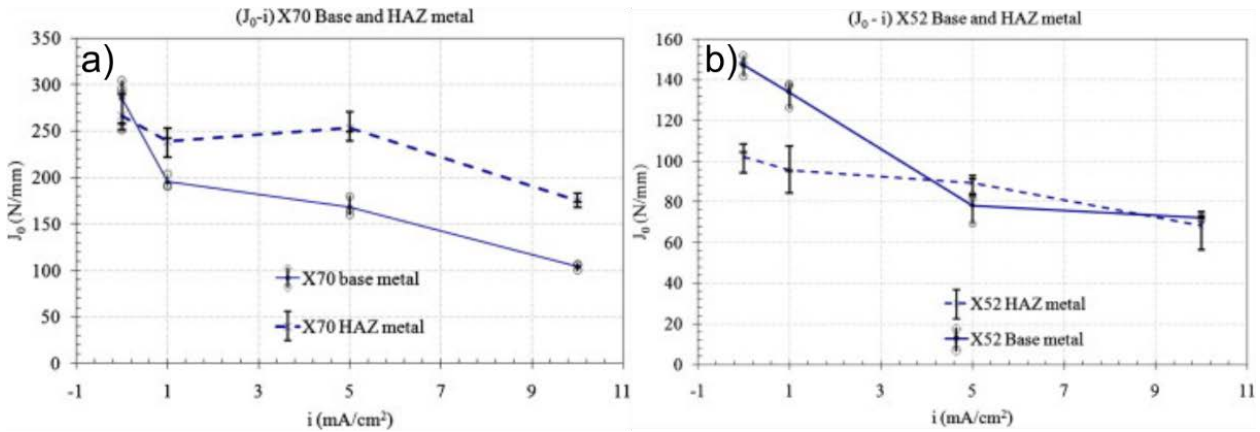


Figure 39: Change in Fracture toughness parameter,  $J_0$  with current density for a) X70 and b) X52 base -and HAZ metal [67].

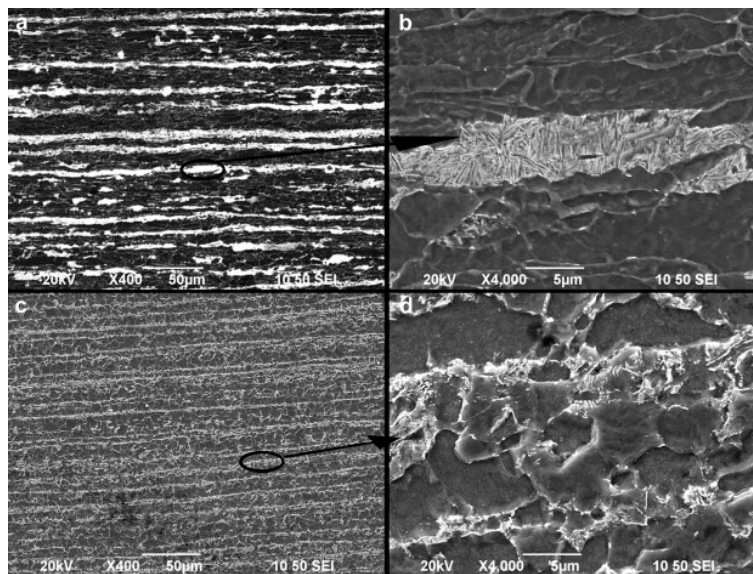


Figure 40: SEM micrographs of X70 a-b) base metal and c-d) HAZ at two magnifications [67].

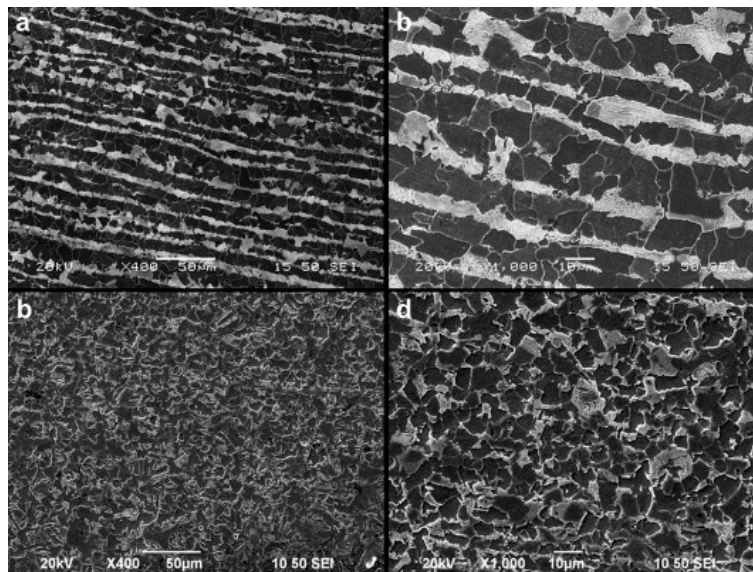


Figure 41: SEM micrographs of X52 a-b) base metal and c-d) HAZ at two magnifications [67].

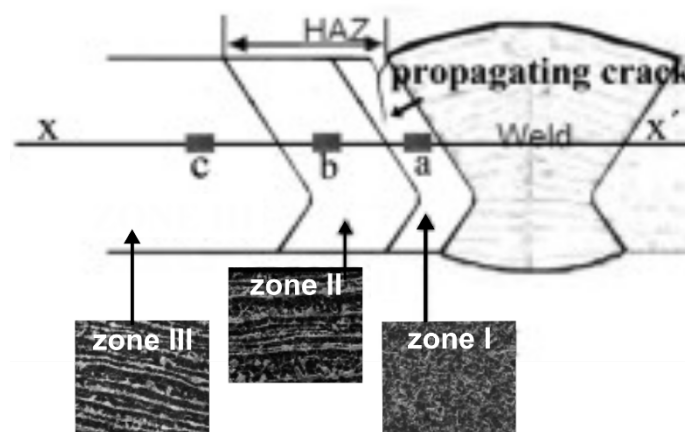
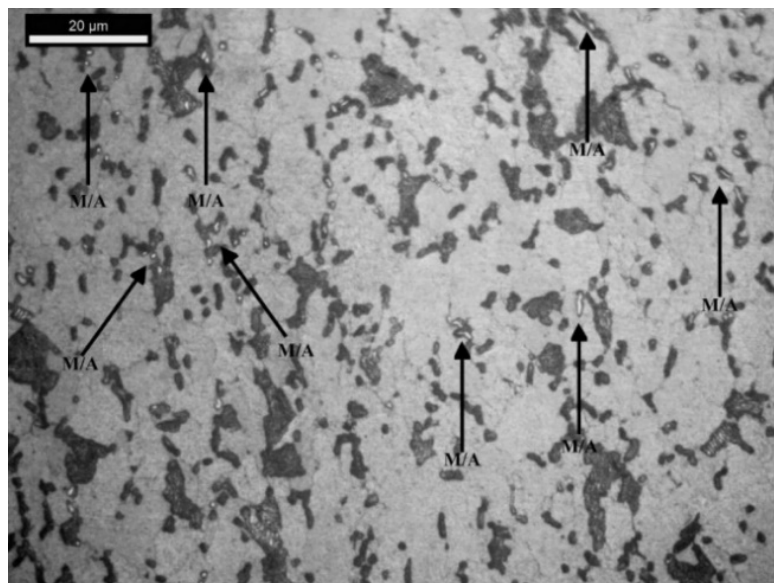


Figure 42: Microstructures in X52 pipeline steel in the different microstructural zones after welding. Figure adapted from [67].

In both the X52 and X70 base metal the microstructure is arranged in bands. Latest trends in pipeline steel manufacturing often possess microstructures with lower carbon content and ferritic-bainitic phases in a homogeneous appearance. Chatzidouros et al. [51] (2014) performed additional testing, following the similar experimental methodology, to a modern X65 pipeline steel base metal and compared the hydrogen effect on fracture toughness with results from the two other pipeline steels, X52 (ferrite-pearlitic) and X70 (ferritic-mixed pearlitic-bainitic) [67]. The X65 pipeline steel contains a ferritic-bainitic microstructure with the presence of martensite/austenite (M/A) stringers shown in Figure 43 (after a two-step etching procedure). The M/A constituents are shown to appear in the ferrite and bainite grain boundaries and in the pearlite islands. The X65 base metal exhibit a substantial drop in ductility already at 1 mA/cm<sup>2</sup>, with J<sub>0</sub> exhibiting a reduction of 77%. The high degree of ductility loss is also prominent in the fractography in terms of brittle rupture, compared

to the ductile fracture morphology observed from tests in air. Figure 44 compare the % reduction of  $J_0$ , for all the three steels, i.e. X70, X52 and the X65 pipeline steel. The results clearly indicate that hydrogen reduction of  $J$ , is greater for the X65 base metal, and lowest for X52 base metal.

The key characteristics that distinguishing these steels are the banded formation of the X52 and X70 steel and the uniform microstructure of X65 with M/A constituent and the bainite content. Moreover, X65 base metal exhibited a ductility drop that is substantially larger than the other two steels. The authors attribute the significant hydrogen damage to the presence of M/A constituent in addition to high dislocation density low carbon bainite. Literature reveal that M/A constituents are favourable trapping sites for hydrogen [15, 122]. Ferritic-bainitic microstructures have also been reported to act as hydrogen trapping sites due to the fairly high dislocation density [123]. These microstructure features are quite different from that in X70 and X52 where the failure mechanisms are dictated along the bands. Banded ferrite-mixed bainite-pearlite microstructure with the presence MnS and  $Al_2O_3$  inclusions along bands, are more exposed to hydrogen damage than the banded ferrite-pearlite microstructure in X52, which are in line with previous findings stating that bainite microstructures have higher hydrogen solubility than pearlitic microstructures [15].



**Figure 43: X65 microstructure after two step etching procedure, with the presence of M/A constituents marked with black arrows [51].**

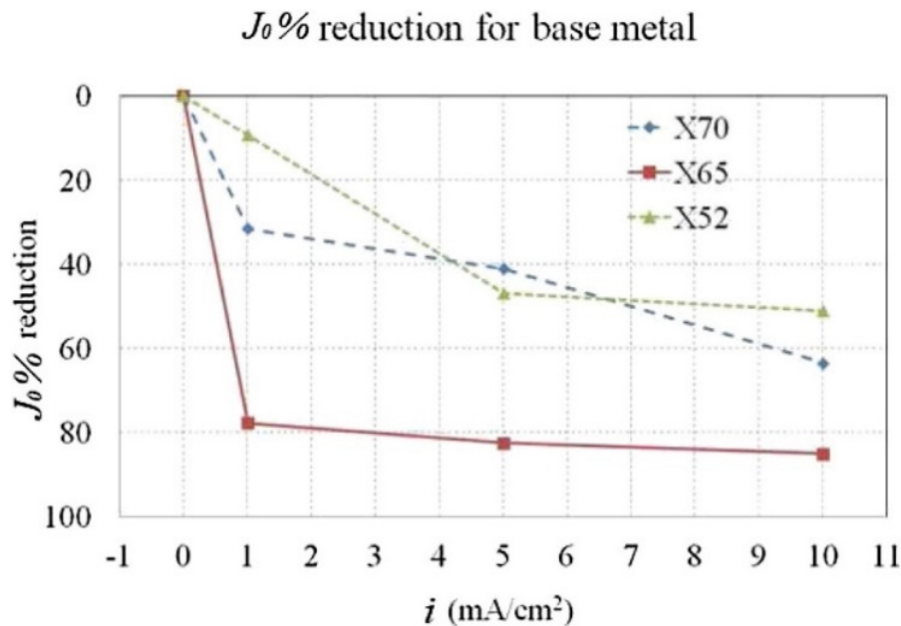


**Figure 44:**  $J_0$  integral reduction (%) for X70, X52 (data from [67]) and X65 [51].

The complex phenomena of stress and diffusion involved in the process of hydrogen embrittlement have been investigated at different dimensional scales in the literature. From a macroscale- point of view, the Cohesive Zone Models (CZM), are well accepted as numerical technique to predict the degradation in mechanical properties of steel in a hydrogen environment. Among the cohesive zone models, some of the main approaches to simulate hydrogen embrittlement includes the combination of stress, diffusion and cracking analysis in a sequential manner. This formulation was first proposed by Olden et al. [124] in 2008 for the estimation of hydrogen induced crack initiation in 25% duplex stainless steel. The similar method was later used to simulate the crack initiation of hydrogen-induced fracture in a X70 pipeline weldments [61]. The two-dimensional finite element approach was performed in combination with in-situ (SENT) fracture mechanical testing, simulating typical subsea operating conditions (potential of  $-1050\text{mV}_{\text{SCE}}$  and  $T=4^\circ\text{C}$ ), where the hydrogen influenced threshold stress intensity factor was established for the base metal, weld metal and heat-affected zone for the material. The results indicated minimal hydrogen susceptibility in base –and weld metal, which failed at net section stresses 24% above and nearly at the yield strength, respectively. While HAZ were highly exposed to hydrogen-induced damage and failed at stress levels 35% below its yield strength. Moreover, fracture topographies for HAZ exhibited a quasi-cleavage surface when exposed to hydrogen with secondary cracking outside the crack plane, commonly observed for hydrogen-induced fracture.

Fracture energies obtained for the base metal were consistent with that obtained in the aforementioned work by Chatzidouros et al. [67]. However, the fracture energies for the HAZ were higher in the results from Chatzidouros et al., attributed to the microstructural differences observed in the materials from the two studies; the former contained a mixture of banded ferrite, pearlite and



bainite. On the other side, the X70 HAZ microstructure from the work by Olden and co-workers, contain a bainitic-martensitic microstructure. The martensitic microstructure often appears after hyperbaric welding, hence its highly relevant to consider due to its poor properties in the presence of hydrogen. The high level of residual stresses and dislocations makes it an efficient trap site for hydrogen atoms, hence influence the diffusion rate and hydrogen concentration.

Findings from electrochemical permeation testing were consistent with the microstructural features in terms of a slower diffusion coefficient and a higher sub-surface concentration in HAZ (high content of bainite and martensite) than that obtained in the base –and weld metal. Diffusion values for the X70 base metal are slightly higher than previous findings from a X65 pipeline steel [125], presumed to occur as a result of a higher level of micro-alloying element in X70 steel. As a result of this process, the formation of precipitations is expected. Consequently, a higher amount of potential trapping sites is available in X70 and thereby will slow down the diffusion.

The finite cohesive element approach developed by Olden et al. [61], was further developed from a two-dimensional to a three-dimensional model by Alvaro et al. [126]. Using a three-dimensional approach, that resulted in higher opening stress values at the stress peak, plastic strain values at the crack tip and hydrogen lattice concentration. However, higher opening stresses were necessary at the onset of crack propagation for the 2D model. The following investigation introduced a different approach in defining the initial cohesive parameters, in order to provide a realistic description of the hydrogen accumulation at the crack tip and of the competition between hydrogen in lattice and in traps in the material degradation [127]. Additionally, the study considered HE related failure both in the case of hydrogen gas and electrochemical charging. The result shows that crack initiation occur at the hydrostatic stress peak for electrochemical hydrogen charging conditions. Whereas the crack initiation occurred at the crack tip under hydrogen gas conditions based on Sievert's law. Results from the simulation also clearly indicate that the hydrogen in lattice interstitials have the major impact in the material degradation.

Hydrogen transport to degradation sites consist of multiple steps that plays a fundamental role for the HE phenomenon. Alvaro et al. [128] (2014) indicated that, apart from the HE mechanisms (such as HELP or HEDE), hydrogen transport kinetics and diffusion mechanisms also determine the incubation period and the local critical hydrogen concentration build-up before fracture. They examined fracture toughness properties of the HAZ of X70 pipeline steel from testing of SENT specimens at the hydrogen gas pressures of 0.1, 0.6, 10 and 40 MPa at 20°C. Experiments was performed in combination with Finite Element (FE) stress-driven diffusion simulations and analytical calculations of hydrogen trapping sites to support findings and understanding of the HE susceptibility. The influence of various hydrogen pressure on the fracture toughness was investigated from both load increase until failure and constant load (up to the failure load from the initial test) until failure. The HAZ, consisting of a martensite-upper bainite microstructure exhibited a yield and ultimate tensile strength of 775 and 913 MPa, respectively.

From SENT testing under rising load conditions, a significant reduction in both load and CMOD and J at failure, occurred when hydrogen pressure increased from 0.1 to 0.6 MPa, shown in Figure 45. The sudden fall in fracture mechanical properties was also reflected in the fracture surface morphology. The transition in fracture morphology goes from a ductile surface consisting of dimples, to a quasi-cleavage morphology with secondary cracking, indicating a significant loss in ductility due to the hydrogen effect. Additionally, the J-values (following the DNV-RP-F108 standard, calculated from CMOD at the onset of unstable crack growth), decreased from 1230 to 74 N/mm. At pressures between 0.6 and 40 MPa, no further significant changes in the load and CMOD curve were observed. Generally, structural steels exposed to hydrogen exhibit degradation of fracture toughness properties with increasing hydrogen pressure, until reaching the lower bound toughness, which is envisaged to have incorporated the maximum effect of absorbed hydrogen [129]. Further increase in hydrogen pressure has minor effect at this stage. Similar trend was clearly seen in the J-values at failure. Additionally, the small variations in  $K_Q$  values for all pressure levels indicated minor hydrogen influence on the elastic regime, in agreement with findings from three-point bending test under different cathodic potentials by Chatzidouros et al. [67] (2011).

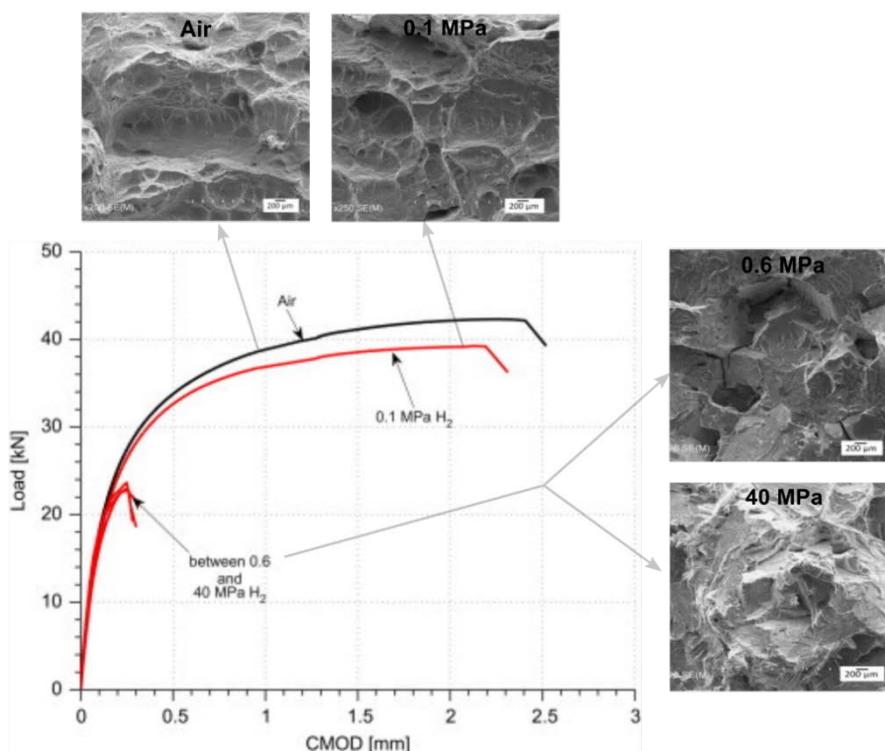


**Figure 45: Load vs. CMOD from SENT testing with load increase until failure at hydrogen gas pressures of 0.1, 0.6 and 40 MPa for a X70 pipeline weld simulated HAZ. The corresponding fracture surface morphology for each pressure are included and indicated with arrows. Figure adopted from [128].**

The SENT testing performed at constant load until failure, indicated that the additional time evolution of hydrogen diffusion mechanisms has a vital role in the determination of the detrimental

effect on fracture toughness properties, as shown in Figure 46. Furthermore, the material degradation was stronger at 40 MPa, related to the synergetic effect of stress and hydrogen concentration at the crack tip. The 3D FE modelling was reproducing the experiments performed at constant load to obtain the distribution of hydrogen lattice concentration as a function of the stress field at the crack tip, at different times, shown in Figure 46 for 40 MPa hydrogen pressure. The steady state distribution of lattice concentration was reached after 8 hours, which is consistent with the longest time to failure in the experiments (Figure 47 b). These results indicate that the lattice hydrogen concentration has a major role in the failure. This is despite a 10- and 100-times higher hydrogen concentration from traps, implying that the trapped hydrogen does not participate actively in the failure mechanisms and the high concentration is not sufficient for failure to occur.

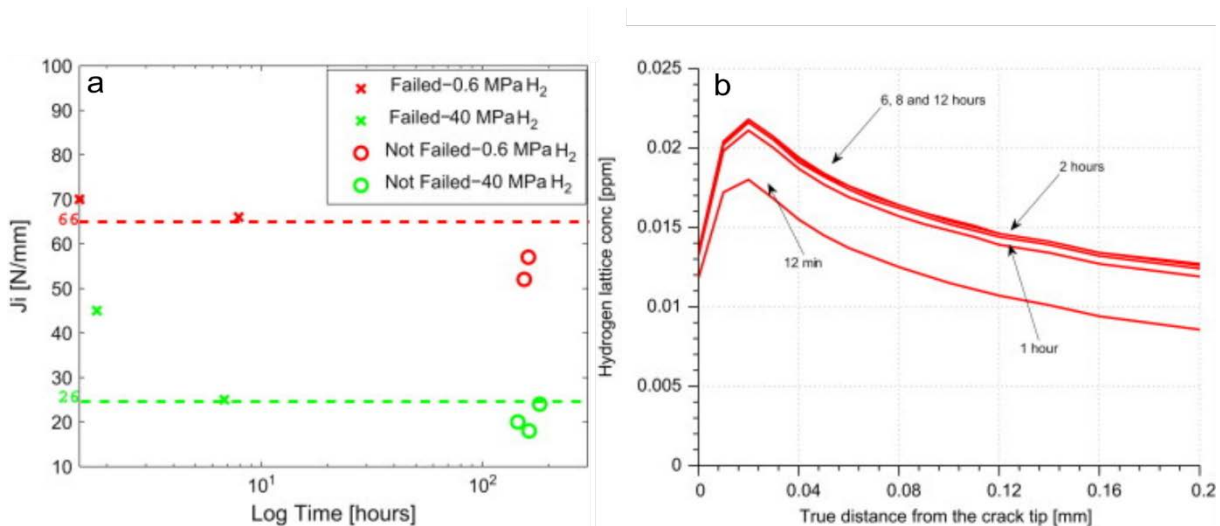


**Figure 46:  $J$  values at initiation of fracture from SENT constant loading testing and (b) time evolution of hydrogen concentration transients at the crack tip obtained from FE simulations using initial hydrogen-related boundary conditions defined by Sievert's law at 40 MPa [128].**

The aforementioned studies emphasize that the hydrogen effect in the base metal can be very different from that in the HAZ, due to the changes in metallurgy and mechanical properties. The coarse-grained HAZ (CGHAZ), located next to the weld fusion line, often exhibit lower fracture resistance due to the frequent presence of local brittle zones in a multi-pass welded joint [5]. Hydrogen effect in these microstructures are essential for reliability of a hydrogen gas transport infrastructure.

Ogawa et al. [130] (2017) investigated the similarities between hydrogen-assisted crack propagation of a low-carbon steel during cyclic and elasto-plastic fracture toughness ( $J_{IC}$ ) using compact-tension specimens in hydrogen environment at the pressures of 0.7 and 115 MPa. The fracture toughness properties were reduced in the presence of hydrogen, likewise, the  $J$ - $\Delta a$  curves degraded in the presence of hydrogen as shown in Figure 47. Particularly at high hydrogen pressure, i.e. 115 MPa,

the degradation was significant, in agreement with previous reported results on low alloy and carbon steels.

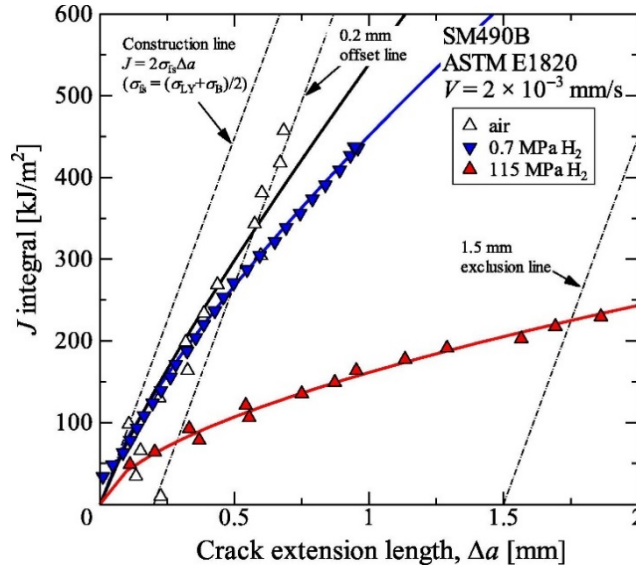


Figure 47: J- Δa curves obtained from elasto-plastic fracture toughness tests in air and hydrogen gas with pressures of 0.7 and 115 MPa [130].

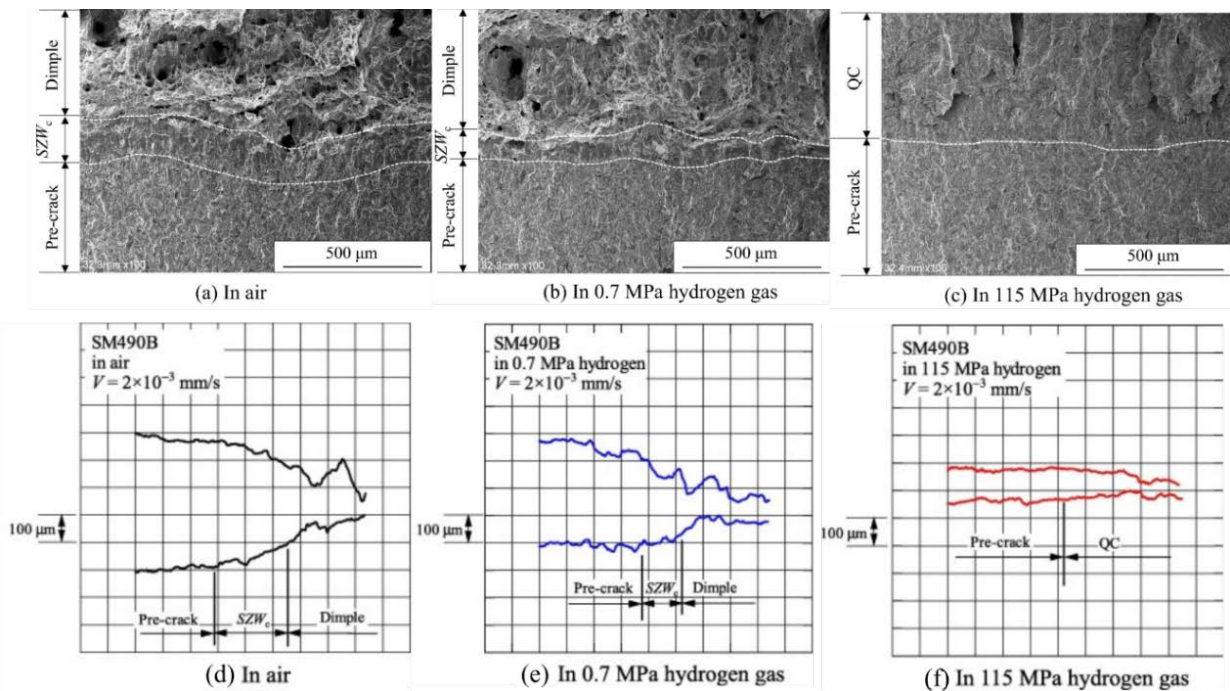


Figure 48: (a-c) SEM micrographs of fracture surfaces from  $J_{IC}$  tests of a low carbon steel obtained in air, 0.7 MPa and 115 MPa hydrogen gas, respectively. (d-f) Cross-sectional shape of the cracks formed in each environment reconstructed from stereo-pair SEM images.  $SZW_c$  indicate the critical stretch zone width formed in the front of the fatigue pre-crack. Figure adopted from [130].

As shown in Figure 48, the fracture morphology was highly dependent on the hydrogen pressure. While the tests performed in air and at 0.7 MPa hydrogen pressure presented an SZW zone and dimples, the specimen tested at 115 MPa did not show any SZW but surface with quasi cleavage features extending directly after the pre-crack, indicating less blunting. The cross-sectional shape of the cracks, obtained from stereo-pair analysis of fracture surfaces are shown in Figure 48(d-f), reveal evidence of large crack blunting from fractures surface obtained in air and at 0.7 MPa hydrogen gas. In contrast, the crack evolution in 115 MPa hydrogen gas was accompanied by substantial crack-tip sharpening and the formation of QC fracture surfaces. Crack growth properties at high hydrogen pressures were related to the HELP hypothesis and described according to the hydrogen-induced successive crack growth (HISCG) [131]. Moreover, it was stated that the intrinsic fracture mechanisms were basically identical in both loading conditions, i.e. fracture toughness testing and fatigue.

## 5.5 Effect of Orientation

Fracture toughness properties in pipeline steels are in general evaluated in the directions perpendicular to the rolling direction, either in the directions TL, LT or TS, LS, (the first letter designates the grain direction normal to the crack plane and the second letter designates the grain direction parallel to the fracture plane). While it is straightforward to extract fracture mechanical properties from these directions, it is challenging to evaluate fracture toughness properties in the SL (parallel to rolling plane) and ST directions as a result of restricted pipeline wall thickness following the ASTM E 1820 standard. It is simply not enough material to extract a full single edge bending (SEB) or compact tension (CT) specimen for evaluation of fracture toughness properties. Several investigations show that fracture toughness properties in thermomechanical control processed manufactured steels, can differ for the different directions [132, 133]. This has drawn some attention to the investigations of orientation dependence of fracture properties and crack growth in hydrogen related environments. Additionally, novel SEB geometries have been developed to overcome the pipe wall thickness constraints for fracture mechanical testing in the SL direction.

A recent study by Chatzidorou et al. (2018) [134] included fracture mechanical testing in both LT and SL direction (perpendicular and parallel to the pipe wall thickness), following ASTM E1820 on pre-charged X65 steel specimens, shown in Figure 49.

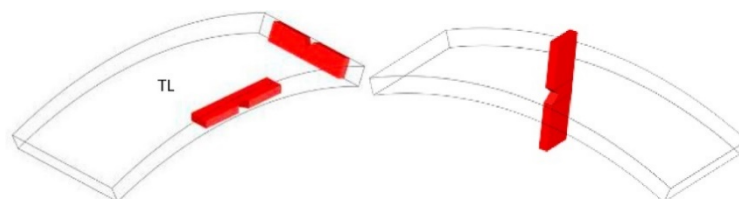


**Figure 49: Schematic illustration of SEB specimens with notch orientation in the TL direction (left image) and SL direction (right) [134].**

The X65 pipeline steel contained a microstructure with both ferrite and bainite phases, with grains elongated in the TL direction. Overall, the fracture toughness properties in the SL direction from tests in air are higher than that obtained in TL direction; a 3.9 % difference in the maximum stress intensity factor,  $K_Q$ , and a 20% difference in CTOD values. This is also evident for electrochemical charged specimens. With increasing hydrogen concentration (established using Thermal Desorption Spectroscopy), CTOD values with increasing hydrogen concentrations clearly decreased in both directions, particularly in the TL direction. On the other hand, the hydrogen concentration (up to 2ppmw) had no measurable effect on the maximum  $K$  for the crack plane in the TL direction, shown in Figure 49. In the SL direction,  $K$  exhibit a 14% reduction with increasing  $C_H$ . The higher susceptibility in the SL direction were attributed to the presence of elongated grains in the microstructure, which provide a favourable hydrogen diffusion path in the SL direction. For this reason, the SL direction is suggested to be considered in the assessment of life span of pipelines. The drop in CTOD on pre-charged specimens are consistent with previous work [116, 135, 136]. According to their previous investigation, a reduction of  $J$  integral was significant under hydrogen charging. According to the relation between CTOD and  $J$ :

$$J = m\sigma_y CTOD \quad (23)$$

where  $\sigma_y$  is the yield strength of the material, and  $m$  is a constant, the CTOD decreases with the reduction of  $J$ . The reduction of CTOD observed in the X65 pipeline steel was attributed by the authors to the dislocation dense bainite which facilitates hydrogen damage along the bainite structure. The authors emphasize that accurate knowledge of relevant material fracture toughness data is needed in order to perform reliable Engineering Critical Assessment (ECA). Usually, the fracture toughness parameter used for the assessment of remaining lifetime, is the critical stress intensity factor. However, the present results show that CTOD is greatly reduced in cases where maximum  $K$  remains nearly insensitive. Hence it was stated that CTOD measurements in SL direction is more suitable fracture toughness parameter for ECA assessments (in the presence of HIC damage).

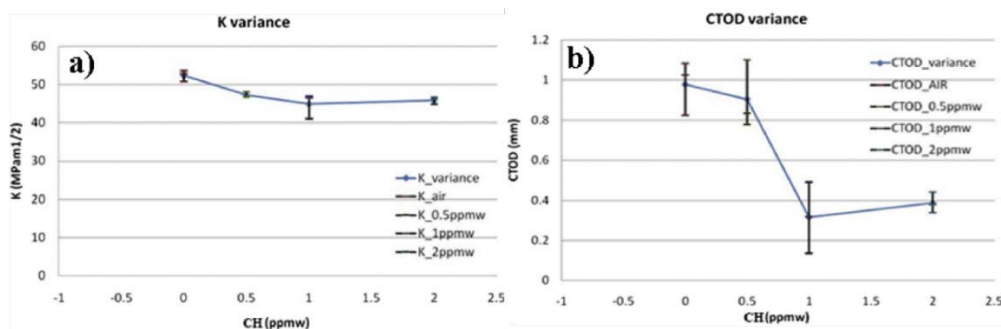


**Figure 50: Fracture toughness variation with increasing hydrogen concentration for the TL direction in X65 pre-charged specimens; a)  $K$  variation and b) CTOD variation [134].**

Following the similar methodology, Chatzidouros et al. (2019) [137] performed additional testing on a X42 alloy. Fracture mechanical testing ( $K_Q$  and CTOD) was performed (ex-situ) on a X42 pipeline steel under simulated  $H_2S$  conditions in both TL and SL directions: perpendicular and parallel to the pipeline wall thickness, respectively (ASTM E1820). From fracture toughness testing, it was revealed that  $K_Q$  was not affected in the SL direction, while it was reduced in the TL direction for a hydrogen concentration of 1.5 ppmw. On the other hand, CTOD was significantly reduced in the SL direction up to 1 ppmw CH.

The damage behaviour in this material is highly correlated to the microstructure of this material. There are two main characteristics in the X42 pipeline steel that reveal an influence: elongated non-metallic inclusions and lamellar structure of the pearlite phase. Inclusion produce voids as there is no bonding between inclusion and matrix. This easily promote early failure during mechanical tests, in particular for high level of CH.

## 5.6 Effect of Inhibitors

Recently, Komoda et al. (2019) [138] showed that the embrittling effect of hydrogen is reduced with increasing oxygen content. Fracture toughness tests of a carbon steel, A333 Gr. 6, was performed in hydrogen gases with an oxygen content of 100, 10 and 0.1 vppm. This pipeline steel consists of a ferrite-pearlite microstructure in a banded appearance. Testing was performed according to ASTM E 1820 standard [139], except for the loading rate which is represented by crosshead speed in this study. Three different speeds were used:  $2 \times 10^{-3}$  mm/s,  $2 \times 10^{-4}$  mm/s and  $2 \times 10^{-5}$  mm/s.

The ppm levels are crucial for testing and precisely controlled and the oxygen content was maintained at a constant level throughout the testing. The relationship between the J-integral and crack extension,  $\Delta a$  are shown in Figure 51. The J- $\Delta a$  curves obtained after testing with hydrogen + 0.1 vppm oxygen resulted in a lower position than results from tests in air, indicating that the hydrogen had sufficient of access to degrade the materials' fracture toughness. The data from the test in 10 vppm O<sub>2</sub> positioned between data in air and 0.1 vppm oxygen. Finally, data from tests in 100 vppm oxygen, converged with that obtained in air.

Interestingly, the initial part of the J- $\Delta a$  curve was investigated in detail to see the initial evolution of the crack propagation in 10 vppm. As shown in Figure 52 the data (10 vppm) converged with the data from tests in air, up to a crack length of 30  $\mu m$ . In contrast, tests in 0.1 vppm oxygen, had a clear deviation from that in air from the very first moment of testing.

The authors discuss and relate the behaviour in 10 vppm oxygen, to the competitive interaction of hydrogen and oxygen on the Fe surface. According to density functional theory (DFT) calculations performed by Stakov et al. [140], the reaction rate constant for hydrogen dissociation on an iron surface with the presence of oxygen, is significantly lower (nine orders of magnitude), compared to

hydrogen dissociation on a pristine iron surface. When hydrogen molecules approach a pristine iron surface, a particular activation energy is needed for the dissociation process. Oxygen on the other hand, dissociate without an activation barrier. Additionally, attractive forces between the iron surface (at a particular distance) and oxygen molecules are much higher, than for hydrogen molecules. As a result, the much faster dissociation rate of oxygen molecules on the iron surface, creates a larger activation barrier for hydrogen dissociation.

As seen in Figure 52, the inhibitor effect of 10 vppm of oxygen was suggested to be present at the initial stage where oxygen causes a passivation. When reaching a crack length of 30  $\mu\text{m}$  the inhibitor effect is suggested to diminish as the onset of the hydrogen-induced degradation occurs. This transition was determined by the competition between the rate at which the bare iron surface is created by crack growth and the rate at which it is passivated by oxygen. If the rate of new surface creation is lower than the rate of repassivation, oxygen can cover the bare iron surface that introduce an inhibitor effect. However, if the rate of surface creation is larger than the rate of repassivation, the inhibitor effect is reduced. At 100 vppm of oxygen prevented hydrogen absorption into the material and hydrogen embrittlement was inhibited.

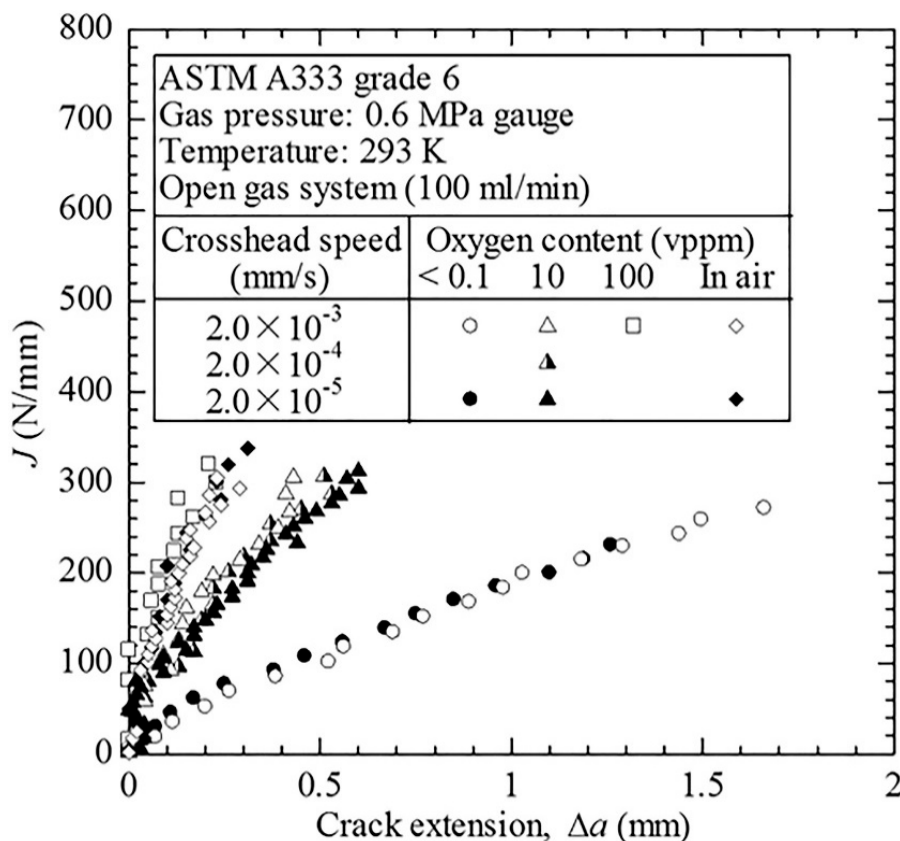


**Figure 51: J- $\Delta a$  curves from fracture toughness test in hydrogen with various oxygen content [138].**



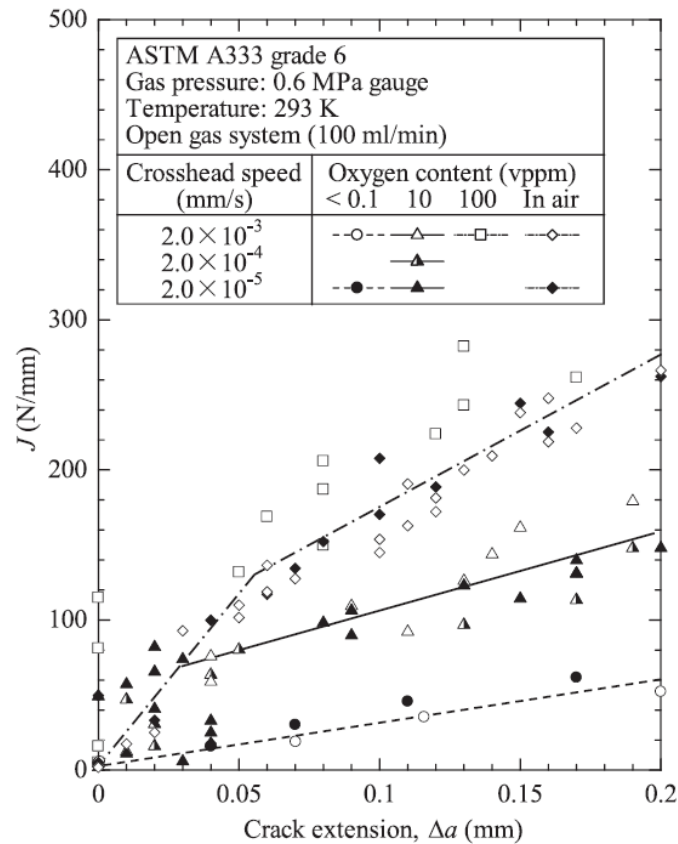


**Figure 52: J- $\Delta a$  curves at the initial part of the fracture toughness test [138]**

Experimental results from Charpy testing are not included in this review, as the test method doesn't allow for the time-dependent mechanisms during hydrogen uptake to take place which are of vital importance with respect to pipeline in-service conditions. Nevertheless, the following study are included as the microstructural aspects are of relevance for this literature review.

**Lee et al. [31] (2013)** systematically investigated the hydrogen effects on the impact toughness of simulated CGHAZ in a X70 pipeline steel, by using standard Charpy V-notch impact tests. The CGHAZ are in general divided into four subzones (a more detailed description can be found in section "Materials and Metallurgy"). Among these, the unaltered (UA) CGHAZ, the super-critically reheated (SCR) GCHAZ and the inter-critically reheated (IC) CGHAZ, were tested in hydrogen free and hydrogen charged condition at room temperature (RT) and  $-40^{\circ}\text{C}$ .

As shown in Figure 53 (a-b), there are large fluctuations in the impact toughness obtained for the various microstructures. The UA CGHAZ and IC CGHAZ exhibited a dramatic loss in toughness at both RT and  $-40^{\circ}\text{C}$ . On the other hand, the SCR GCHAZ exhibited an impact energy, even higher than that of the BM. This zone is often treated as fine-grained HAZ (FGHAZ) as a result of its recrystallized fine grains. Tests performed at  $-40^{\circ}\text{C}$  shows similar trend as seen at RT. However, the IC CGHAZ stand

out as the most brittle zone among those tested, with a noteworthy decrease in energy as temperature is decreased, with a toughness of  $\sim 8$  J in a H-free state and  $\sim 3$  J for H-charged state.

The higher brittleness of the UA CGHAZ and IC CGHAZ was attributed to the coarse microstructure consisting of high dislocation density bainite and the presence of martensite-austenite (M-A) constituents. As shown in the SEM images in Figure 54, a significant amount of M-A constituents are present in both zones, also verified by the high carbon content shown in the colour map from electron probe microanalysis (EPMA) in Figure 54 (c). The IC CGHAZ zone contained twice as much M-A constituent than the UA CGHAZ with 18% compared to 9%, respectively. The hydrogen-induced drop in toughness in SCR CGHAZ was attributed to its fine-grained microstructure, introducing a large fraction of grain boundaries acting as traps for hydrogen. Interestingly, macro images of the fracture surface reveal relatively large cracks, so-called splitting, for the UA and IC CGHAZ. This observation was only seen in the hydrogen charged samples, thus the author closely relates this to the hydrogen-induced loss in toughness. The main mechanisms responsible for this event is not completely understood in detail, but it is speculated that hydrogen atoms trapped in sites, such as lath boundaries can easily initiate cracks that introduce the splitting.

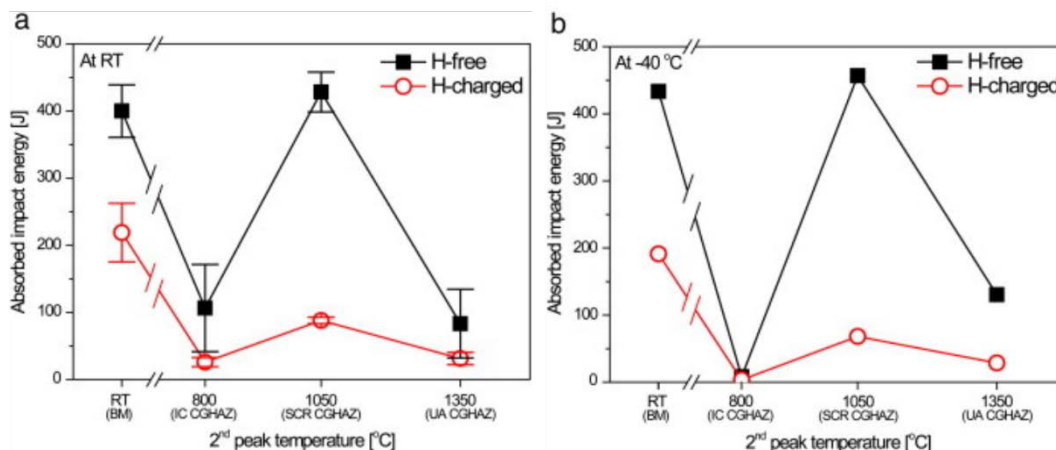


Figure 53: Charpy energy of simulated HAZ's at (a) room temperature (RT) and (b)  $-40^{\circ}\text{C}$  [31].

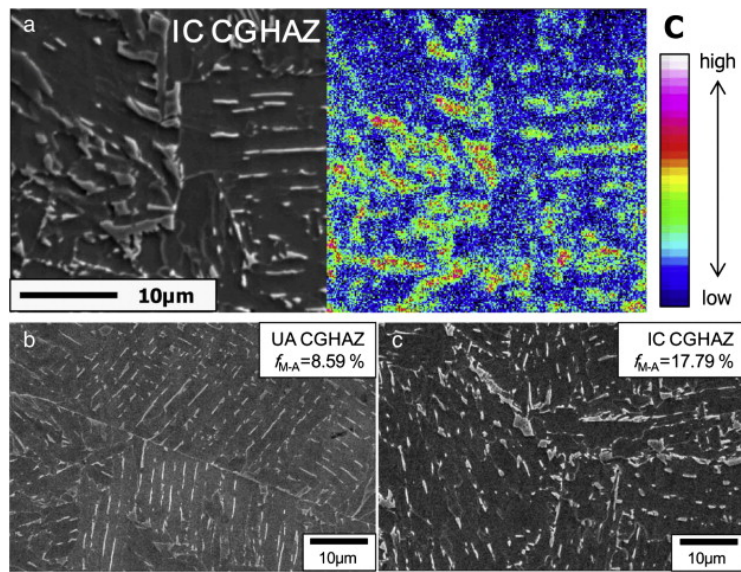


Figure 54: SEM microscopy showing the M-A constituents remaining after the two-stage etching. Also verified in from the very high carbon content in the map of electron probe micro-analysis (EPMA).

**Table 5: Fracture toughness for low-carbon steels in hydrogen gas and room temperature. Fracture toughness values from air are included for comparison.**

Steel	$\sigma_y$ † [MPa]	RA † [%]	Test environment	Displ. Rate mm/s	$K_{IC}$	$K_{IH}$ ‡	DJ/d a MPa	Ref.
<b>A516-70</b>	375	69	Air	$8.5 \times 10^{-3}$	166*		516	[79, 108]
			3.5 MPa H <sub>2</sub>			131	47	
			6.9 MPa H <sub>2</sub>			113	55	
			20.7 MPa H <sub>2</sub>			98	54	
			34.5 MPa H <sub>2</sub>			90	57	
<b>X42</b>	366	56	6.9 MPa N <sub>2</sub>	$2.5 \times 10^{-4}$	178*	107	63	[80, 81, 141]
			6.9 MPa H <sub>2</sub>	$2.5 \times 10^{-3}$				
<b>X42</b>	280	58	Air	$3.3 \times 10^{-4}$	147*		111	[110]
			2.0 MPa H <sub>2</sub>			101-128	-	
			4.0 MPa H <sub>2</sub>			85	36	
			6.5 MPa H <sub>2</sub>			69	31	
			7.0 MPa H <sub>2</sub>			73#	-	
			8.0 MPa H <sub>2</sub>			59#	-	
			10 MPa H <sub>2</sub>			53#	-	
			12.2 MPa H <sub>2</sub>			57#	-	
			16 MPa H <sub>2</sub>			46#	-	
<b>X60</b>	473	62	6.9 MPa He	$8.5 \times 10^{-3}$	142	104	123	[79]
			6.9 MPa H <sub>2</sub>				43	
<b>X70</b>	584	57	6.9 MPa N <sub>2</sub>	$2.5 \times 10^{-4}$	197	95	251	[81]
			6.9 MPa H <sub>2</sub>	$2.5 \times 10^{-3}$			23	

<b>X60</b>	434	88	5.5 MPa H <sub>2</sub>	2.5x10 <sup>-4</sup>	-	85	[113]
			21 MPa H <sub>2</sub>	2.5x10 <sup>-3</sup>		82	

\* May not be valid plane strain measurements

# Measured from burst tests on pipes with machined flaws

‡ Yield strength and RA of smooth tensile specimen in air

‡ Calculated from relationship  $K=\sqrt{JE}/1-\nu^2$

## 6 Fatigue Performance

Fatigue crack growth rate (FCGR) is one of the essential properties to consider in safe design of pipeline steels. In general, fatigue crack growth in metallic materials is described by means of  $da/dN$  (the per-cycle variation of the crack length) vs  $\Delta K$  (stress intensity range) plot. Although  $\Delta K$  is the primary variable the FCGR also depends on other factors such as the maximum stress intensity ( $K_{max}$ ), the stress ratio ( $R = K_{min}/K_{max}$ ), the cyclic frequency, the wave form and the environment. The crack growth curve for most metallic materials display three different zones which are related to different stages of the crack propagation, schematically illustrated in Figure 59. Stage I represents crack growth at low  $\Delta K$  and  $da/dN$  in which the fatigue crack appears to be dormant below the fatigue threshold  $\Delta K_{th}$ . The crack tip extension between cycles is in the order of several ångströms and the crack length is typically smaller than 500  $\mu m$ . Microstructural features, e.g. interfaces, can contribute to a prolonged stage I period. In stage II, or the *Paris domain*, the plastic zone encompasses multiple grains, resulting in less microstructure-dependency and thus a possibility of applying a continuum approach of the crack driving force in terms of  $\Delta K$ . In this intermediate region (usually between  $10^{-9} - 10^{-6}$  mm/cycle) the crack growth presents a power-law behaviour that is usually described by the Paris Equation [142]:

$$da/dN = A(\Delta K)^m \quad (24)$$

where  $A$  and  $m$  are material constants. In absence of hydrogen, Stage II tends to present transgranular crack growth for the materials of interest in this review, i.e. pipeline ferritic steels. [143]. Finally, *Stage III* of accelerated crack growth is reached when  $K_{max}$  approaches the critical stress intensity,  $K_{IC}$  for the material (for plane strain condition).

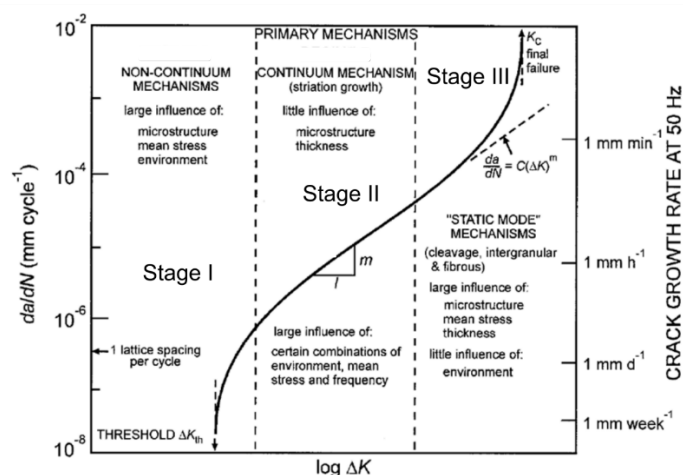


**Figure 55: Schematic illustration of typical variation in fatigue crack growth rates  $da/dN$  showing the different stages or regimes in function of the applied stress intensity range  $\Delta K$  in metallic materials [144].**

## 6.1 Fatigue Life

In the infinite life design of components, the maximum stress applied to a component is set below the fatigue limit of the material. When evaluating the integrity of materials in hydrogen environment, the fatigue limit is one of the most important properties to be considered. In general, low and medium strength steels have definite fatigue limits determined by one of two threshold conditions, i.e. "the crack initiation threshold" or "the crack growth threshold" of small fatigue cracks. Most studies on hydrogen effects focus on the intermediate stress intensity regime for "large" cracks, i.e. where continuum-based fracture mechanics definitions are valid. However, there is still a lack of understanding of the fatigue limit under the presence of hydrogen, particularly for low -to medium strength steels.

A recent study by Ogawa et al. [145] is the first study that addresses the fatigue threshold of small cracks in steel exposed to high hydrogen gas pressures (>100 MPa). They investigated the fatigue limit of a low carbon steel (JIS-SM490B) by performing fully reversed tension-compression tests on smooth specimens in laboratory air and in situ in 115-MPa hydrogen gas applying a frequency of 1 Hz. The S-N data in Figure 55, shows that the fatigue life in hydrogen gas is lowered in the shorter life regime,  $N_f < 10^5$ . The total fatigue life regime consists of the initiation life and the propagation life. The authors point out the complexity of the crack initiation process which is a result of factors that both enhance and delay crack initiation. In general, fatigue crack initiation from a smooth specimen surface involves irreversible dislocation gliding, persistent slip bands (PSB's) formation and subsequent initiation of surface intrusions and extrusions [146]. The hydrogen-enhanced localized plasticity mechanism (HELP) [34], is well known to localize slip bands and this can accelerate the formation of PSB's [146]. It has previously been reported that, in a ferritic-pearlitic carbon steel, crack initiation tends to primarily occur inside the ferrite grains, due to the hydrogen slip localization in narrow zones [147]. Low contents (ppm levels) of oxygen or water vapor in hydrogen gas can possibly reduce the rate of crack embryos formation and thus delay the fatigue crack initiation [148].

A previous study by Ogawa et al. [130], confirmed that fracture surfaces of the low carbon steel (JIS-SM490B) after fatigue tests in hydrogen gas, were of quasi-cleavage type known as an evidence of hydrogen-induced crack acceleration. Hence, the reduction of fatigue life in the present study [145], was attributed to the hydrogen-induced acceleration of crack propagation process and, that the hydrogen influence on the crack initiation was insignificant. Therefore, in the longer life regime, the hydrogen influence was reported to be minimal, as the maximum stress amplitude at which the specimen did not fail in hydrogen, was similar to the fatigue limit in air, i.e.  $N=2 \times 10^6$ .

Optical microscopy of parallels from the crack initiation threshold -and crack growth threshold condition, revealed small fatigue cracks at the surface of the unbroken specimens at N of  $10^7$ . Additional test at N of  $2 \times 10^5$ ,  $1 \times 10^6$  and  $2 \times 10^6$  was performed for a more detailed investigation

of the crack growth and arresting behaviour. Surface cracks of various length were observed, and the top ten largest cracks were registered for each  $N$ , presented in Figure 56. According to these results, the authors suggest that the fatigue limit in air and at 115 MPa hydrogen gas is determined by a non-propagating condition of fatigue cracks at a stress amplitude of 260 MPa. At this stress level cracks initiated at a small number of cycles ( $N < 2 \times 10^5$ ), propagated slowly, and eventually reached a non-propagation condition before  $N$  of  $1 \times 10^6$ .

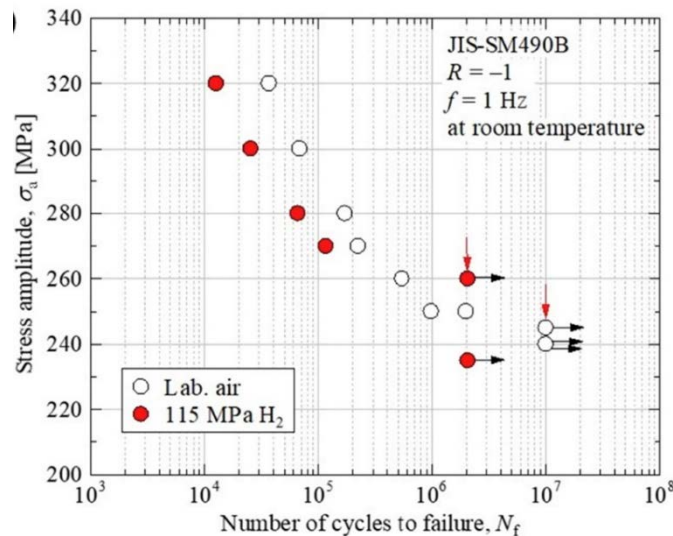


Figure 56: S-N diagram of a low carbon steel (JIS-490B) in air and in 115 MPa hydrogen gas. black arrows indicate the run-out of the test and red arrows pointing downwards mark the specimens examined in optical microscopy [145].

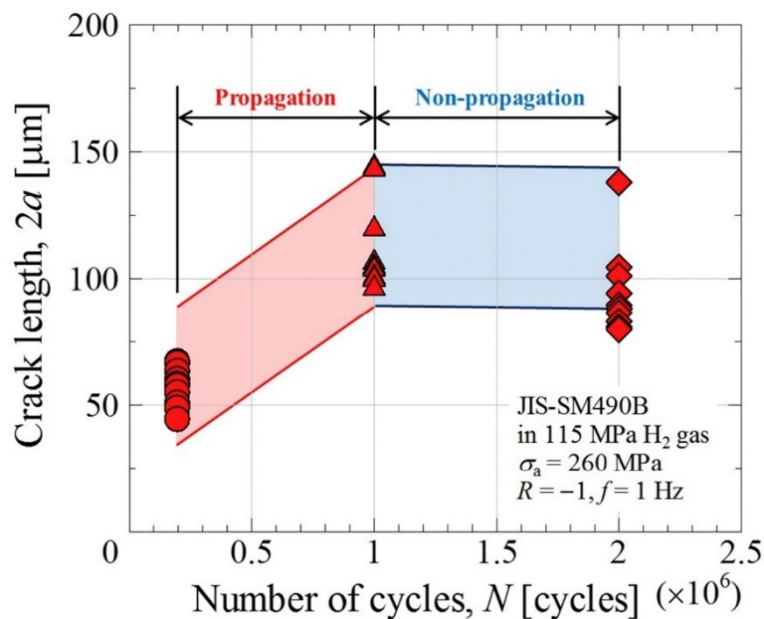


Figure 57: Relationship between fatigue loading cycles and length of the top ten largest cracks, from an unbroken specimen tested in 115 MPa hydrogen gas at  $\sigma_a = 260$  MPa [145].



## 6.2 Short Cracks

Characterization of fatigue crack growth in terms of fracture mechanics primarily relies on fatigue tests for long cracks typically several millimetres in length. However, investigations at very low fatigue crack growth rates, near the so-called threshold stress intensity range  $\Delta K_0$ , below at which the crack growth rate are experimentally undetectable, are limited. Crack sizes less than a millimetre (or comparable to the size of microstructure) cannot be analysed by linear elastic methods due to large scale plasticity effects and breakdown in the stress intensity factor correlation of fatigue crack growth rates. Consequently, this remains almost a completely uncharted research territory. The few relevant studies that exist on this topic to a large extent overlap with the Stage I fatigue crack propagation curve, which is the topic of the next section.

Suresh and Richie [149] investigated the near-threshold crack propagation in various steels under gaseous hydrogen environment at different load ratios. Their study showed that the threshold stress intensity in hydrogen are lower than in air at lower load ratio ( $R=0.05$ ) as a result of the absence of oxide-induced crack closure. In contrast, the thresholds were almost consistent in air and hydrogen environment at a higher stress ratio ( $R=0.75$ ), shown in Figure 57. Similar behaviour was observed for ferritic and bainitic steels as well. The results indicate that there are no degrading effects of hydrogen on the propagation threshold of small fatigue cracks.

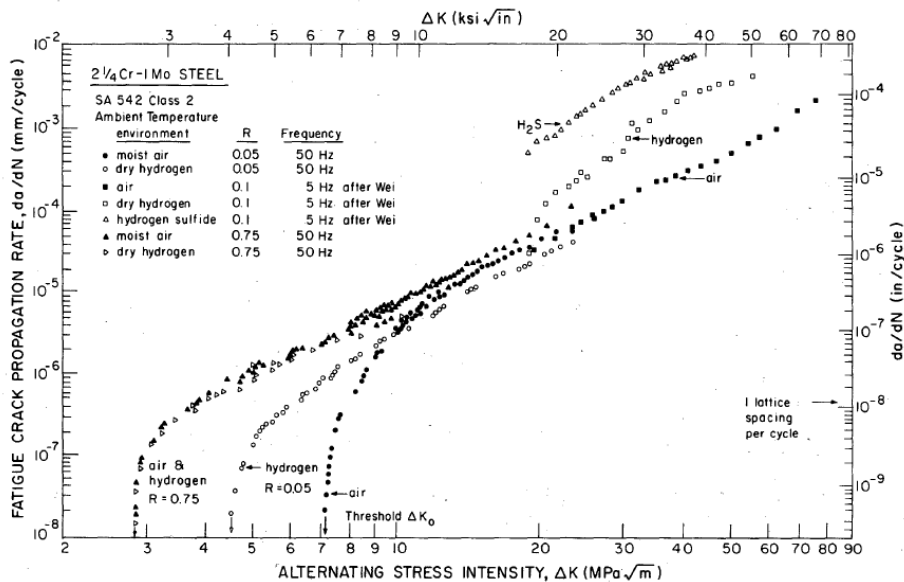


**Figure 58: Fatigue crack propagation in martensitic CrMo steel at  $R=0.05-0.75$  showing a reduced threshold stress intensity at higher load ratios. Similar behaviour [149].**

In agreement with Suresh and Richie, Sarrazin-Baudoux et al. [150] concluded that the hydrogen gas itself, had no particular effect in the near-threshold domain. They investigated the influence of hydrogen environment on fatigue crack propagation behaviour for both short and long cracks in a 3.5NiCrMoV steel (low martensitic alloy with bainitic microstructure with prior austenitic size of 50

μm) under 0.4 MPa hydrogen atmosphere, ambient air and high vacuum. Crack propagation tests were performed under load control at 20 Hz and R=0.1. artificial 2D short crack was obtained from machining the crack wake of the pre-grown long crack by using electro discharge machining (EDM). The influence of the difference environments on the near-threshold fatigue crack propagation for short and long cracks are shown in Figure 58.

The near-threshold propagation for small cracks in air and hydrogen are comparable Figure 58(a). Figure 58(b) shows the crack growth rates after closure correction, i.e.  $\Delta K_{eff}$ . shows that the effective crack propagation vs  $\Delta K_{eff}$  in both air and hydrogen are comparable to the similar effective threshold,  $\Delta K_{eff,th}=2.7 \text{ MPa}\cdot\text{m}^{1/2}$ . The results show that short crack growth is faster than the long crack growth and the threshold appears to be lower. The near-threshold fracture surfaces revealed a flat trans-crystalline surface with marking of the bainitic microstructure with traces of the previous austenitic grain boundaries and some localized brittle cleavage facets. The presence of these facets are suggested to gradually decrease with decreasing  $\Delta K$  [151] (no access). As Sarrazin observed, close to the threshold, fracture surface was in general very flat and of trans-crystalline character. No further considerations regarding the operating mechanisms was discussed.

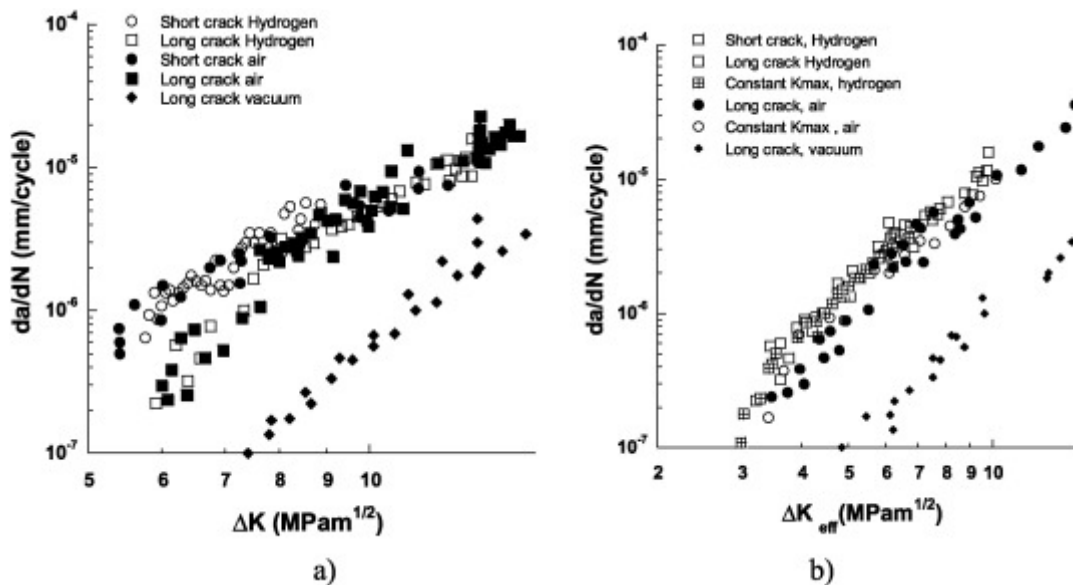
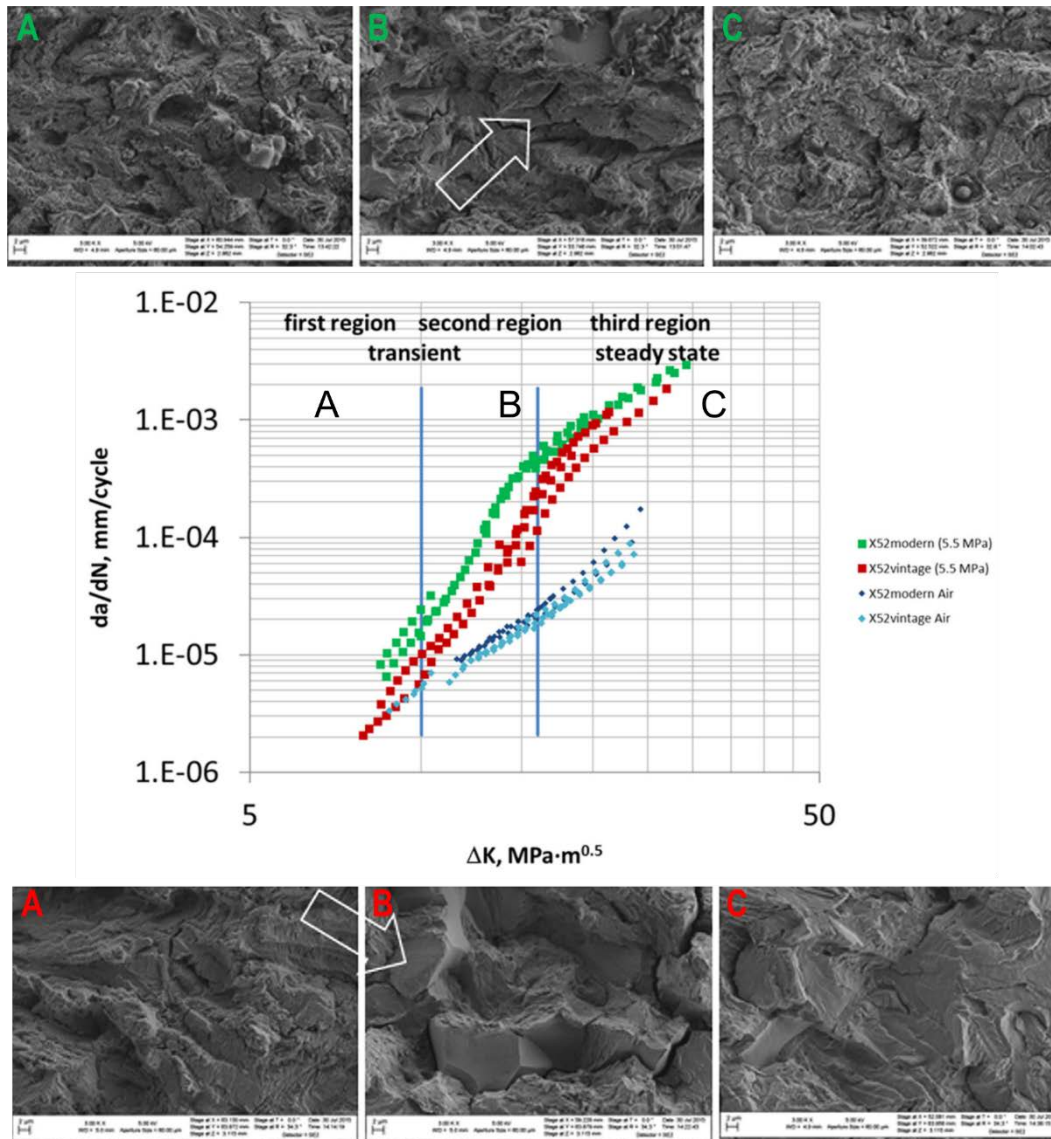


Figure 59: Fatigue crack growth rates for tests in air, vacuum and 0.4 MPa hydrogen gas at R=0.1 and 20 Hz a) da/dN vs.  $\Delta K$ ; b) da/dN vs  $\Delta K_{eff}$  after closure correction [150].

### 6.3 Hydrogen Assisted Fatigue Crack Growth

It is well known that the presence of hydrogen gas can accelerate the FCGR. Thus, in order to precisely estimate the fatigue lifetime of pipelines for transporting hydrogen gas, it is crucial to investigate how the hydrogen-induced acceleration is influenced by factors such as pressure,

loading frequency, loading ratio etc. and to understand the underlying acceleration mechanisms. In general, three distinct regions can often be observed when comparing the Paris domain of the FCGR curves obtained in hydrogen gas environment with the curves for the same material tested in air or inert environment, as exemplified in the curve plot in Figure 60.



**Figure 60: Fatigue crack growth curve for X52 modern -and vintage pipeline steel with corresponding fatigue fracture surfaces, above and below the graph, respectively (Frequency= 1 Hz and R=0.5). Figure adopted from [40, 152].**

A brief description of typical observations from these regions are given below and correlates with data presented in Figure 60 . The fracture surfaces differ significantly for each region, indicating that different deformation mechanism is dominating. It should be noted that the extent of the three

regions are strongly affected by parameters as the gas pressure and loading frequency as shown in Figure 61.

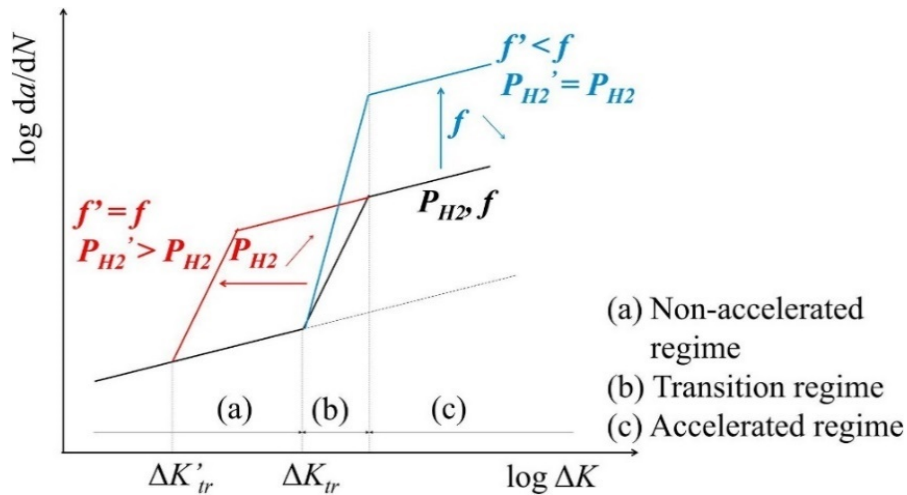


**Figure 61: Schematic curve of the effect of hydrogen gas pressure and loading frequency [153].**

**Region A:** Often the data obtained in air converge with those obtained in hydrogen in this region with very low  $\Delta K$ -values ( $\Delta K > 10 \text{ MPa}\sqrt{\text{m}}$  for this test). The corrosion effect of hydrogen is not significant in this region. According to Suresh and Ritchie, for a given set of testing parameters and hydrogen charging conditions, there is a threshold stress intensity value, below which the FCGR of steels are not affected by hydrogen [149]. The data within region A, are believed to be below this threshold value.

**Region B:** In this region a sharp increase in FCGR is recorded featuring a change in both Paris constants. The increase in FCGR has been attributed to an increase in hydrogen diffusion towards the crack tip due to a higher driving force from stress. It has been presumed that the crack extension per cycle is less than or equal to the size of the hydrogen-affected region ahead of the crack tip, i.e. the size of the fatigue process zone [40].

**Region C:** In the third region, above the "knee", it is often observed a slope comparable to that observed in the reference tests in air. This regime is often referred to as the "steady-state"-region and the Paris constants obtained in this region are often used as most conservative FCGR characteristic since the effect of hydrogen is assumed to be at a maximum and no further acceleration is to be expected. The region is dominated by the increase in  $\Delta K$  [40].

The American Society of Mechanical Engineers (ASME) B31.12 code for piping in both gaseous and liquid hydrogen service is based on data resulting from a large amount of tensile tests, showing a general trend of increased sensitivity to hydrogen embrittlement with increasing strength of pipeline steel [81, 154]. Based on the monotonic data, design thickness penalties were incorporated for all steels with a specified minimum yield strength (SMYS) greater than 360 MPa (grade X52). However, recent work at the National Institute of Standards and Technology (NIST) and Sandia

National Laboratories shows that material strength is not unambiguously correlated to hydrogen-assisted fatigue crack growth and suggest that the design criteria for higher strength steel may be too conservative [155]. Pipelines operate within a safety margin well below its yield strength (globally) and most of its loss in ductility is registered just after UTS is achieved. On the other hand, when considering these steels for transporting hydrogen gas, the material behaviour under cyclic loading conditions is often considered to be more relevant and important for evaluating its in-service condition for determination of lifetime and safety design. Therefore, there has been expressed a need to modify the ASME B31.12 code based on fatigue data.

Most of the relevant baseline findings are from the work by Holbrook, Cialone and co-workers [81, 141, 156]. They investigated the correlation between hydrogen embrittlement and FCGR with the effect of frequency, pressure, stress ratio, alloy microstructure and strength. Most results are for X42 steel, but additional results from a plain carbon steel (AISI 1080), pure iron and X70 steel are also investigated.

There has been a gap in research on hydrogen-assisted fatigue crack growth in pipelines from the mid 1980's until today. Recently, extensive work has been conducted at the National Institute of Standards and Technology (NIST) [40, 157] and Sandia National Laboratories with the purpose to propose a modification of the ASME B31.12 standard with respect to expanding the choice of steel grades used in the design of hydrogen pipelines. Based on these results, phenomenological models have been developed, correlating loading conditions, geometry and hydrogen pressure to the HA-FCG behaviour in pipeline steels [152, 158]. The effort of this work led to a code change that removed the design penalties on pipeline steels with a SMYS above 360 MPa (X52) and up to 480 MPa (X70).

The following section reviews additional existing literature on gaseous and electrochemically generated hydrogen effects on FCGR in low carbon pipeline steels. Key relationship between hydrogen embrittlement, FCGR and other variables, including frequency, pressure, stress ratio, microstructure and strength will be addressed. The literature relevant to ferritic pipeline steels provides a clear evidence of high susceptibility to hydrogen-assisted fatigue crack growth/enhanced fatigue crack growth rates when exposed to hydrogen [82, 113, 114, 149, 152, 159-162].

### 6.3.1 Effect of Hydrogen Gas Pressure

Hydrogen gas pressure is one of the most influential factors on the magnitude of FCGR acceleration in pipeline steels. Holbrook et al. [156] studied the effect of hydrogen gas pressure on FGC in a X42 pipeline steel at hydrogen partial pressures of 0 (1000 psi nitrogen), 30, 250 and 1000 psi and constant  $\Delta K$  of 20 MPa $\sqrt{m}$ , a cyclic frequency of 0.1 Hz and a load ratio of 0.25. The FCGR showed a clear dependence on the hydrogen pressure, whereas the ratio of FCGR in hydrogen to that in

nitrogen increased as a power function (with an exponent of 0.36) of the hydrogen partial pressure. Based on the results, the following relation was proposed:

$$\frac{(da/dN)_{in\ H_2}}{(da/dN)_{in\ N_2}} = 1 + 2.2P_{H_2}^{0.36} \quad (25)$$

where  $P_{H_2}$  is absolute hydrogen pressure in psi. The trend inferred by equation is graphically shown in Figure 62 where the acceleration factor, intended as  $(da/dN)_{in\ H_2}/(da/dN)_{in\ N_2}$  versus hydrogen partial pressure (converted to bar) is presented [163]. The relation gives an indication of the acceleration of FCGR occurring with increasing pressure. It was notified that the slope was much less steep than that obtained during monotonic loading (an exponent of 0.5). The hydrogen pressure dependence on hydrogen degradation for monotonic loading, typically follows a square root relation, given by Sieverts law [9], stating that the surface concentration should be proportional to the square root of the gas pressure, under equilibrium conditions. Holbrook and co-workers presumed that the relatively smaller square root dependence obtained from their dynamic loading tests, was due to a non-equilibrium state at the cyclically deformed crack tip. It should be notified that this relation is based on a limited number of tests, thus only gives an indication of the influence of hydrogen gas pressure on the fatigue crack growth behaviour in pipeline steels. On the other hand, the low frequency ensures that a high hydrogen concentration and thus time dependent degrading mechanisms are active in the process zone during the test.

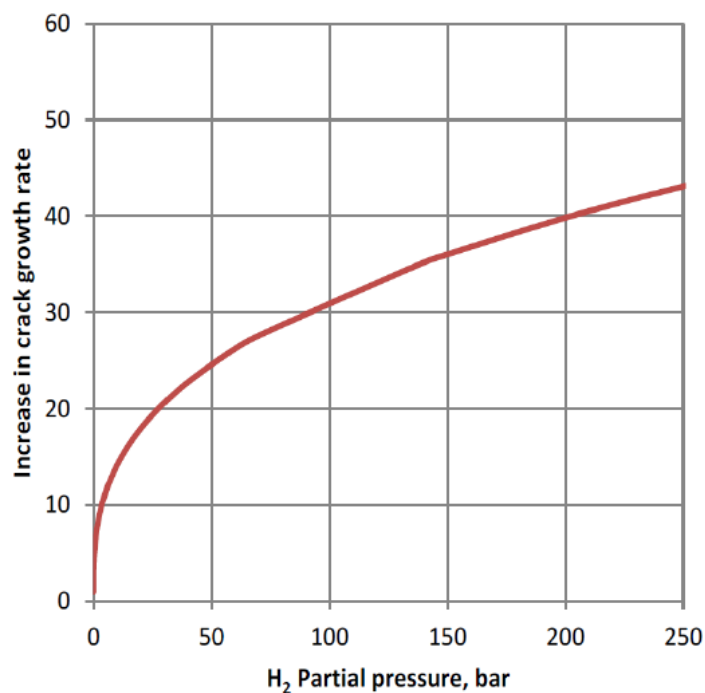


**Figure 62: Effect of hydrogen partial pressure on fatigue crack growth rate in pure H<sub>2</sub> relative to N<sub>2</sub> [156]. (Adopted by Hval [163]).**

Walter and Chandler [161] investigated the effect of hydrogen pressure in a SA 105 steel Grade II in the range of 7 to 100 MPa, at load ratios of  $R=0.1$ . Nelson et al. [164] tested a 1020 steel at low gas pressures, from 0.02 to 7 MPa. As shown in Figure 63, the effect of hydrogen gas pressure on FCGR is highly dependent on the  $\Delta K$ . At low  $\Delta K$ , the FCGR increase by more than a factor of ten at gas pressures in the range 0.02-100 MPa. However, at  $\Delta K$ -values higher than  $\sim 35$ -40 MPa $\sqrt{m}$ , and gas pressures above 69 MPa – 100 MPa (for SA 105 Grade II) the FCGR data from the different test, starts to merge. This indicate a threshold limit at which the FCGR is less influenced by the hydrogen gas pressure. This is suggested associated with a maximum solubility of hydrogen in the steel and/or a critical hydrogen concentration in the damage zone. Still, the increase of FCGR compared to data obtained in air is significant. For instance, at hydrogen gas pressures as low as 0.02 MPa, the FCGR is ten-fold higher than in air. The results in Figure 63 indicate that carbon steels are sensitive to accelerated FCGR even at low partial pressures and load ratios. These results are partly contradictory with the findings by Holbrook and Cialone [81], where the hydrogen influence on FCGR at load ratios below 0.4 was reported to be insignificant.

Recent studies have reported the occurrence of a maximum "saturation" threshold limit in FCG-data for low carbon steel. Yamabe et al. [165], revealed crack growth enhancement with increasing hydrogen gas pressure for an annealed low-carbon steel, JIS-SM490B ( $\sigma_y=360$  MPa). The FCGR as a function of  $\Delta K$  in air and hydrogen pressures from 0.1-90 MPa are shown in Figure 64 (a). The authors highlight the significant FCG acceleration that occurs with increasing  $\Delta K$  in the low  $\Delta K$  regime, i.e. at  $\Delta K < 20$  MPa $\sqrt{m}$ . Above this value, the acceleration in hydrogen gas was parallel to that obtained in air. As shown in Figure 64(b), the relative crack growth rate for hydrogen and air (the acceleration factor) was nearly constant at pressures between 0.7 ~ 90 MPa at  $f=1$ ,  $R=0.1$  and  $\Delta K=30$  MPa $\sqrt{m}$ . The authors attribute the behaviour to hydrogen saturation at the crack tip, causing a change in crack growth behaviour. The study elucidates the interplay between pressure and mainly frequency and their role on fatigue crack growth behaviour. This will be further discussed in the following section "Effect of Frequency".

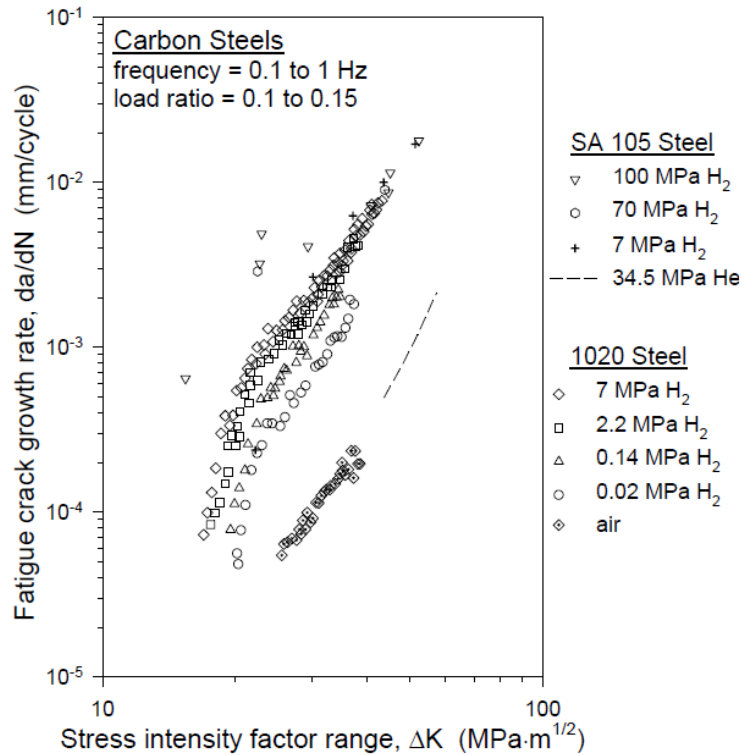


**Figure 63: Effect of hydrogen gas pressure on FCGR vs stress intensity factor for carbon steels compared to values in air [161] and Nelson [164].**

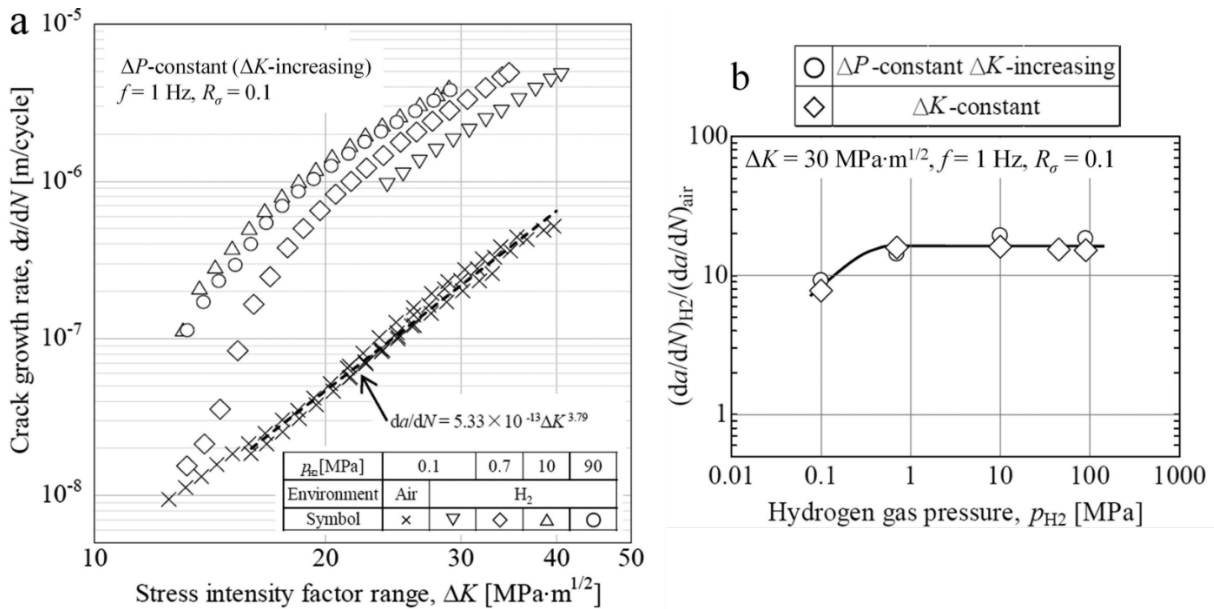


**Figure 64: Fatigue crack growth rate versus  $\Delta K$  and relative crack growth for hydrogen and air at hydrogen gas pressures between 0.1 and 90 MPa, for a low carbon steel (JIS-SM490B) [165].**



The NIST [40] have systematically tested both vintage (X52V) and modern (X52M, X70A and X70 B) pipeline steels at various hydrogen gas pressures and frequencies. The X52V vintage steel was produced in the mid-1960s and contained considerably larger amounts of carbon than the modern X52M steels produced in 2011; ~0.2 wt% versus 0.04-0.07 wt%, respectively. In addition, the vintage X52 featured an average grain size about 10 times larger than the other steels, that might influence hydrogen diffusivity. The X70A steel was obtained from a natural gas service pipeline while the X70B never had experienced service. Both X70A and X70B had similar chemistry but the microstructure differed somewhat due to differences in thermomechanical processing.

For all four steels tested, the FCGR is enhanced with increasing gas pressure from 5.5 MPa to 34 MPa at a cyclic loading rate of 1 Hz and increases with increasing  $\Delta K$ , see Figure 65 (a) for X52V and X52M and Figure 65 (b) for X70A and X70B. The X52V revealed a higher sensitivity to increasing gas pressure compared to the other materials (X52M, X70A and X70B), as shown in Figure 65 (a) and (b). However, at the lowest pressure, i.e. 5.5 MPa, the FCGR of X52V is below that of the X52M, indicating that this material exhibits a higher fatigue resistance at low hydrogen-gas pressures. When it comes to the X70 steels, the X70A revealed a slightly higher sensitivity to pressure than the one not used in service. Nevertheless, the data from both X70 steels at 34 MPa are within experimental spread of data. Moreover, data from both X70 steels at both pressures are comparable and at  $\Delta K$  values higher than 13 MPa $\sqrt{\text{m}}$ . This is consistent with the observed trend in the findings from Walter and Chandler [161] and Nelson et al. [164], where the FCGR starts to converge at a particular  $\Delta K$  (about  $\Delta K \approx 15 \text{ MPa}\sqrt{\text{m}}$ ) independently of hydrogen pressure.

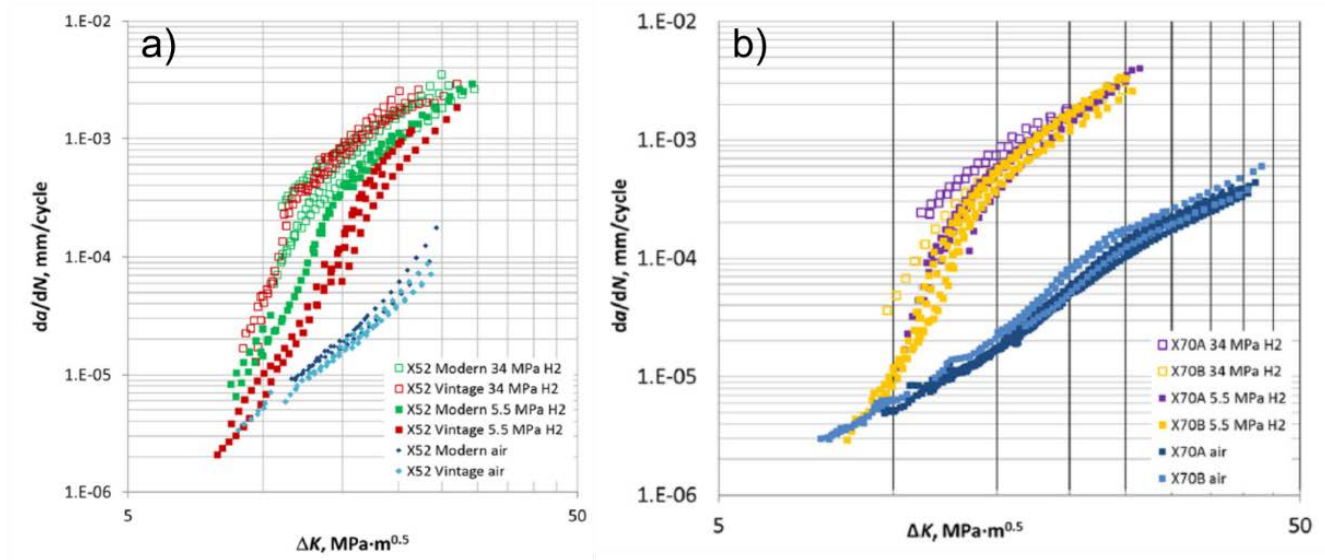


**Figure 65: Fatigue crack growth rate for a) two X52 steels (vintage and modern) and b) two X70 steels, one from in-service (X70a) and one not from service [40].**

Interestingly, there are surprisingly little differences between these materials. The X52 vintage steel have the highest sensitivity to HA-FCGR and X70A exhibit the highest FCGR for  $\Delta K$  in the range 11-14 MPa $\sqrt{m}$  at 34 MPa hydrogen pressure. Moreover, as seen from the overlap in data of X52M and X70B in Figure 66, both in air and in pressurized hydrogen environment, SMYS seems not to be an influential factor for FCGR for the modern pipeline steels [152].

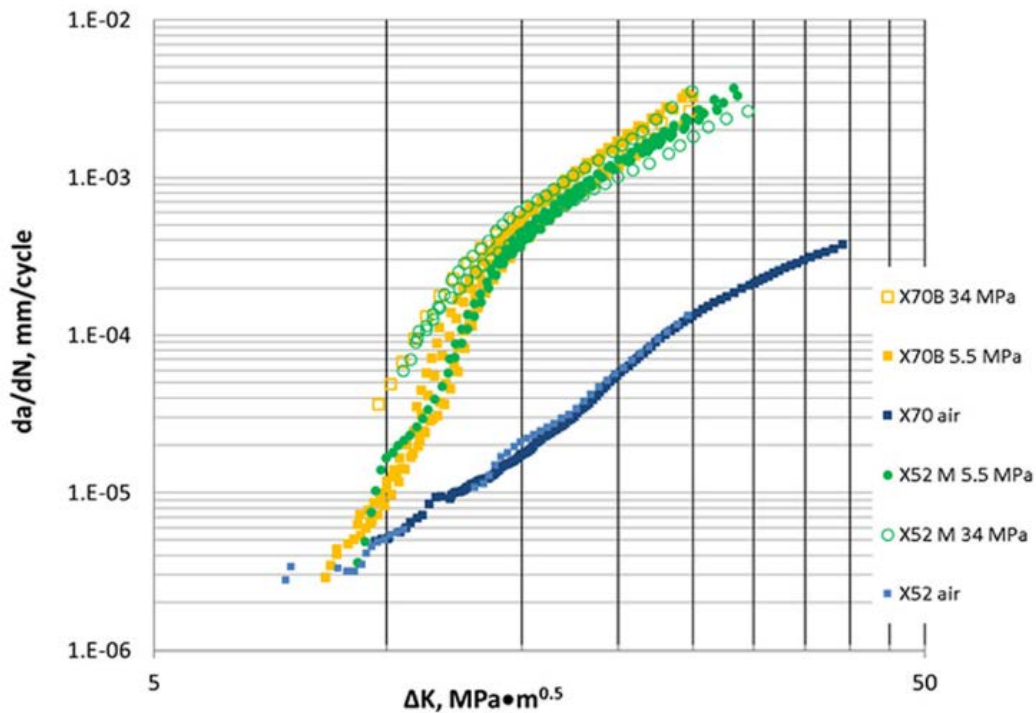
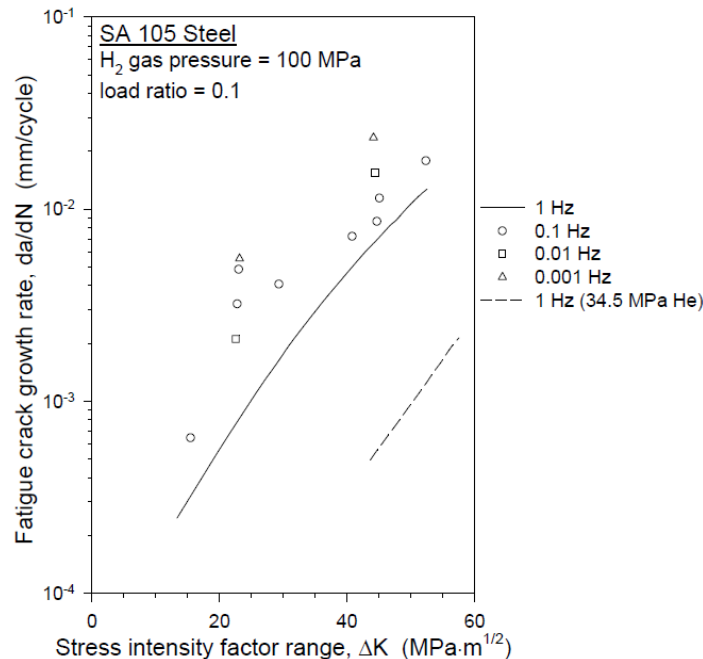


Figure 66: FCGR for X70 and X52 modern pipeline steel in hydrogen and air at both 5.5 MPa and 34 MPa [152]. Data from testing at NIST.

### 6.3.2 Effect of Frequency

Fatigue crack growth rates are generally reported to increase as the load cycle frequency decreases. In the work by **Holbrook et al.** [156], the effect of load cycle frequency was found to be less prominent. No significant changes occurred at frequencies between 0.1 and 10 Hz for a X42 pipeline steel in 1000psi (6.9 MPa) hydrogen gas [156]. The lack of frequency dependence within this range, is supported by others [166]. However, below 0.1 Hz, several researchers report a higher frequency dependence. Walter and Chandler [161] observed a significant frequency effect on the FCGR for SA 105 steel in 100 MPa hydrogen gas for frequencies from 0.001 to 1 Hz. The FCGR increased with a factor of 5, shown in Figure 67.



**Figure 67: Effect of load cycle frequency on FCGR for SA 105 steel in hydrogen gas [161].**

Recently, the research group at **Kyushu University** have performed extensive research on the topic of HE and cyclic loading on various materials using high pressure H<sub>2</sub> gas [165, 167-171]. Matsui et al. [170] found a remarkable frequency dependence of FCG acceleration in 0.7 MPa hydrogen gas for a low-alloy steel (JIS-SCM435). FCG acceleration gradually increased with decreasing frequency, reaching a peak at ≈0.1 Hz and subsequently followed by a sudden acceleration in FCGR. Yamabe et al. [165] showed that a similar frequency dependence occurs in low carbon steel under hydrogen pressures ranging from 0.1 to 90 MPa, at frequencies ranging from 0.001 to 10 Hz. Figure 68 shows the relative FCG acceleration ratio  $(da/dN)_{H_2}/(da/dN)_{air}$  vs test frequency for various pressures for a constant  $\Delta K$  (30 MPa $\sqrt{m}$ ) during the tests. At a loading frequency lower than the value at the peak of acceleration, a sudden drop in FCG acceleration ratio occurs at H<sub>2</sub> gas pressures below 10 MPa. The peak shifts towards lower frequencies when increasing the pressure from 0.1 to 10 MPa. Using laser microscope, the fatigue crack morphology was revealed and correlated with SEM micrographs of the fracture surface, as shown in Figure 69. The crack surface obtained in air at f=10 Hz consisted of extensive slip bands, distributed along the crack. The corresponding striations observed at the fatigue fracture surface in SEM did not show any significant difference with the one tested in air. In contrast, at the frequency of 1 Hz in 0.7 MPa H<sub>2</sub> gas, the FCGR accelerated nearly by a factor of 10 and only a few slip bands were observed along the crack. Also, flat and blurred striations were observed on the fracture surface for the accelerated crack growth, indicating a shift in the underlying crack growth mechanism. Moreover, similar characteristics to that obtained in air was observed in 0.7 MPa hydrogen gas at the frequency of 0.001 Hz. At higher pressure levels, the FCGR gradually increased with decreasing test frequency (at least to f=0.001 Hz).

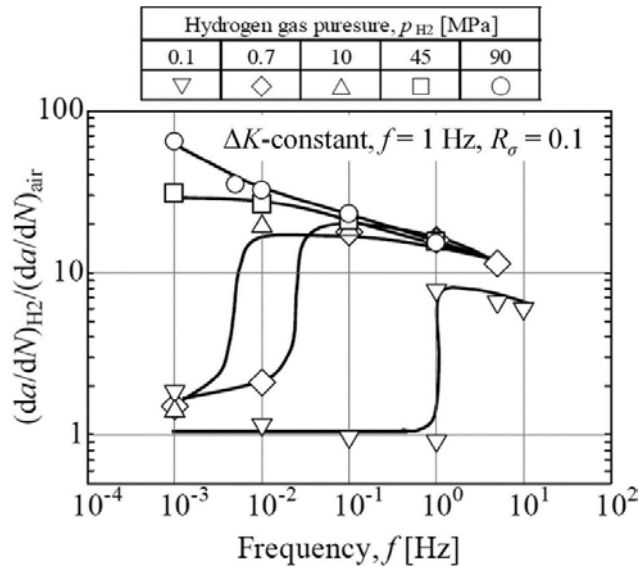


Figure 68: Effect of frequency on relative fatigue crack growth rate in hydrogen gas pressures of 0.1-90 MPa [165].

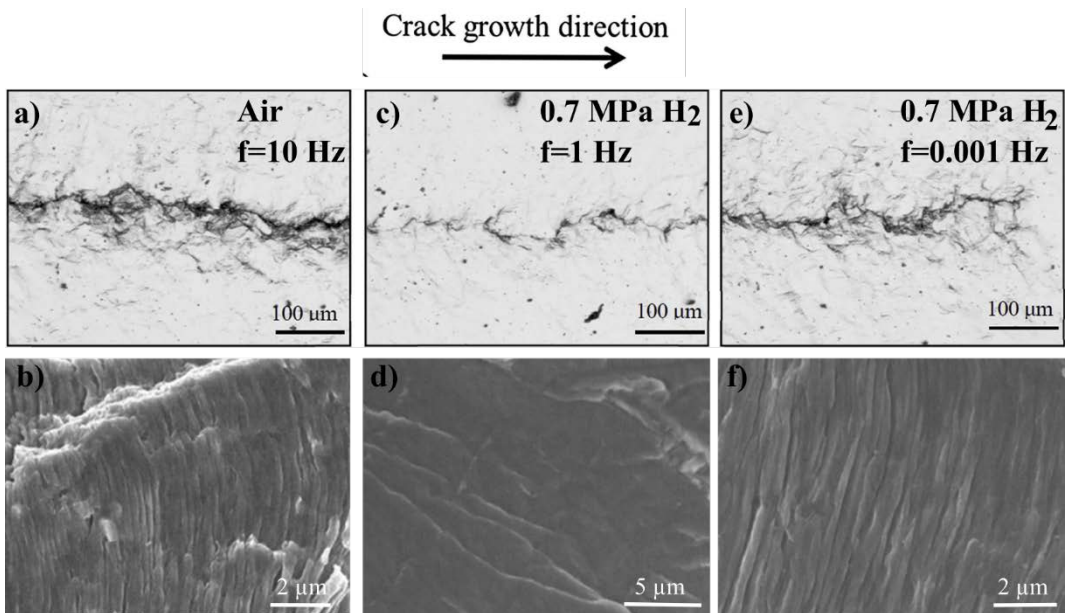
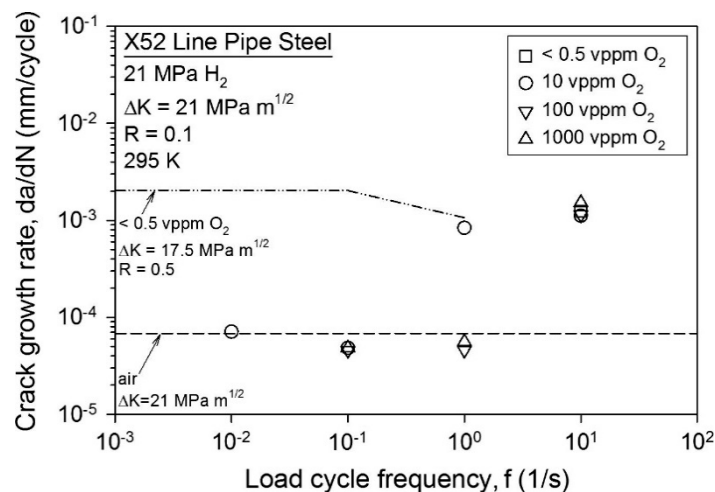


Figure 69: Fatigue crack growth morphology and corresponding fatigue fracture surface for a low carbon steel (JIS-SM490B) after  $\Delta K$ -constant tests (30 MPa $\sqrt{m}$ ) in (a-b) air at RT,  $f=10$  Hz and  $da/dN=1.9 \cdot 10^{-7}$  m/cycle,  $s=0.22 \mu m$ , (c-d) 0.7 MPa hydrogen gas at  $f=1$  Hz and  $da/dN=2.2 \cdot 10^{-6}$  m/cycle,  $s=2.2 \mu m$  (e-f) 0.7 MPa hydrogen gas at  $f=1$  Hz and  $da/dN=3.2 \cdot 10^{-7}$  m/cycle,  $s=0.30 \mu m$ . Figure adopted from [165, 167].

Matsuo et al. [170] proposed that the sudden acceleration in FCGR is being linked to a steep hydrogen gradient at the crack tip which in turn enhanced localized plasticity and consequently increasing the crack growth per cycle. This is in accordance to the HELP mechanisms for which crack tip blunting is suppressed and faster crack propagation occur. Based on these assumptions, Yamabe et al. [165, 167] developed a criterion, involving a simplified parameter  $(P_{H_2} \times f)^{1/2}$ , to estimate the

frequency at which hydrogen-induced acceleration would disappear, where the  $(P_{H_2} \times f)^{1/2}$  quantify the gradient of hydrogen concentration ahead of the crack tip accounting for hydrogen pressure, frequency and temperature. However, it has been questioned if this criterion is sufficient to capture the complexity of FCGR increase, since the  $\Delta K$  is considered to be constant in this case [153]. The FCGR acceleration was related to the hydrogen-induced successive crack growth (HISCG) mechanism [131, 172].

Somerday et al. [173] revealed that frequency dependence is modified according to the oxygen content in the hydrogen gas. From the FCGR test on a X52 pipeline steel in a 21 MPa hydrogen gas pressure containing 10, 100 and 1000 vol. ppm oxygen, it was proposed that during the crack opening process, oxygen adsorption in the newly created crack surfaces would restrict hydrogen entry. Indeed, the resulting hydrogen-induced accelerations were less prominent at lower frequencies, i.e. 0.001 Hz, due to longer time for oxygen to adsorb, as shown in Figure 70. The FCGR immediately decreased to the level obtained in air, when reducing the frequency from 10 to 0.1 Hz. Nevertheless, it is still not verified that the HISCG mechanism is dominating the hydrogen induced FCGR acceleration when considering different test conditions, environments and materials.



**Figure 70: Effect of cyclic loading frequency on FGCR for X52 pipeline steel in mixed H<sub>2</sub> + O<sub>2</sub> gases at R=0.1 and K=21 MPa√m. FCGR data from tests in air and high-purity H<sub>2</sub> gas at 10 Hz are included for comparison [173].**

Within the comprehensive testing program of FGC of pipeline steels at NIST, various variables, including cyclic loading frequencies, have been investigated [40]. X52 modern and vintage -and X70 pipeline steels were tested over the frequency range 0.01-1 Hz, at R=0.5 for hydrogen gas pressures of 34 MPa and 5.5 MPa. Overall, the frequency dependence on HA-FCGR (Hydrogen-assisted fatigue crack growth rate) was low for all pipeline steels, at a hydrogen gas pressure of 34 MPa. Figure 71 shows the da/dN vs frequency for a X52 vintage -and modern pipeline steel. Similar characteristics in FCGR is observed for each material at frequencies of 0.1 and 1 Hz. FCGR is higher at the lowest frequency, 0.01 Hz. These results have been obtained only for the X52M, since no successful tests

were completed for the X52V at this frequency. However, the authors assume small differences between FCGR's for X52M and X52V at 0.01 Hz, due to similar variation in FCGR already seen from at 1 Hz and 0.1 Hz.

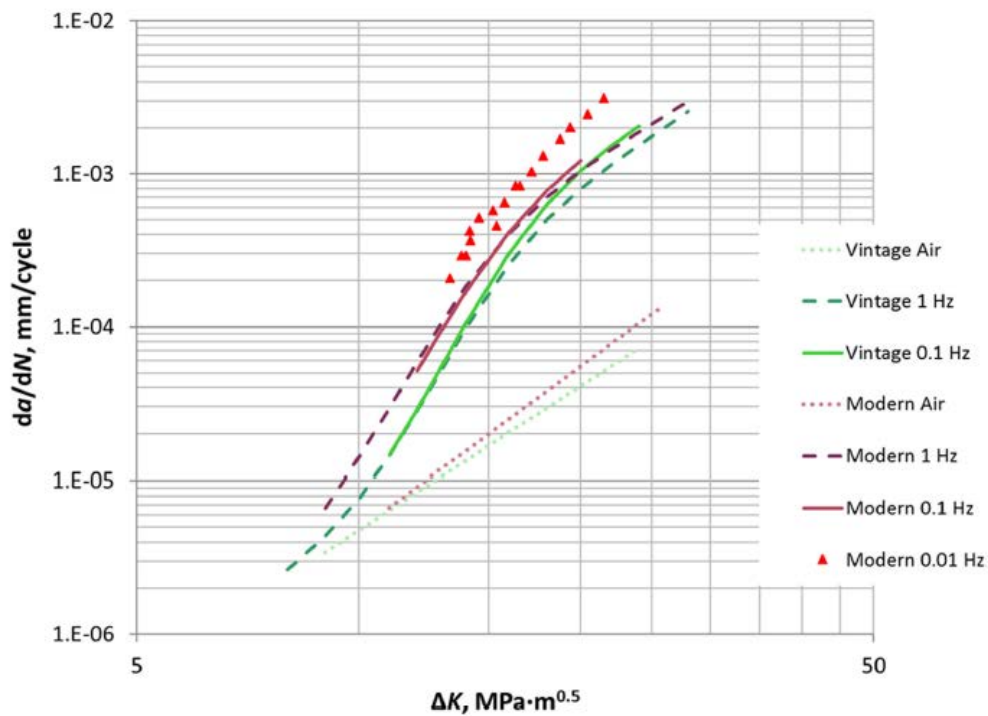


**Figure 71: Effect of cyclic loading frequency on FCGR in a modern and vintage X52 pipeline steel at a hydrogen pressure of 5.5 MPa [40].**

At the highest gas pressure, 34 MPa less frequency dependence is observed compared to that at 5.5 MPa hydrogen gas. The authors attribute the lack of frequency dependence to hydrogen saturation. Figure 72 shows the FCGR vs loading frequency at  $\Delta K$  of 14 MPa $\sqrt{m}$  for all four materials. At this stress intensity factor, X52V is less affected by a lower load frequency. On the other hand, X52M and X70A show an increase in FCGR at the lowest load frequency. Moreover, the increase in H<sub>2</sub> pressure from 5.5 MPa to 34 MPa is more influential than the effect of decreasing the frequency.

Generally, hydrogen-enhanced fatigue crack growth is related to hydrogen diffusion and increased hydrogen concentration near the crack tip [172]. Accordingly, a decrease in frequency can be expected to have similar effect as an increase in gas pressure. At lower frequencies, hydrogen atoms will have more time to diffuse towards the crack tip per cycle. Moreover, as the pressure influences the hydrogen uptake and thus the hydrogen flux, the driving force for hydrogen-enhanced fatigue crack growth is higher.

This effect is clearly shown for the X52 vintage steel at higher pressures, shown in Figure 65 (a). On the contrary, the authors claim that the frequency dependence on FCGR for X52V is not evident as reported in Figure 72 (a). It must be pointed out that the  $da/dN$  value for X52V at  $f=0.01$  are just an assumption; it is assumed that the change in FCG acceleration for X52V from 0.1 to 0.01 Hz, is the same as for the X52M. The X70A steel shows a slightly higher decrease in FCGR at the lowest loading frequency at 34 MPa gas pressure.

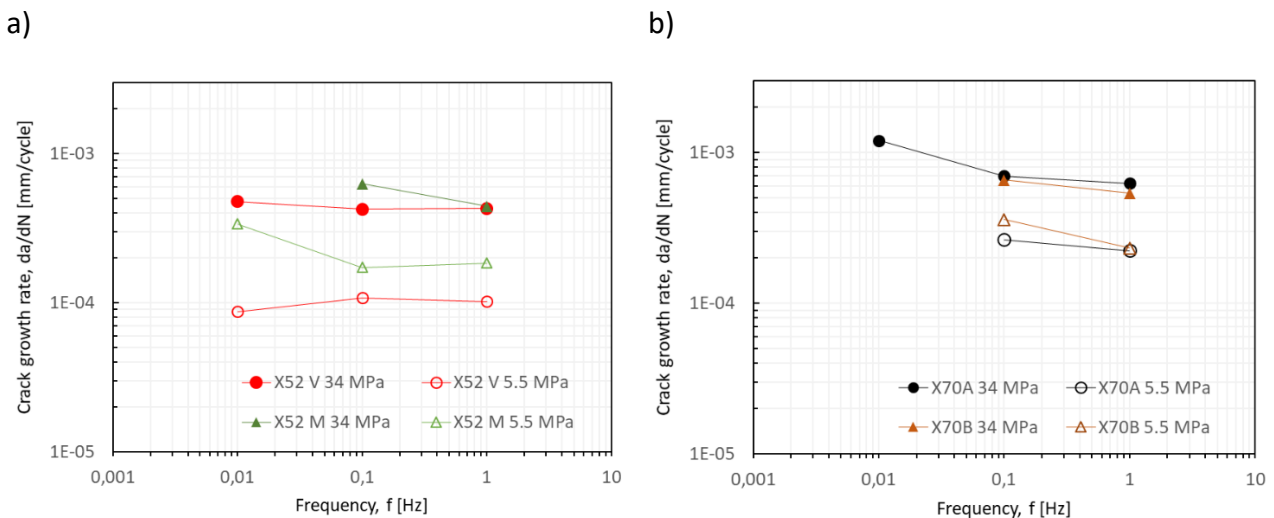


**Figure 72: FCGR as a function of test frequency at  $\Delta K$  of 14 MPa $\sqrt{m}$  and hydrogen gas pressure of 5.5 and 34 MPa for a) modern and vintage X52 and b) X70A and X70B. Data adopted from [40].**

Alvaro et al. [174, 175] investigated the effects on HA-FCGR in a Fe3%Si and X70 under in-situ cathodically charged hydrogen conditions at frequencies of 0.1, 1 and 10 Hz. The influence of hydrogen on FCGR was clearly test frequency dependent, as shown in Figure 73. These two materials show to some extent qualitatively comparable hydrogen-induced frequency dependent behaviour. However, the authors highlight the quantitative differences, such as 500 times higher crack growth acceleration for Fe-3wt%Si in hydrogen than in air, compared to an acceleration factor of 70 for X70. Furthermore,  $\Delta K$  appears to be independent of hydrogen in the Paris' domain for Fe-3wt%Si, indicated by small variations in  $m$  (material and test condition dependent constant), from Paris law,  $da/dN=A \Delta K^m$ . With decreasing frequency, the curves shifted to higher stress intensity ranges while the FCGR in X70 exhibited a transition at frequencies of 1 Hz. The authors attribute the higher embrittlement sensitivity in Fe-3wt%Si to the Silicon containing alloy. This is previously shown to strongly favor cleavage cracking and consequently causing a strong acceleration of the FCGR [176].

EBSD and ECCI post-mortem deformation analysis of the two tested materials, revealed striking similarities in the underlying dislocation structure between X70 steel and pure iron. These results indicate that there is no significant difference in the basic dislocation behavior between pure iron and X70 pipeline steel, weather it is tested in gaseous hydrogen [177-179] or electrochemical

charging hydrogen conditions. Nevertheless, the effect of electrochemical charging parameters is still not fully understood.

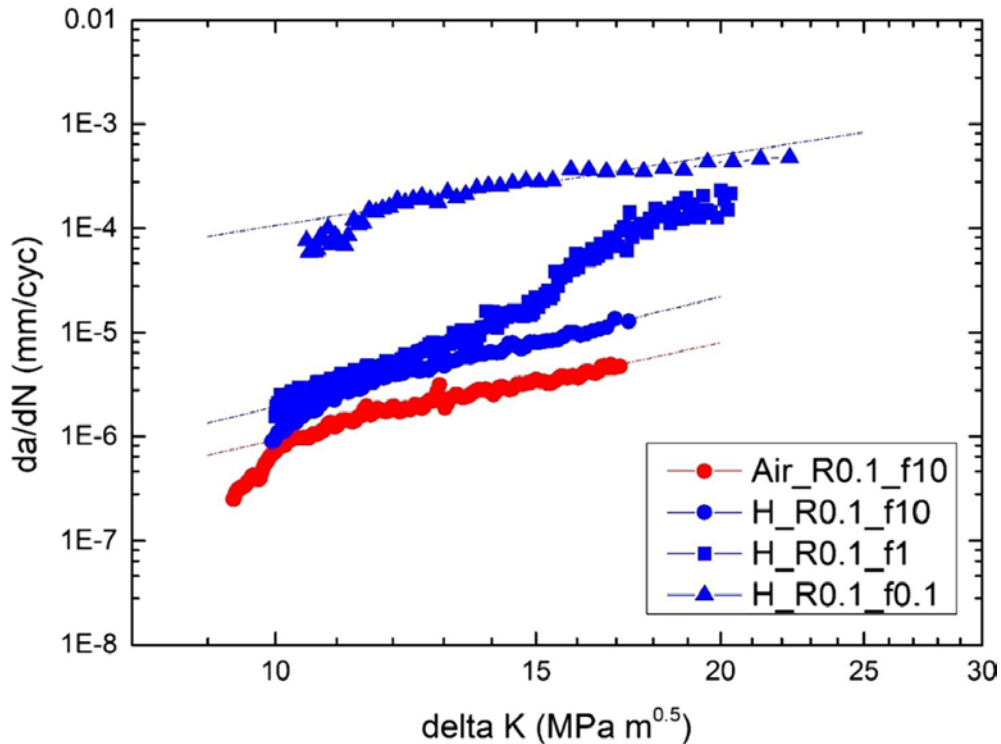


Figure 73: FCGR of a X70 pipeline steel at load cycles frequencies of 0.1, 1 and 10 Hz from in-situ electrochemical charged tests, compared with test in air [175].

### 6.3.3 Effect of Stress Ratio

The load ratio,  $R$ , is considered an important but not overall controlling factor for the hydrogen influence on the FGCR. The cyclic stress intensity range,  $\Delta K$ , is related to  $K_{max}$  by the following [159]:

$$\Delta K = (1 - R)K_{max} \tag{26}$$

The load ratio seems to affect the transitions between the fatigue crack growth regimes. Usually, the FCGR in gaseous hydrogen increases with increasing  $R$  at a constant  $\Delta K$ . However, conflicting data exist on the effect of load ratio on FCGR (it should be noted that changing the load ratio involves changing the max load, mean load, extent of closure mechanisms that can be contributing reasons for discrepancies).

Suresh and Richie [149] investigated several pressure vessel and pipeline steels in hydrogen and moist air. A schematic diagram based on their findings of load ratio and frequency effects in low carbon steel, is presented in Figure 74. They demonstrated that there is a critical maximum stress intensity factor,  $K_{max}^T$  for the onset of the intermediate regime, at which hydrogen-assisted crack



growth acceleration decreases with increasing R. In other words, for a given pressure, the onset of accelerated FCGR will be shifted to lower stress intensity factor values as R increases. This behaviour was also seen in the threshold stress intensity range,  $\Delta K_0$ , below  $10^{-6}$  mm/cycle (Regime A), below which crack growth are experimentally undetectable. The major role of hydrogen was evident below  $10^{-6}$  mm/cycle at low load ratios; crack growth rates in dry hydrogen gas was found to be about two orders of magnitude higher and threshold,  $\Delta K_0$ , was 50% lower than that obtained in air. However, crack growth rates and threshold values for air and hydrogen were comparable at higher load ratios (R=0.75).

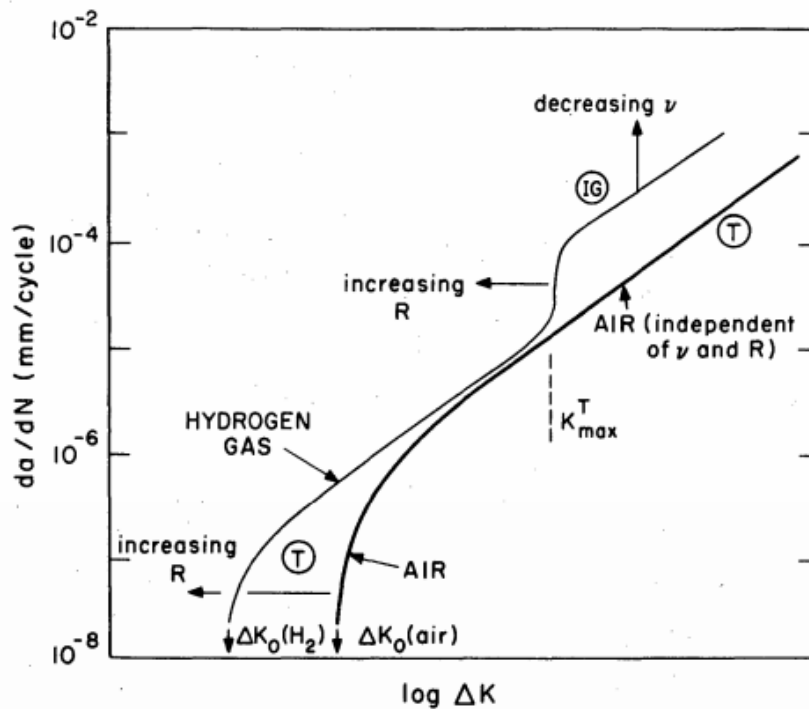


**Figure 74: Schematic representation of the hydrogen (dry gas) effect on fatigue crack growth in low strength steels (R= load ratio,  $\nu$ = frequency, T= predominantly transgranular fracture and IG= predominantly intergranular fracture) [149].**

This is consistent with recent findings in the work by San Marchi et al [113]. In contrast, Cialone and Holbrook [81] found that while the load ratio linearly increased the FCGR for a X42 steel when tested in nitrogen, a similar trend was observed only for  $R < 0.5$  in hydrogen gas. For low load ratios the FCGR was unaffected in the presence of hydrogen.

The main findings are summarized in Figure 75 for  $\Delta K = 10$  MPa $\sqrt{m}$  the crack growth rate in nitrogen gas increases steadily with R. Contrary, the load ratio in hydrogen gas appears to have minor influence on the crack growth rate up to 0.4. The authors explain such behaviour stating that at higher R values, the FCGR increases due to the critical condition where  $K_{max}$  approaches the fracture toughness in hydrogen gas (obtained from monotonic loading conditions). Therefore, they relate

this load ratio effect to the onset of Stage III as a result of a HE-induced reduction in energy required for ductile crack growth. On the other hand, Cialone and Holbrook attributed the differences in FCGR trends at low R-values in hydrogen and nitrogen environment to the crack closure process that can limit the FCGR through a bridging of cracked surfaces around asperities from corrosion products, second-phase particles or the crack fracture surface itself. The extent of plasticity-induced crack closure is suggested to be less pronounced in the presence of hydrogen compared to that of nitrogen [141]. Similar behaviour was also observed for a X70 pipeline steel.

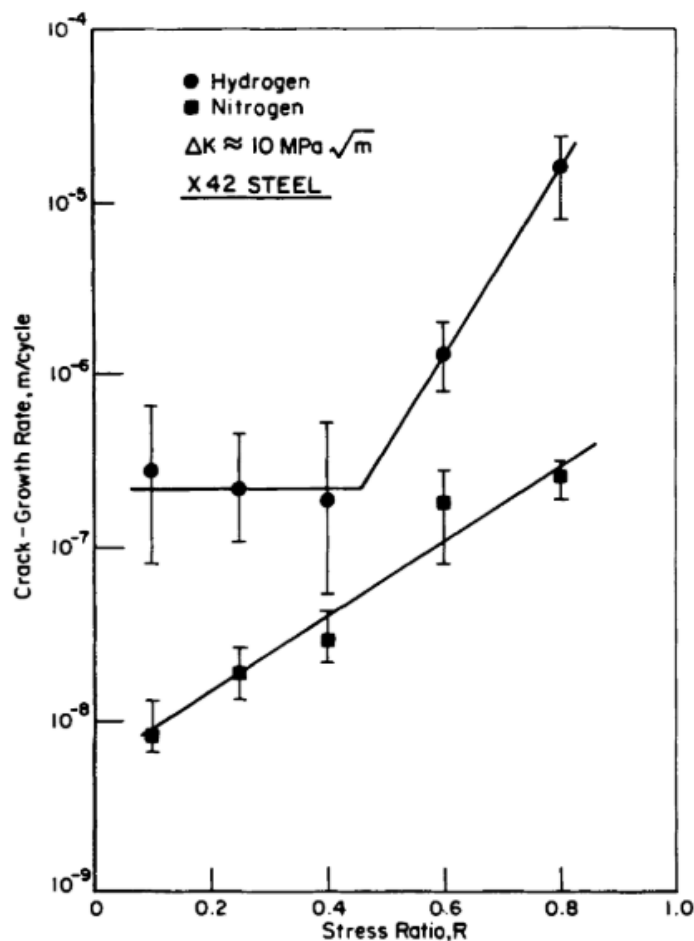


**Figure 75: Effect of stress ratio of FCGR in X42 pipeline steel in hydrogen and nitrogen gas at 6.9 MPa,  $f=1$  Hz,  $\Delta K=10$  MPa $\sqrt{m}$  [81].**

Somerday et al. [173] studied a X52 pipeline steel in 21 MPa hydrogen gas at  $R=0.1$  and  $0.5$ . At both load ratios, the  $da/dN$  vs  $\Delta K$  curves shows similar characteristics, as reported in Figure 76. However, in agreement with the work by Suresh and Ritchie [149], the onset of acceleration is shifted to lower stress intensity ranges at the highest load ratio,  $R=0.5$ . Moreover, the crack growth rates at  $R=0.5$  were higher than those at  $R=0.1$  over the entire  $\Delta K$  range.

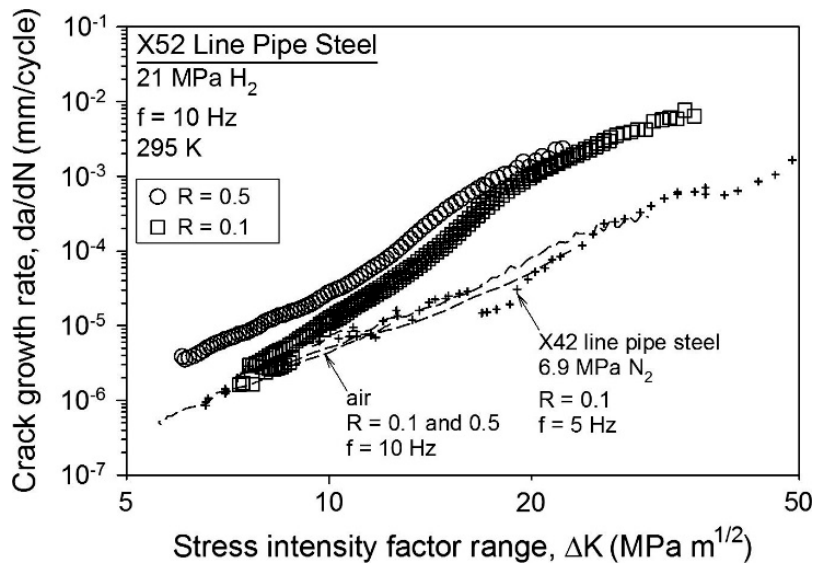


**Figure 76: da/dN vs stress intensity factor range ( $\Delta K$ ) for X52 pipeline steel at load ratios R=0.1 and 0.5. [173]. FCGR data for X42 from the work by Cialone et al. [81] are included for comparison with data in air.**

Roy et al. [180] studied the FCGR behaviour of a HSLA steel (~650 MPa) with in-situ hydrogen charging and load ratios in the range from 0.1-0.5. The load ratio was changed in-situ during cyclic loading at a constant frequency in both air and in hydrogenated samples. As shown in Figure 77, an onset of FCG acceleration occurs immediately after the load ratio is shift from 0.1 to 0.5. The increase in FCGR with increasing R were attributed to a combination of high mean stresses which favour hydrogen damage. In addition, the high mean stresses would also enhance plastic damage therefore facilitating mechanical fatigue effects as detectable from the FCGR curve in air.

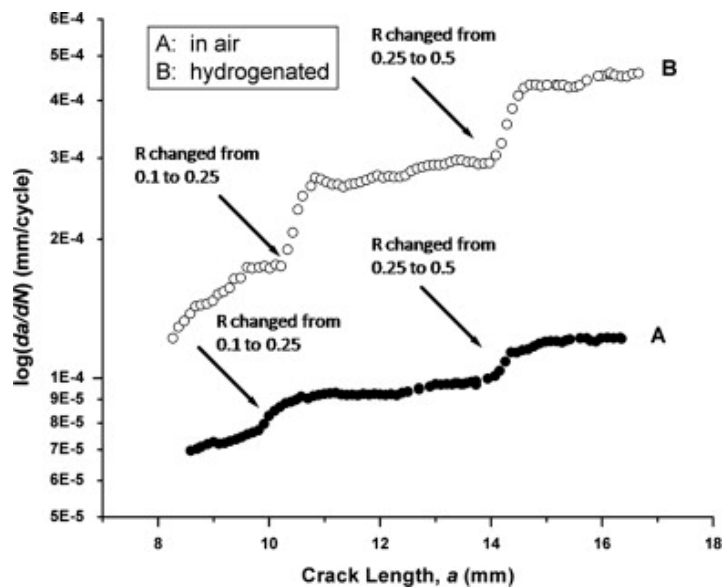


**Figure 77: Effect of R on the crack growth rate in air and hydrogen environment with a  $\Delta K=22 \text{ MPa} \cdot \text{m}^{1/2}$  [180].**

### 6.3.4 Effect of Microstructure and Yield Strength

Degradation of fracture resistance by HE mainly occurs in steels with high tensile strength or high hardness. However, hydrogen induced fatigue crack growth is present in materials that are conventionally considered less susceptible to hydrogen embrittlement, including low strength C-Mn steels [156].

Cialone and Holbrook compared the FCGR of a X42 pipeline steel, consisting of a ferritic-pearlitic microstructure, a pearlitic (AISI 1080 steel,  $\sigma_y \approx 410$  MPa) and a fully ferritic steel alloy ( $\sigma_y \approx 110$  MPa), at 1 Hz,  $R = 0.1$  in 6.9 MPa hydrogen and nitrogen gas pressure. In addition, for comparison with a more complex microstructure, data from X70 pipeline steel ( $\sigma_y \approx 600$  MPa) was included. The X70 steel primarily consisted of polygonal ferrite, acicular ferrite and martensite. The data plotted in Figure 78, reveal that there is no obvious detrimental effect of increased material strength on FCGR in hydrogen. Instead, FCG measurements suggest that the microstructure is more critical. Overall, all four alloys exhibit enhanced FCGR in hydrogen when compared to nitrogen environment. This effect is more prominent in the alloys with a larger ferrite content. For instance, the HA-FCGR curves for the fully ferritic alloy, such as the X70 and X42 steels were clearly higher than those in nitrogen gas. The X42 and X70 steels predominantly consisted of equiaxed ferrite and polygonal ferrite, respectively. The 1080 alloy with a pearlitic microstructure had minimal change in the FCGR in hydrogen when compared with that in nitrogen. The X70 alloy, the one with the highest strength, exhibited the overall lowest FCGR in hydrogen gas. This is contradicting the results obtained from monotonically testing of the four alloys, where the alloys with highest strength typically exhibited highest HE susceptibility. The fatigue results however indicate that X70 with the highest strength was not inferior to the lower strength steel, i.e. X42.

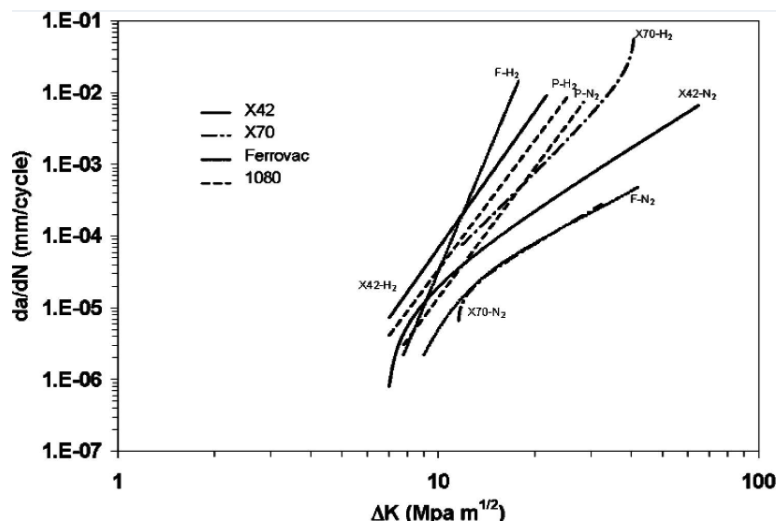
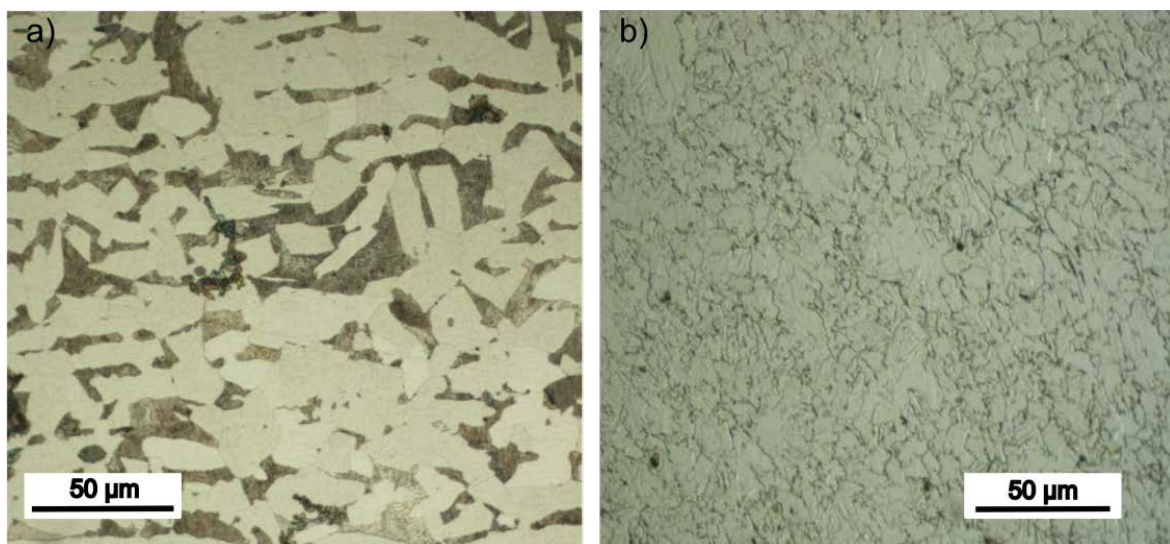


Figure 78: Effect of different microstructure and yield strength on HA-FCG in pipeline steel. Figure from [159].

Microstructures of modern pipeline steels, produced from the early 2000`s, differ significantly from older pipelines both in chemical composition and microstructure. In general, older pipeline steels consist of a ferrite/pearlite microstructure, while modern pipeline steels in addition to a lower carbon content have an acicular ferrite and bainitic microstructure.

Slifka et al. [155] demonstrated that monotonic performances have little effect on FCGR in modern pipeline steels, X52 and X70. Three of the tested alloys, X52 (produced in 2011) and two X70 steels (some microstructural differences), exhibited comparable FCGR when tested in 34 MPa hydrogen pressure, at a loading frequency of 1 Hz and  $R= 0.5$  (see Figure 66). A similar trend was observed at 5.5 MPa hydrogen pressure, for the three newer steels (X52modern + two X70 steels). The X52 vintage steel, however, showed lower FCGR than the modern at  $\Delta K$  levels below 25 MPa $\sqrt{m}$  and at low hydrogen pressure. The higher crack growth resistance at low pressures observed for the vintage steel was attributed to the microstructure. All the modern pipeline steels had similar microstructures. The modern X52 and X70 pipeline steel, had a fine homogeneous grain structure consisting of polygonal ferrite, acicular ferrite with presence of dispersed carbides. The X70 materials also contained some phases of upper bainite (X70A) and pearlite and acicular ferrite (X70B). The X52 vintage design from the 1960`s, consisted of a ferrite/pearlite microstructure, with ten times larger grain size and a significantly higher carbon content than the modern steels (0.235 wt% versus 0.07 wt% for X52M). The larger grain size results in a larger distribution of the hydrogen trapped in the grain boundaries, consequently, a relative lower hydrogen content per area is assumed to contribute to the lower FCGR observed for X52V. Figure 79 shows optical microscopy images of both microstructures. A more detailed distinction between these microstructures are described in section "Materials".



**Figure 79: Optical microscopy images with mag. X500 of a) X52 vintage steel with ferrite-pearlite microstructure and b) X52 modern steel with polygonal ferrite and a mixture of acicular ferrite and dispersed carbides. Figure adopted from [155].**

None of these steels shows the typical microstructural banding related to chemical segregation at the centreline. Thicker walled-pipes commonly presents this banded microstructure with alternating layers of ferrite and pearlite elongated in the rolling direction [181]. This results in higher level of anisotropy which influences the mechanical properties.

Ronevich et al. [182] showed that the orientation of the banded ferrite-pearlite microstructure had distinct effects on fatigue crack growth rates for a X65 steel in air and in 21 MPa hydrogen gas at  $R=0.5$ . The definitions of the various orientations with respect to microstructural banding and the resulting  $da/dN$  vs.  $\Delta K$  relationship are shown in Figure 80 and Figure 81 (a-b). Figure 81 (b), contains additional data for X52, X60, X70 and X80 steels that do not contain a banded microstructure [113, 160, 183, 184]. The fatigue crack growth rate in hydrogen gas was higher in the C-L and L-C orientations (crack parallel to the banded pearlite) than for the L-R orientation (crack oriented perpendicular to the banded pearlite), illustrated in Figure 81 (a). Crack propagation across the L-R orientations encounters the alternating layers of ferrite and pearlite whose boundaries act as a barrier for crack propagation. While crack propagation in the C-L and L-C orientation occurs parallel to the banding.

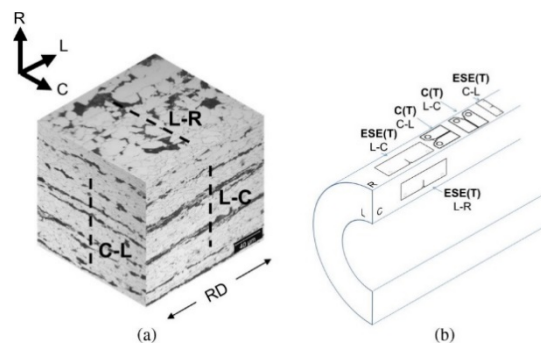


**Figure 80: a) Isometric view of the microstructural banding of a X65 pipeline steel, in the longitudinal (L) and circumferential (C) directions. b) Schematic illustration of the test specimen in the pipe [182].**

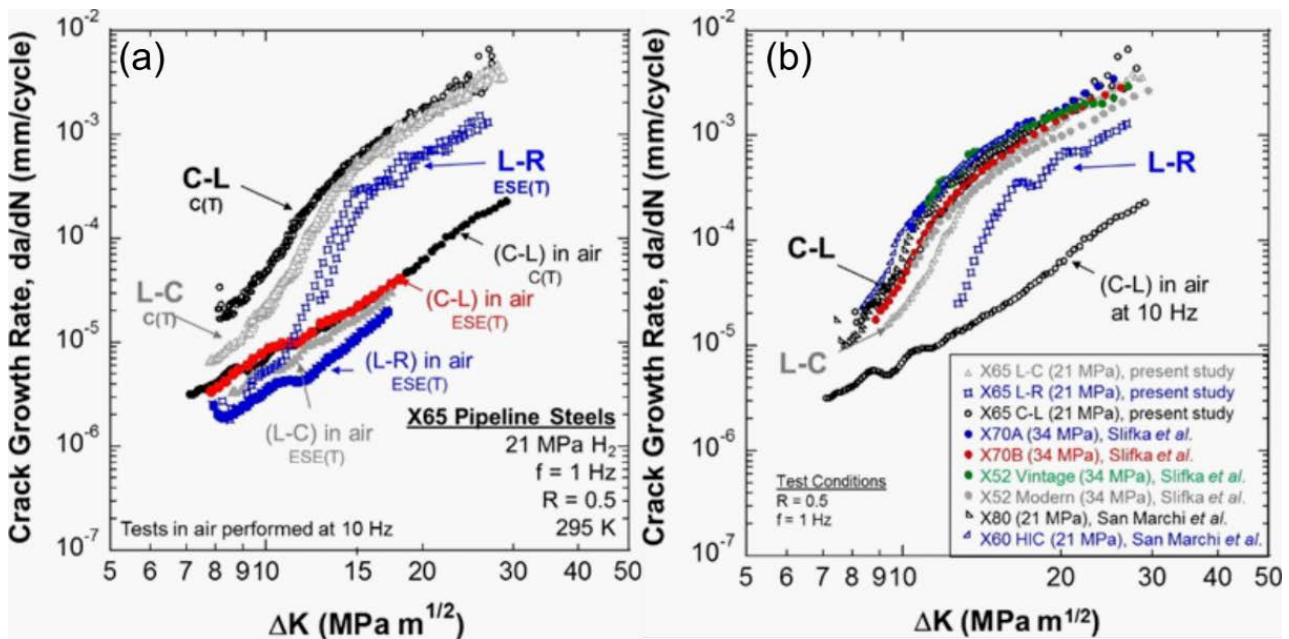
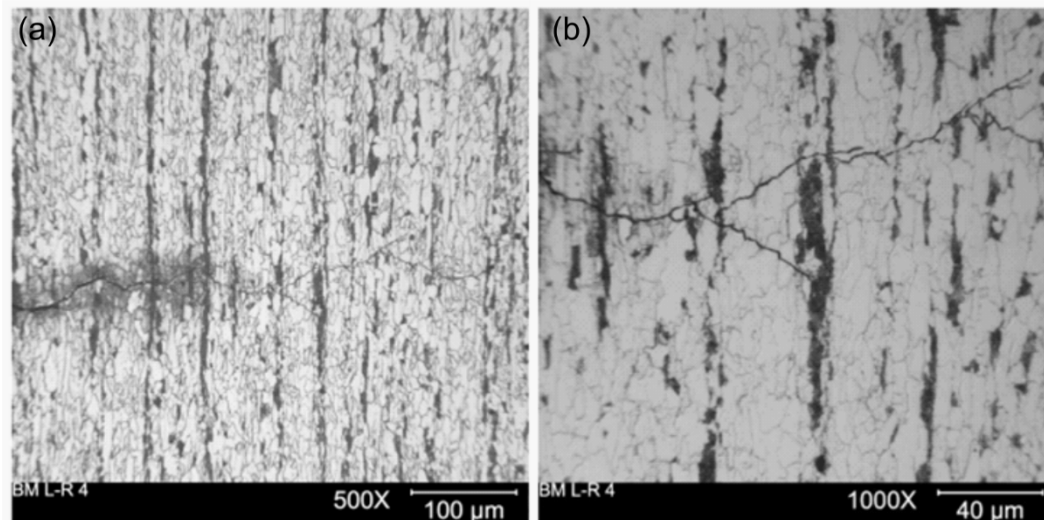


Figure 81:  $da/dN$  vs  $\Delta K$  from a) tests in air and in hydrogen gas (21 MPa) for various crack growth orientations and b) FCGR curves from the present study compared to other literature [40] [182].

In Figure 81(b), the collected data from other steels are comparable with those for X65 in the C-L and L-C Orientations (despite some scatter). However, the X65 data for the L-R oriented specimens clearly showed lower fatigue crack growth rates than the earlier reported results in Figure 81(b). The tested X65 pipeline steel contained an anisotropic microstructure with elongated grains in the longitudinal and circumferential direction. Thus, the crack plane in L-R oriented specimens intersects with alternating layers of ferrite and pearlite, compared to that in the L-C and C-L oriented specimens.

Optical micrographs from the L-R oriented specimen, see Figure 82, shows the primary crack propagation (from left to right) perpendicular to the banded structure with secondary microcracks branching from the primary crack plane. Crack-tip branching typically occurs with interaction of hard phases such as pearlite or cementite. This can either deflect or arrest the crack. L-C and C-L oriented specimens did not exhibit branching in air. Fracture surfaces from tests in hydrogen gas revealed some secondary cracking. However, these did not reflect branching, but rather delamination along bands which appear as secondary microcracks.

The limited hydrogen assisted fatigue crack growth in the L-R direction was mainly attributed to the impeded hydrogen diffusivity through the pearlite layers that limits the hydrogen supply to the crack tip. Additionally, it has been reported [10, 11] that crack branching induces a shielding effect, reducing the local crack tip driving force.



**Figure 82: Optical micrographs of X65 pipeline steel with fatigue crack propagation in the L-R orientation (perpendicular to the pearlite banding) in 21 MPa hydrogen gas, at (a) low magnification and (b) higher magnification, revealing the crack path with crack branching at  $\Delta K \sim 26 \text{ MPa}\sqrt{\text{m}}$  [182].**

### 6.3.5 Effect of Gas Composition

The occurrence of hydrogen embrittlement in an existing crack in a gaseous environment with high purity hydrogen gas, includes several processes, such as 1) transport of hydrogen to the crack tip surface, 2) physical adsorption of the hydrogen gas molecules, 3) chemical adsorption of the hydrogen atoms, 4) atomic entry into the crack tip, 5) diffusion to the embrittlement site and finally the 6) hydrogen-material interaction, resulting in crack extension (Nelson and Wei [164]). However, hydrogen damage may be inhibited by adding small amounts of impurities to the hydrogen gas, for example, oxygen, carbon composed molecules and sulphur with unsaturated chemical bonds (Somersday [173]).

Cialone and Holbrook demonstrated that X42 pipeline steel obtained nearly full inhibition of hydrogen accelerated FCGR by testing in a gas mixture consisting of additives such as COS, O<sub>2</sub> and C<sub>2</sub>H<sub>4</sub>. The FCGR from these tests were comparable to those exhibited in pure nitrogen gas. However, these tests were only performed at a load frequency of 1 Hz. Results from surface characterization methods, such as XPA (x-ray photoelectron spectroscopy), TDS (thermal desorption spectroscopy) and AES (Auger electron spectroscopy), revealed that some gas additives, were more promising than others; gases with C, S and O, block adsorption due to the formation of semi-stable bonds with the iron surface. For instance, C<sub>2</sub>H<sub>4</sub> and O<sub>2</sub> had the most prominent inhibition effect. O<sub>2</sub> however, might introduce concern such as flammability when mixing with hydrogen.

Nelson et al. [164] also showed that additions of other gases could be used to suppress HA-FCGR in hydrogen gas. They explored a 1020 steel at a load cycle frequency of 1 Hz and tested in three different gas mixtures: hydrogen and carbon dioxide, hydrogen and natural gas and hydrogen and



water. Water vapor reduced the HA-FCG rates compared to those in pure hydrogen gas, while additions of CO<sub>2</sub> and natural gas, either increased the FCGR or had minimal effect on inhibiting HA-FCG. Additions of CO were shown to have nearly full inhibition effect on the FCGR.

Somerday et al. [173] showed that the addition of O<sub>2</sub> effectively prevented HE in low strength X52 steel. Fatigue crack growth tests were conducted in high-purity hydrogen and with additions of 10, 100 and 1000 wppm oxygen. Tests in hydrogen gas containing up to 1000 wppm oxygen, were comparable to results obtained in inert gas or air at low to medium  $\Delta K$  levels. However, a sudden acceleration occurred above a critical  $\Delta K$  level that depended on the oxygen concentration, as shown in Figure 83. The FCGR curves at 10 wppm oxygen and high purity hydrogen were comparable. Tests at 100 and 1000 wppm oxygen exhibited accelerated crack growths displaced to higher  $\Delta K$ . The operating mechanisms responsible for this behaviour are discussed in section 6.6 Effect of inhibitors from [138].

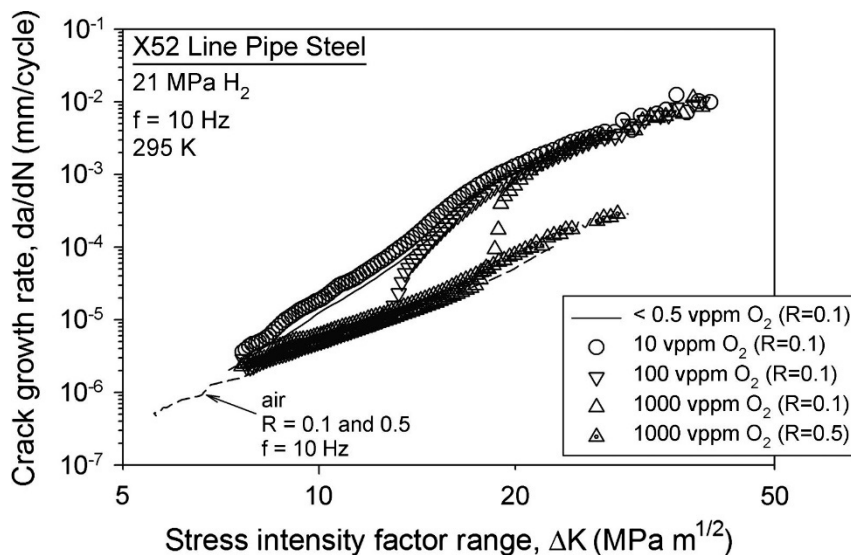


**Figure 83: FCGR vs.  $\Delta K$  for X52 pipeline steel tested in both 21 MPa hydrogen gas ( $R=0.1$ ) and a mixture of hydrogen and oxygen ( $R=0.1$  or  $0.5$ ) [173].**

### 6.3.6 Effect of Temperature

The temperature dependence of FCGR in low- to high pressure hydrogen is an important issue in achieving a comprehensive understanding of the mechanisms. Only recently, experimental results with different test temperatures from high-pressure hydrogen gas has been reported.

The work by Matsuoka et al. [165, 185] was the first investigation of temperature dependence of hydrogen-enhanced fatigue crack growth (HEFCG) of low carbon steel in high pressure hydrogen gas. FCGR test were performed at 0.7-90 MPa hydrogen pressure in the temperature range 298 k to 423 K of a low carbon steel (JIS-SM490B).

As shown in Figure 84, the temperature dependence on HEFCGR was most prominent at the lowest gas pressure, i.e. 0.7 MPa and at room temperature. With increasing temperature, the hydrogen influence on FCGR decreased. For example, at  $\Delta K=25$  MPa $\sqrt{m}$ , the relative FCGR in hydrogen gas compared to that in air (the acceleration factor),  $(da/dN)_H/(da/dN)_{air}$ , decreased with a factor of 11 from 298 K to 423 K. On the other hand, in high-pressure hydrogen (90 MPa), the HEFCG was nearly insensitive to temperature (298 K and 393 K). The temperature independency was interpreted in terms of "trap-site occupancy" of hydrogen, i.e. most of the trap sites were occupied by hydrogen regardless of temperature at the highest pressure.

The FCGR acceleration seen at RT in 0.7 and 90 MPa hydrogen gas, reveal a different striation morphology compared to that observed in air and at 0.7 MPa hydrogen gas at 423 K. As shown in Figure 85, the fatigue crack is straighter and more localized (Figure 85 (a-b) and (e-f)), compared to the morphology exhibited from tests in air. Moreover, the striations formed in the presence of hydrogen exhibit a less distinct character, attributed to the lack of blunting during the loading process, instead the crack maintains a sharp tip.

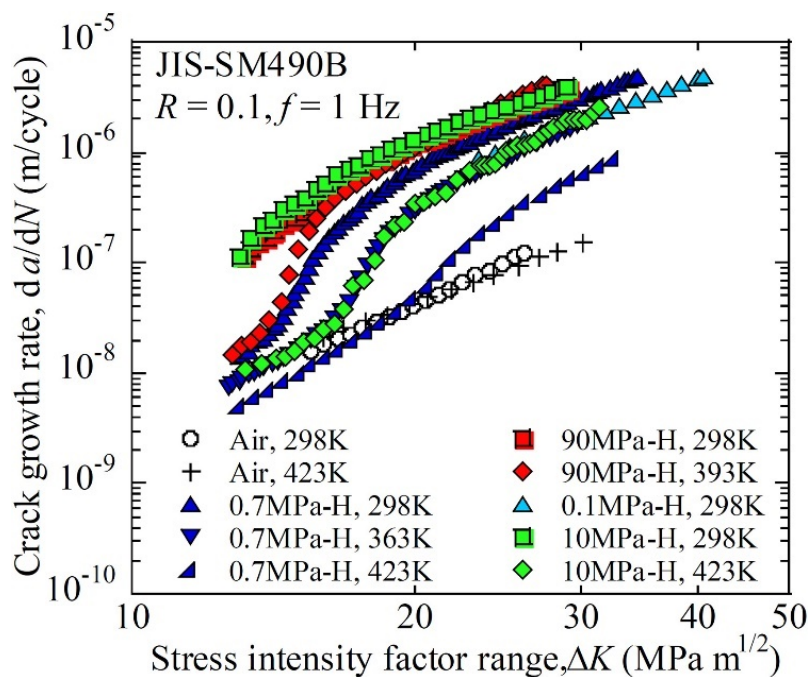


**Figure 84: Fatigue crack growth rates for a low carbon steel (JIS-SM490B) in air and 0.7- 90 MPa hydrogen pressures at temperatures from 298K to 423K [185].**

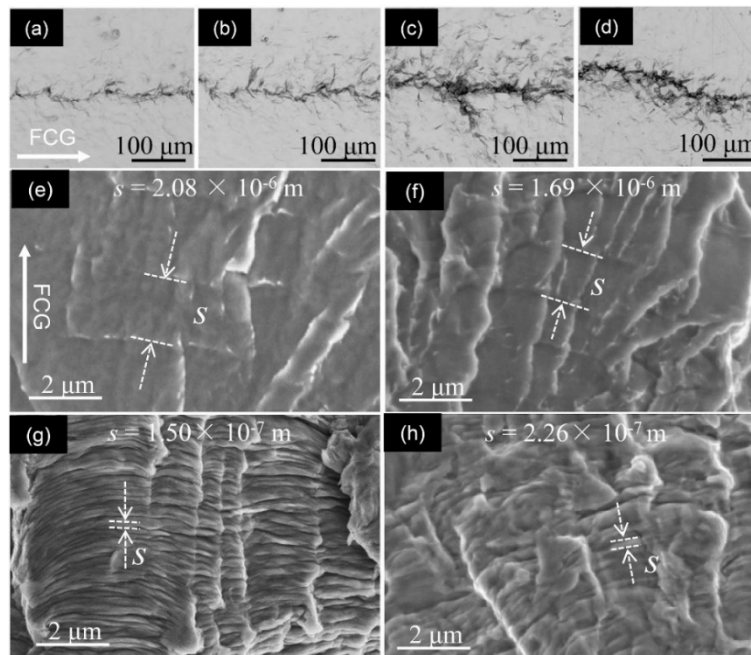


**Figure 85: SEM micrographs of (a)-(d) crack path and (e)-(h) the fracture surface at  $K=30 \text{ MPa}\sqrt{\text{m}}$ , (a) and (e) in 0.7 MPa hydrogen gas at 298 K; (b) and (f) at 90 MPa hydrogen gas at 298 K; (c) and (g) in air at 298 K; (d) and (h) in 0.7 MPa hydrogen gas at 423 K.**

Fassina et al. [186] investigated hydrogen influence in a X65 pipeline steel at low temperatures using electrochemical charging and fatigue propagation tests at various frequencies. The hydrogen diffusivity is suggested to be the most important parameter to explain the temperature effect on the fatigue crack propagation rate.

### 6.3.7 FCGR of Pipeline HAZ

The fatigue crack growth rate vs stress-intensity factor range relationship is an important for assessing the integrity of pipeline steel. The ASME B31.12 code for steel hydrogen pipelines requires testing of base metal, weld and the heat-affected zone. However, there is still a gap in available information of fatigue performance of steel welds and the HAZ.

A recent study by Drexler et al [187], determined the fatigue crack growth rate in several welds and associated heat-affected zones (HAZ's) for X70 and X52 pipeline steel in hydrogen gas to which area of the pipe that was most vulnerable to fatigue when exposed to hydrogen gas. Tests were performed at  $R=0.5$ , frequency of 1 Hz in air and hydrogen with a pressure of 5.5 MPa and 34 MPa. The results indicated that either the weld metal or their HAZ's are substantially more susceptible to fatigue crack growth in hydrogen than the base metal. The variations between FCGR in HAZ and BM's that were observed was attributed to the microstructure where the crack propagated.

In particular, the HAZ from the X52 vintage steel (similar material as referred to in section 7.3.2. from the work by [40]) exhibited higher FCGR than the weld and base metal. This was mainly

attributed to the high carbon content in the alloy, which resulted in formation of martensite at the fusion line between WM and HAZ. Local presence of martensite are shown to highly increase the risk of hydrogen embrittlement [5] and may thus increase the FCGR in HAZ well above banded microstructures in base metals.

### 6.3.8 Representative FCGR Curves for Pipeline Steel

Fatigue crack growth rate data from relevant pipeline steels are presented below [188]:

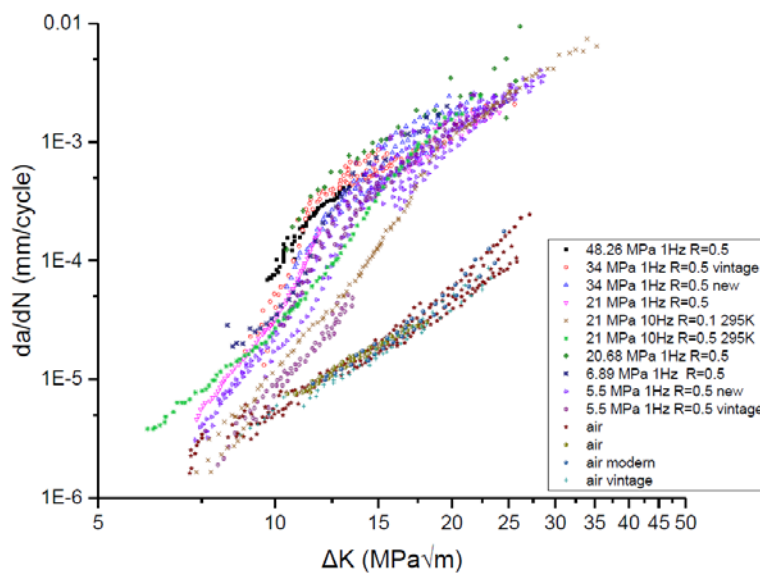


Figure 86: Fatigue crack growth data for X52 pipeline steel [155, 189, 190].

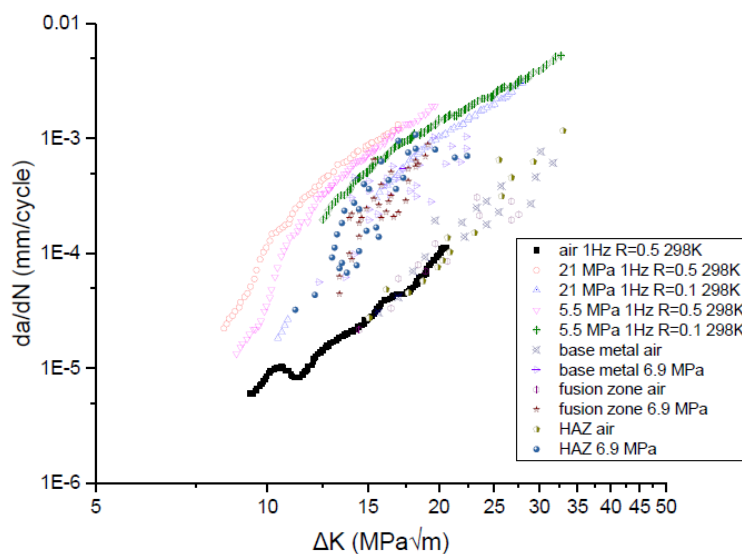


Figure 87: Fatigue crack growth data for X60 pipeline steel [113].

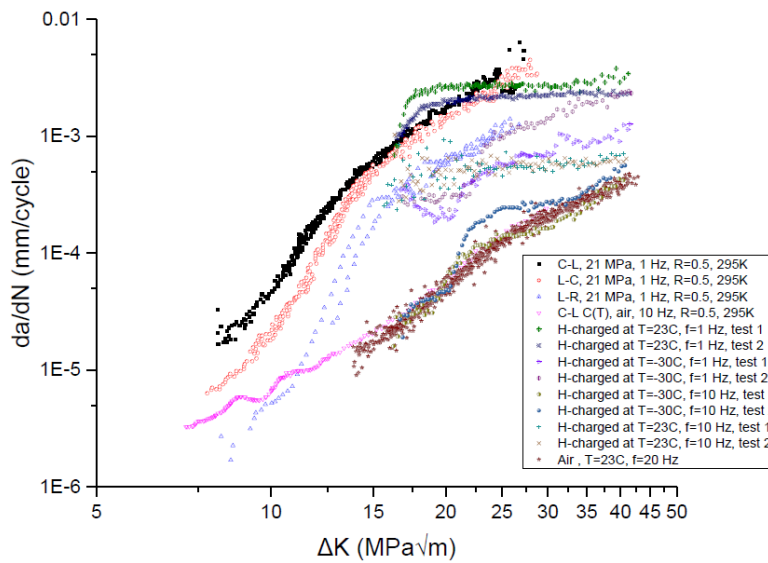


Figure 88: Fatigue crack growth data for X65 pipeline steel [182, 191].

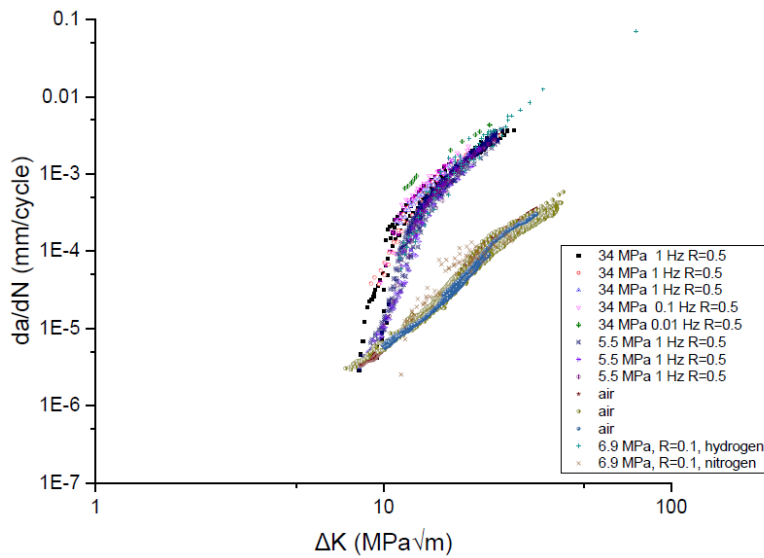


Figure 89: Fatigue crack growth data for X70 pipeline steel [81, 155, 177].

## A Chemical composition of reviewed materials

Steel	From	C	Si	Mn	P	S	Fe	Other	Ref
<b>A333 Grade 6</b>		0.11	0.25	1.21	0.010	0.002			[138]
<b>JIS-SM490B</b>		0.16	0.44	1.43	0.017	0.004	Bal		[165]
<b>A516 Gr. 70 (US grade)</b>	2.5 cm plate	0,21	0,21	1,04	0,0012	0,020	Bal		[79, 108]
<b>Alloy D (X60)</b>	plate	<b>0.03</b>	0.18	1.14	0.008	0,001	Bal	0.16 Cr, 0.14 Ni, 0.084 Nb, 0.034 Al, 0.014 Ti	[113]
<b>Alloy B (X80)</b>	plate	0,05	0,18	1,52	0,007	0,003	Bal	0.25 Cr, 0.14 Ni, 0.092 Nb, 0.036 Al, 0.012 Ti	[113]
<b>API 5L Grade B</b>		0,18		1,06					[111]
<b>SA – 105 Gr.II</b>	Hemisphere OD=59cm ID=37cm	0.23	0.15	0.62	0.010	0.015	bal		[161]
<b>1020</b>	3.8 cm plate	0.17	-	0.47	0.011	0.037	bal		[164]

## 7 Bibliography

1. Johnson, W.H., *On some remarkable changes produced in iron and steel by the action of hydrogen and acids*. Proceedings of the Royal Society of London, 1875. **23**: p. 168-179.
2. Liu, M.A., et al., *Microstructural influence on hydrogen permeation and trapping in steels*. Materials & Design, 2019. **167**: p. 107605.
3. Park, J.H., M.-s. Oh, and S.J. Kim, *Effect of bainite in microstructure on hydrogen diffusion and trapping behavior of ferritic steel used for sour service application*. Journal of Materials Research, 2017. **32**(7): p. 1295-1303.
4. Liou, H.Y., S.C. Wang, and R.I. Hsieh, *The influence of microstructure on the hydrogen embrittlement in a low carbon steel*. 1994: NACE International, Houston, TX (United States). Medium: X; Size: pp. 11, Paper 224.
5. Davis, C.L. and J.E. King, *Cleavage initiation in the intercritically reheated coarse-grained heat-affected zone: Part I. Fractographic evidence*. Metallurgical and Materials Transactions A, 1994. **25**(3): p. 563-573.
6. Woodtli, J. and R. Kieselbach, *Damage due to hydrogen embrittlement and stress corrosion cracking*. Engineering Failure Analysis, 2000. **7**(6): p. 427-450.
7. Johnsen, R., B.r. Nyhus, and S. Wästberg, *Hydrogen Induced Stress Cracking (HISC) of Stainless Steels Under Cathodic Protection in Seawater: Presentation of a New Test Method*. 2009. 55-67.
8. Christmann, K., *Hydrogen Adsorption on Metal Surfaces*, in *Atomistics of Fracture*, R.M. Latanision and J.R. Pickens, Editors. 1983, Springer US: Boston, MA. p. 363-389.
9. Sieverts, A., *Die Löslichkeit von Wasserstoff in Kupfer, Eisen und Nickel*, in *Zeitschrift für Physikalische Chemie*. 1911. p. 591.
10. Jiang, D.-e. and E. Carter, *Diffusion of interstitial hydrogen into and through bcc Fe from first principles*. Phys. Rev. B, 2004. **70**.
11. Hirth, J.P., *Effects of hydrogen on the properties of iron and steel*. Metallurgical Transactions A, 1980. **11**(6): p. 861-890.
12. Jiang, D.-e. and E. A. Carter, *Diffusion of interstitial hydrogen into and through bcc Fe from first principles*. Vol. 70. 2004.
13. Griessen, R., *Heats of solution and lattice-expansion and trapping energies of hydrogen in transition metals*. Physical Review B, 1988. **38**(6): p. 3690-3698.
14. Philipp, S., et al., *Correlation between the Electrostatic Potential and the Occupation of Interstitial Sites by Hydrogen in Metallic Systems*. Berichte der Bunsengesellschaft für physikalische Chemie, 1992. **96**(11): p. 1639-1645.
15. Park, G.T., et al., *Effect of microstructure on the hydrogen trapping efficiency and hydrogen induced cracking of linepipe steel*. Corrosion Science, 2008. **50**(7): p. 1865-1871.
16. Lan, L., et al., *Hydrogen permeation behavior in relation to microstructural evolution of low carbon bainitic steel weldments*. Corrosion Science, 2016. **112**: p. 180-193.
17. Mehrer, H., *Diffusion in solids: fundamentals, methods, materials, diffusion controlled processes*. Vol. 155. 2007: Springer Science & Business Media.

18. Li, J.C.M., R.A. Oriani, and L.S. Darken, *The Thermodynamics of Stressed Solids*, in *Zeitschrift für Physikalische Chemie*. 1966. p. 271.
19. Oriani, R.A., *The diffusion and trapping of hydrogen in steel*. *Acta Metallurgica*, 1970. **18**(1): p. 147-157.
20. Turk, A., et al., *Grain boundary carbides as hydrogen diffusion barrier in a Fe-Ni alloy: A thermal desorption and modelling study*. *Materials & Design*, 2018. **160**: p. 985-998.
21. West, A.J. and M.R. Louthan, *Dislocation transport and hydrogen embrittlement*. *Metallurgical Transactions A*, 1979. **10**(11): p. 1675-1682.
22. Pressouyre, G.M., *Trap theory of Hydrogen embrittlement*. *Acta Metallurgica*, 1980. **28**(7): p. 895-911.
23. Ohaeri, E., U. Eduok, and J. Szpunar, *Hydrogen related degradation in pipeline steel: A review*. *International Journal of Hydrogen Energy*, 2018. **43**(31): p. 14584-14617.
24. Koyama, M., et al., *Recent progress in microstructural hydrogen mapping in steels: quantification, kinetic analysis, and multi-scale characterisation*. *Materials Science and Technology*, 2017. **33**(13): p. 1481-1496.
25. Tien, J., et al., *Hydrogen transport by dislocations*. *Metallurgical Transactions A*, 1976. **7**(6): p. 821-829.
26. Maroef, I., et al., *Hydrogen trapping in ferritic steel weld metal*. *International Materials Reviews*, 2002. **47**(4): p. 191-223.
27. Myers, S.M., et al., *Hydrogen interactions with defects in crystalline solids*. *Reviews of Modern Physics*, 1992. **64**(2): p. 559-617.
28. Kumnick, A.J. and H.H. Johnson, *Deep trapping states for hydrogen in deformed iron*. *Acta Metallurgica*, 1980. **28**(1): p. 33-39.
29. Bilotta, G., et al., *Experimental measurement of out-of-plane displacement in crack propagation under gaseous hydrogen*. *International Journal of Hydrogen Energy*, 2017. **42**(15): p. 10568-10578.
30. Djukic, M.B., et al., *The synergistic action and interplay of hydrogen embrittlement mechanisms in steels and iron: Localized plasticity and decohesion*. *Engineering Fracture Mechanics*, 2019. **216**: p. 106528.
31. Troiano, A.R., *The Role of Hydrogen and Other Interstitials in the Mechanical Behavior of Metals*. *Metallography, Microstructure, and Analysis*, 2016. **5**(6): p. 557-569.
32. Oriani, R.A., *A mechanistic theory of hydrogen embrittlement of steels*. *Berichte der Bunsengesellschaft für physikalische Chemie*, 1972. **76**(8): p. 848-857.
33. *Hydrogen Induced Cracking Mechanisms — Are There Critical Experiments?*, in *Hydrogen Effects in Materials*.
34. Birnbaum, H.K. and P. Sofronis, *Hydrogen-enhanced localized plasticity—a mechanism for hydrogen-related fracture*. *Materials Science and Engineering: A*, 1994. **176**(1): p. 191-202.
35. Robertson, I.M., H.K. Birnbaum, and P. Sofronis, *Chapter 91 Hydrogen Effects on Plasticity*, in *Dislocations in Solids*, J.P. Hirth and L. Kubin, Editors. 2009, Elsevier. p. 249-293.
36. Martin, M.L., I.M. Robertson, and P. Sofronis, *Interpreting hydrogen-induced fracture surfaces in terms of deformation processes: A new approach*. *Acta Materialia*, 2011. **59**(9): p. 3680-3687.
37. Sofronis, P. and I.M. Robertson, *Viable Mechanisms of Hydrogen Embrittlement—A Review*. *AIP Conference Proceedings*, 2006. **837**(1): p. 64-70.



38. Mohtadi-Bonab, M.A., et al., *The mechanism of failure by hydrogen induced cracking in an acidic environment for API 5L X70 pipeline steel*. International Journal of Hydrogen Energy, 2015. **40**(2): p. 1096-1107.
39. 5L, A.S., *Specification for Line Pipe*. 42 ed. 2000, USA: American Petroleum Institute.
40. Slifka, A.J., et al., *Fatigue Measurement of Pipeline Steels for the Application of Transporting Gaseous Hydrogen I*. Journal of Pressure Vessel Technology, 2017. **140**(1): p. 011407-011407-12.
41. Quispe-Avilés, J.M., et al., *A Comparative Investigation of the Corrosion Resistance and HIC Susceptibility of API 5L X65 and API 5L X80 Steels*. Materials Research, 2019. **22**.
42. Yoo, J.-Y., et al., *New Development of High Grade X80 to X120 Pipeline Steels*. Vol. 26. 2011. 154-160.
43. Witek, M., *Possibilities of using X80, X100, X120 high-strength steels for onshore gas transmission pipelines*. Journal of Natural Gas Science and Engineering, 2015. **27**: p. 374-384.
44. El-Danaf, E., et al., *Mechanical, microstructure and texture characterization of API X65 steel*. Materials & Design, 2013. **47**: p. 529-538.
45. Adamczyk, J., *Development of the microalloyed constructional steels*. Journal of Achievements in Materials and Manufacturing Engineering, 2006. **14**(1-2): p. 9-20.
46. Li, X.L., et al., *Precipitation strengthening in titanium microalloyed high-strength steel plates with new generation-thermomechanical controlled processing (NG-TMCP)*. Journal of Alloys and Compounds, 2016. **689**: p. 542-553.
47. Silva, S.C.d., et al., *Cracking mechanism in API 5L X65 steel in a CO<sub>2</sub>-saturated environment*. Engineering Failure Analysis, 2019. **99**: p. 273-291.
48. Sage, A.M., *Physical metallurgy of high-strength, low-alloy line-pipe and pipe-fitting steels*. Metals Technology, 1983. **10**(1): p. 224-233.
49. Ghosh, G., et al., *Hydrogen induced cracking of pipeline and pressure vessel steels: A review*. Engineering Fracture Mechanics, 2018. **199**: p. 609-618.
50. Slifka, A., et al., *Fatigue Measurement of Pipeline Steels for the Application of Transporting Gaseous Hydrogen I*. Vol. 140. 2017.
51. Chatzidouros, E.V., V.J. Papazoglou, and D.I. Pantelis, *Hydrogen effect on a low carbon ferritic-bainitic pipeline steel*. International Journal of Hydrogen Energy, 2014. **39**(32): p. 18498-18505.
52. Godefroid, L.B., et al., *Microstructure and mechanical properties of two Api steels for iron ore pipelines*. Materials Research, 2014. **17**: p. 114-120.
53. Thewlis, G., *Classification and quantification of microstructures in steels*. Materials Science and Technology, 2004. **20**(2): p. 143-160.
54. Krauss, G. and S.W. Thompson, *Ferritic Microstructures in Continuously Cooled Low- and Ultralow-carbon Steels*. ISIJ International, 1995. **35**(8): p. 937-945.
55. Wilson, E.A., *The  $\gamma$  and  $\alpha$  Transformation in Low Carbon Irons*. ISIJ International, 1994. **34**(8): p. 615-630.
56. Thompson, S., C.V. D. J, and G. Krauss, *Continuous cooling transformations and microstructures in a low-carbon, high-strength low-alloy plate steel*. Vol. 21. 1990. 1493-1507.

57. Kostryzhev, A.G., *BAUSCHINGER EFFECT IN Nb AND V MICROALLOYED LINE PIPE STEELS*, in *College of Engineering and Physical Sciences*. 2009, The University of Birmingham.
58. Boniszewski, T. and F. Watkinson, *EFFECT OF WELD MICROSTRUCTURES ON HYDROGEN-INDUCED CRACKING IN TRANSFORMABLE STEELS - 1*. *Met Mater*, 1973. **7**(2): p. 90-96.
59. Bauer, M., *Metallurgical modelling of welding. Von O. Grong, 600 Seiten, The Institute of Materials, London 1994, Materials modelling series; 557, £ 85.00, ISBN 0-901716-37-5*. *Materials and Corrosion*, 1997. **48**(3): p. 199-200.
60. Silva, R.d.A., et al., *Formation of Microphases and Constituents from Remaining Austenite Decomposition in API X80 Steel Under Different Processing Conditions*. *Materials Research*, 2015. **18**: p. 908-917.
61. Olden, V., A. Alvaro, and O.M. Akselsen, *Hydrogen diffusion and hydrogen influenced critical stress intensity in an API X70 pipeline steel welded joint – Experiments and FE simulations*. *International Journal of Hydrogen Energy*, 2012. **37**(15): p. 11474-11486.
62. Zhao, Y., et al., *The role of hydrogen in hardening/softening steel: Influence of the charging process*. *Scripta Materialia*, 2015. **107**: p. 46-49.
63. Depover, T., et al., *Assessment of the potential of hydrogen plasma charging as compared to conventional electrochemical hydrogen charging on dual phase steel*. *Materials Science and Engineering: A*, 2019. **754**: p. 613-621.
64. Brass, A.M. and J. Chêne, *Hydrogen uptake in 316L stainless steel: Consequences on the tensile properties*. *Corrosion Science*, 2006. **48**(10): p. 3222-3242.
65. Oriani, R., *The Physical and Metallurgical Aspects of Hydrogen in Metals*. Vol. 1. 1994.
66. Au, M., *High temperature electrochemical charging of hydrogen and its application in hydrogen embrittlement research*. *Materials Science and Engineering: A*, 2007. **454-455**: p. 564-569.
67. Chatzidouros, E.V., et al., *Hydrogen effect on fracture toughness of pipeline steel welds, with in situ hydrogen charging*. *International Journal of Hydrogen Energy*, 2011. **36**(19): p. 12626-12643.
68. Garber, R., I.M. Bernstein, and A.W. Thompson, *Effect of hydrogen on ductile fracture of spheroidized steel*. *Scripta Metallurgica*, 1976. **10**(4): p. 341-345.
69. Garber, R., I.M. Bernstein, and A.W. Thompson, *Hydrogen assisted ductile fracture of spheroidized carbon steels*. *Metallurgical Transactions A*, 1981. **12**(2): p. 225-234.
70. Verbeke, K., *Gaseous Hydrogen Embrittlement of Materials in Energy Technologies*. *Gaseous Hydrogen Embrittlement of Materials in Energy Technologies*, 2012: p. 31-33.
71. Dieter, G.E., *Mechanical Metallurgy*. 1988, UK: McGraw-Hill Book Company.
72. Capelle, J., et al., *Sensitivity of pipelines with steel API X52 to hydrogen embrittlement*. *International Journal of Hydrogen Energy*, 2008. **33**(24): p. 7630-7641.
73. Meliani, M.H., et al., *The Effect of Hydrogen on the Master Failure Curve of APL 5L Gas Pipe Steels*. *Procedia Engineering*, 2011. **10**: p. 942-947.
74. Elazzizi, A., et al., *The master failure curve of pipe steels and crack paths in connection with hydrogen embrittlement*. *International Journal of Hydrogen Energy*, 2015. **40**(5): p. 2295-2302.
75. Soudani, M., et al., *Reduction of hydrogen embrittlement of API 5l X65 steel pipe using a green inhibitor*. *International Journal of Hydrogen Energy*, 2018. **43**(24): p. 11150-11159.

76. Takasawa, K., et al., *Effects of grain size and dislocation density on the susceptibility to high-pressure hydrogen environment embrittlement of high-strength low-alloy steels*. International Journal of Hydrogen Energy, 2012. **37**(3): p. 2669-2675.
77. Moro, I., et al., *Hydrogen embrittlement susceptibility of a high strength steel X80*. Materials Science and Engineering: A, 2010. **527**(27): p. 7252-7260.
78. San Marchi, C. and B.P. Somerday, *Technical reference on hydrogen compatibility of materials*. 2012, Sandia National Laboratories: Livermore, CA
79. R. Hoover, W., et al., *Hydrogen compatibility of structural materials for energy storage and transmission*. Vol. 81. 1981. 29598.
80. Cialone, H.J. and J.H. Holbrook, *Microstructure and fractographic features of hydrogen-accelerated fatigue crack growth in steels*. Microstructural Science. Vol. 14. 1987, Metals Park.
81. J. Cialone, H. and J. H. Holbrook, *Sensitivity of steels to degradation in gaseous hydrogen*. STP962-EB Hydrogen Embrittlement: Prevention and Control. 1988, West Conshohocken: PA: ASTM International. 134-152.
82. Nanninga, N.E., et al., *Comparison of hydrogen embrittlement in three pipeline steels in high pressure gaseous hydrogen environments*. Corrosion Science, 2012. **59**: p. 1-9.
83. Delafosse, D. and T. Magnin, *Hydrogen induced plasticity in stress corrosion cracking of engineering systems*. Engineering Fracture Mechanics, 2001. **68**(6): p. 693-729.
84. Park, C., N. Kang, and S. Liu, *Effect of grain size on the resistance to hydrogen embrittlement of API 2W Grade 60 steels using in situ slow-strain-rate testing*. Corrosion Science, 2017. **128**: p. 33-41.
85. Mahajan, D., et al., *Study of Hydrogen Embrittlement of API X65 & X80 Pipeline Steels using Short Fatigue Cracks*. Paper No. CMT25, CORCON 2017 (17-20 September) Mumbai, India. 2017.
86. Khatib Zadeh Davani, R., R. Miresmaeili, and M. Soltanmohammadi, *Effect of thermomechanical parameters on mechanical properties of base metal and heat affected zone of X65 pipeline steel weld in the presence of hydrogen*. Materials Science and Engineering: A, 2018. **718**: p. 135-146.
87. Boukourt, H., et al., *Hydrogen embrittlement effect on the structural integrity of API 5L X52 steel pipeline*. International Journal of Hydrogen Energy, 2018. **43**(42): p. 19615-19624.
88. Laureys, A., et al., *Characterization of hydrogen induced cracking in TRIP-assisted steels*. Vol. 40. 2015.
89. Brass, A.M. and J. Chêne, *Influence of tensile straining on the permeation of hydrogen in low alloy Cr-Mo steels*. Corrosion Science, 2006. **48**(2): p. 481-497.
90. Ghosh, K.S. and D.K. Mondal, *Effect of grain size on mechanical electrochemical and hydrogen embrittlement behaviour of a micro-alloy steel*. Materials Science and Engineering: A, 2013. **559**: p. 693-705.
91. Chen, S., M. Zhao, and L. Rong, *Effect of grain size on the hydrogen embrittlement sensitivity of a precipitation strengthened Fe-Ni based alloy*. Materials Science and Engineering: A, 2014. **594**: p. 98-102.
92. Hall, E., *The deformation and ageing of mild steel: III discussion of results*. Proceedings of the Physical Society. Section B, 1951. **64**(9): p. 747.
93. Yazdipour, N., et al., *2D modelling of the effect of grain size on hydrogen diffusion in X70 steel*. Vol. 56. 2012. 49-57.

94. Yazdipour, N., D. Dunne, and E. Pereloma, *Effect of Grain Size on the Hydrogen Diffusion Process in Steel Using Cellular Automaton Approach*. Vol. 706-709. 2012. 1568-1573.
95. Ichimura, M., Y. Sasajima, and M. Imabayashi, *Grain Boundary Effect on Diffusion of Hydrogen in Pure Aluminum*. Materials Transactions, JIM, 1991. **32**(12): p. 1109-1114.
96. Krauss, G., *Steels: Processing, Structure, and Performance, Second Edition*. 2005, Materials Park: ASM International.
97. Cabrini, M., *Hydrogen Embrittlement and Diffusion in High Strength Low Alloyed Steels with Different Microstructures*. Vol. 2. 2019.
98. Xu, J., et al., *Understanding variability in mechanical properties of hot rolled microalloyed pipeline steels: Process–structure–property relationship*. Materials Science and Engineering: A, 2013. **574**: p. 94-103.
99. Lu, J. and J.A. Szpunar, *Microstructural model of intergranular fracture during tensile tests*. Journal of Materials Processing Technology, 1996. **60**(1): p. 305-310.
100. Watanabe, T., *APPROACH TO GRAIN BOUNDARY DESIGN FOR STRONG AND DUCTILE POLYCRYSTALS*. Res Mechanica: International Journal of Structural Mechanics and Materials Science, 1984. **11**(1): p. 47-84.
101. Crawford, D.C. and G.S. Was, *The Role of grain boundary misorientation in intergranular cracking of Ni-16Cr-9Fe in 360 °C argon and high-Purity water*. Metallurgical Transactions A, 1992. **23**(4): p. 1195-1206.
102. Arafin, M.A. and J.A. Szpunar, *A new understanding of intergranular stress corrosion cracking resistance of pipeline steel through grain boundary character and crystallographic texture studies*. Corrosion Science, 2009. **51**(1): p. 119-128.
103. Venegas, V., et al., *EBSD study of hydrogen-induced cracking in API-5L-X46 pipeline steel*. Scripta Materialia, 2005. **52**(2): p. 147-152.
104. Venegas, V., et al., *Role of Crystallographic Texture in Hydrogen-Induced Cracking of Low Carbon Steels for Sour Service Piping*. Metallurgical and Materials Transactions A, 2007. **38**(5): p. 1022-1031.
105. Verdeja, J.I., J. Asensio, and J.A. Pero-Sanz, *Texture, formability, lamellar tearing and HIC susceptibility of ferritic and low-carbon HSLA steels*. Materials Characterization, 2003. **50**(1): p. 81-86.
106. Latifi V, A., R. Miresmaeili, and A. Abdollah-Zadeh, *The mutual effects of hydrogen and microstructure on hardness and impact energy of SMA welds in X65 steel*. Materials Science and Engineering: A, 2017. **679**: p. 87-94.
107. T. Chandler, W. and R. J. Walter, *Effect of high pressure hydrogen on metals*. 1968.
108. Robinson, S. and R. Stoltz, *Toughness Losses and Fracture Behavior of Low-Strength Carbon-Manganese Steels in Hydrogen*. Hydrogen Effects in Metals, 1980: p. 987-995.
109. Gutierrez-Solana, F. and M. Elices, *High-pressure hydrogen behavior of a pipeline steel*. Current Solutions to Hydrogen Problems in Steels, 1982: p. 181-185.
110. Gutierrez-Solana, F. and M. Elices, *High-Pressure Hydrogen Behavior of a Pipeline Steel*. Current Solutions to Hydrogen Problems in Steels, ed. C.I.a. GM and G.M. Pressouyre. 1982, Metals Park, OH: American Society for Metals.

111. Zawierucha, R. and K. Xu, *Hydrogen pipeline steels*. MATERIALS SCIENCE AND TECHNOLOGY-ASSOCIATION FOR IRON AND STEEL TECHNOLOGY-, 2005. **3**: p. 5.
112. J. Capelle, J.G., G. Pluvinage, *Hydrogen effect on fatigue and fracture of pipe steels*, in *International Conference on Hydrogen Safety-HYSAFE ICHS*. 2008.
113. San Marchi, C., et al., *Fracture and Fatigue of Commercial Grade API Pipeline Steels in Gaseous Hydrogen*. 2010(49255): p. 939-948.
114. Lam, P.S., et al., *Literature Survey of Gaseous Hydrogen Effects on the Mechanical Properties of Carbon and Low Alloy Steels*. Journal of Pressure Vessel Technology, 2009. **131**(4): p. 041408-041408-14.
115. Hardie, D., E.A. Charles, and A.H. Lopez, *Hydrogen embrittlement of high strength pipeline steels*. Vol. 48. 2006. 4378-4385.
116. Wang, R., *Effects of hydrogen on the fracture toughness of a X70 pipeline steel*. Corrosion Science, 2009. **51**(12): p. 2803-2810.
117. Lian, C., L. Minzhi, and S. Huihe, *A study of hydrogen effect on deformation and fracture microprocess in pure iron*. Acta Metallurgica Sinica, 1981(5): p. 5.
118. Chandler, M.Q., et al., *Hydrogen effects on nanovoid nucleation in face-centered cubic single-crystals*. Acta Materialia, 2008. **56**(1): p. 95-104.
119. Chan, S. and J. Charles, *Effect of carbon content on hydrogen occlusivity and embrittlement of ferrite-pearlite steels*. Materials science and technology, 1986. **2**(9): p. 956-962.
120. Hong, G.-W. and J.-Y. Lee, *The interaction of hydrogen and the cementite-ferrite interface in carbon steel*. Journal of materials science, 1983. **18**(1): p. 271-277.
121. Tau, L. and S.L.I. Chan, *Effects of ferrite/pearlite alignment on the hydrogen permeation in a AISI 4130 steel*. Materials Letters, 1996. **29**(1): p. 143-147.
122. Xue, H.B. and Y.F. Cheng, *Characterization of inclusions of X80 pipeline steel and its correlation with hydrogen-induced cracking*. Corrosion Science, 2011. **53**(4): p. 1201-1208.
123. Zhao, M.-C., et al., *Continuous cooling transformation of undeformed and deformed low carbon pipeline steels*. Materials Science and Engineering: A, 2003. **355**(1): p. 126-136.
124. Olden, V., et al., *Application of hydrogen influenced cohesive laws in the prediction of hydrogen induced stress cracking in 25%Cr duplex stainless steel*. Engineering Fracture Mechanics, 2008. **75**(8): p. 2333-2351.
125. Scoppio, L. and M. Barteri, *Methods of hydrogen uptake measurements by electrochemical permeation test on low alloy steels*. Hydrogen transport and cracking in metals, 1994: p. 204-215.
126. Alvaro, A., V. Olden, and O.M. Akselsen, *3D cohesive modelling of hydrogen embrittlement in the heat affected zone of an X70 pipeline steel*. International Journal of Hydrogen Energy, 2013. **38**(18): p. 7539-7549.
127. Alvaro, A., V. Olden, and O.M. Akselsen, *3D cohesive modelling of hydrogen embrittlement in the heat affected zone of an X70 pipeline steel – Part II*. International Journal of Hydrogen Energy, 2014. **39**(7): p. 3528-3541.
128. Alvaro, A., et al., *Hydrogen embrittlement susceptibility of a weld simulated X70 heat affected zone under H2 pressure*. Materials Science and Engineering: A, 2014. **597**: p. 29-36.

129. Barthélémy, H., *Effects of pressure and purity on the hydrogen embrittlement of steels*. International Journal of Hydrogen Energy, 2011. **36**(3): p. 2750-2758.
130. Ogawa, Y., et al., *Unified evaluation of hydrogen-induced crack growth in fatigue tests and fracture toughness tests of a carbon steel*. International Journal of Fatigue, 2017. **103**: p. 223-233.
131. Matsuoka, S., J. Yamabe, and H. Matsunaga, *Criteria for determining hydrogen compatibility and the mechanisms for hydrogen-assisted, surface crack growth in austenitic stainless steels*. Engineering Fracture Mechanics, 2016. **153**: p. 103-127.
132. Beltrán, M.A., et al., *On the role of microstructural properties on mechanical behavior of API-X46 steel*. Procedia Structural Integrity, 2017. **3**: p. 57-67.
133. Joo, M.S., D.W. Suh, and H.K.D.H. Bhadeshia, *Mechanical anisotropy in steels for pipelines*. ISIJ international, 2013. **53**(8): p. 1305-1314.
134. Chatzidouros, E.V., et al., *Effect of hydrogen on fracture toughness properties of a pipeline steel under simulated sour service conditions*. International Journal of Hydrogen Energy, 2018. **43**(11): p. 5747-5759.
135. Chong, T.-V.S., et al., *Effects of wet H<sub>2</sub>S containing environment on mechanical properties of NACE grade C–Mn steel pipeline girth welds*. Engineering Fracture Mechanics, 2014. **131**: p. 485-503.
136. Hejazi, D., et al., *Effect of manganese content and microstructure on the susceptibility of X70 pipeline steel to hydrogen cracking*. Materials Science and Engineering: A, 2012. **551**: p. 40-49.
137. Chatzidouros, E.V., et al., *Fracture toughness properties of HIC susceptible carbon steels in sour service conditions*. International Journal of Hydrogen Energy, 2019. **44**(39): p. 22050-22063.
138. Komoda, R., et al., *Inhibitory effect of oxygen on hydrogen-induced fracture of A333 pipe steel*. Fatigue & Fracture of Engineering Materials & Structures, 2019. **42**(6): p. 1387-1401.
139. ASTM, *E1820-13*. 2014.
140. Staykov, A., J. Yamabe, and B. Somerday, *Effect of Hydrogen Gas Impurities on the Hydrogen Dissociation on Iron Surface*. International Journal of Quantum Chemistry, 2014. **114**: p. 626-635.
141. Cialone, H.J. and J.H. Holbrook, *Effects of gaseous hydrogen on fatigue crack growth in pipeline steel*. Metallurgical Transactions A, 1985. **16**(1): p. 115-122.
142. Paris, P. and F. Erdogan, *A Critical Analysis of Crack Propagation Laws*. Journal of Basic Engineering, 1963. **85**(4): p. 528-533.
143. Chowdhury, P. and H. Sehitoglu, *Mechanisms of fatigue crack growth – a critical digest of theoretical developments*. Vol. 39. 2016.
144. Ritchie, R.O., *Mechanisms of fatigue-crack propagation in ductile and brittle solids*. International Journal of Fracture, 1999. **100**(1): p. 55-83.
145. Ogawa, Y., et al., *Fatigue limit of carbon and CrMo steels as a small fatigue crack threshold in high-pressure hydrogen gas*. International Journal of Hydrogen Energy, 2018. **43**(43): p. 20133-20142.
146. Mughrabi, H., *Cyclic slip irreversibilities and the evolution of fatigue damage*. Metallurgical and Materials Transactions B, 2009. **40**(4): p. 431-453.
147. Uyama, H., et al., *Effects of hydrogen charge on microscopic fatigue behaviour of annealed carbon steels*. Fatigue & Fracture of Engineering Materials & Structures, 2006. **29**(12): p. 1066-1074.

148. Wang, R., et al., *Fatigue of copper single crystals in vacuum and in air I: Persistent slip bands and dislocation microstructures*. Materials Science and Engineering, 1984. **65**(2): p. 219-233.
149. Suresh, S. and R.O. Ritchie, *Mechanistic dissimilarities between environmentally influenced fatigue-crack propagation at near-threshold and higher growth rates in lower strength steels*. Metal Science, 1982. **16**(11): p. 529-538.
150. Sarrazin-Baudoux, C., et al., *Fatigue propagation of short and long cracks in gaseous hydrogen environment in 3.5 NiCrMoV steel*. Engineering Failure Analysis, 2016. **69**: p. 29-34.
151. Stewart, A.T., *The influence of environment and stress ratio on fatigue crack growth at near threshold stress intensities in low-alloy steels*. Engineering Fracture Mechanics, 1980. **13**(3): p. 463-478.
152. Amaro, R., et al., *Development of a Model for Hydrogen-Assisted Fatigue Crack Growth in API Pipeline Steel*. Vol. 140. 2017.
153. Shinko, T., et al., *Hydrogen-affected fatigue crack propagation at various loading frequencies and gaseous hydrogen pressures in commercially pure iron*. International Journal of Fatigue, 2019. **121**: p. 197-207.
154. T. Chandler, W. and R. J. Walter, *Effects of high pressure hydrogen on metals at ambient temperature Final report, 7 Mar. 1967 - 28 Feb. 1969*. 1969.
155. Slifka, A.J., et al., *The Effect of Microstructure on the Hydrogen-Assisted Fatigue of Pipeline Steels*. 2013(55713): p. V06BT06A009.
156. Holbrook, J.H., et al., *Effect of hydrogen on low-cycle-fatigue life and subcritical crack growth in pipeline steels*. 1982, ; Battelle Columbus Labs., OH (USA). p. Medium: X; Size: Pages: 142.
157. Chen, Y., et al., *Performance Evaluation of High-Strength Steel Pipelines for High-Pressure Gaseous Hydrogen Transportation*. 2009.
158. Amaro, R.L., et al., *Modeling the fatigue crack growth of X100 pipeline steel in gaseous hydrogen*. International Journal of Fatigue, 2014. **59**: p. 262-271.
159. Nanninga, N., et al., "A Review of Fatigue Crack Growth for Pipeline Steels Exposed to Hydrogen" N. Nanninga, A. Slifka, Y. Levy and C. White, pp. 437-452 in *J. Res. Natl. Inst. Stand. Technol.*, vol. 115, no. 6, (2010). Vol. 115. 2010. 437.
160. Stalheim, D., et al., *Microstructure and Mechanical Property Performance of Commercial Grade API Pipeline Steels in High Pressure Gaseous Hydrogen*. 2010(44212): p. 529-537.
161. J. Walter, R. and W. T. Chandler, *Cyclic-load crack growth in ASME SA-105 grade II steel in high-pressure hydrogen at ambient temperature*. 1976.
162. San Marchi, C., et al., *Fracture Resistance and Fatigue Crack Growth of X80 Pipeline Steel in Gaseous Hydrogen*. 2011(44564): p. 841-849.
163. Hval, M. and S.V. Gråberg, *Transportation of Hydrogen Gas From a Local Plant to Remote Markets via High Pressure Submarine Pipelines*. 2017(57687): p. V004T03A001.
164. Nelson, H. *On the mechanism of hydrogen-enhanced crack growth in ferritic steels*. in *Proceedings of the Second International Conference on Mechanical Behavior of Materials*. 1976.
165. Yamabe, J., et al., *Effects of hydrogen pressure, test frequency and test temperature on fatigue crack growth properties of low-carbon steel in gaseous hydrogen*. Procedia Structural Integrity, 2016. **2**: p. 525-532.

166. Vosikovskiy, O., *Fatigue crack closure in an X70 steel*. International Journal of Fracture, 1981. **17**(3): p. 301-309.
167. Yamabe, J., et al., *Hydrogen trapping and fatigue crack growth property of low-carbon steel in hydrogen-gas environment*. International Journal of Fatigue, 2017. **102**: p. 202-213.
168. Matsunaga, H., et al., *Slow strain rate tensile and fatigue properties of Cr–Mo and carbon steels in a 115 MPa hydrogen gas atmosphere*. International Journal of Hydrogen Energy, 2015. **40**(16): p. 5739-5748.
169. Ogawa, Y., et al., *Multi-scale observation of hydrogen-induced, localized plastic deformation in fatigue-crack propagation in a pure iron*. Scripta Materialia, 2017. **140**: p. 13-17.
170. Matsuo, T., S. Matsuoka, and Y. Murakami, *Fatigue crack growth properties of quenched and tempered Cr-Mo steel in 0.7 MPa hydrogen gas*. 2010.
171. Matsunaga, H., et al., *Hydrogen-enhanced fatigue crack growth in steels and its frequency dependence*. Philosophical Transactions of the Royal Society A: Mathematical, Physical and Engineering Sciences, 2017. **375**(2098).
172. Murakami, Y., et al., *Hydrogen Embrittlement Mechanism in Fatigue of Austenitic Stainless Steels*. Metallurgical and Materials Transactions A, 2008. **39**(6): p. 1327.
173. Somerday, B.P., et al., *Elucidating the variables affecting accelerated fatigue crack growth of steels in hydrogen gas with low oxygen concentrations*. Acta Materialia, 2013. **61**(16): p. 6153-6170.
174. Alvaro, A., et al., *Hydrogen Enhanced Fatigue Crack Growth Rates in a Ferritic Fe-3wt%Si Alloy*. Procedia Structural Integrity, 2018. **13**: p. 1514-1520.
175. Alvaro, A., et al., *Hydrogen enhanced fatigue crack growth rates in a ferritic Fe-3 wt%Si alloy and a X70 pipeline steel*. Engineering Fracture Mechanics, 2019: p. 106641.
176. Nakasato, F. and I. Bernstein, *Crystallographic and fractographic studies of hydrogen-induced cracking in purified iron and iron-silicon alloys*. Metallurgical Transactions A, 1978. **9**(9): p. 1317-1326.
177. Drexler, E., et al., *Fatigue crack growth rates of API X70 pipeline steel in a pressurized hydrogen gas environment*. Vol. 37. 2013.
178. Bilotta, G., et al. *Environmentally-Assisted Fatigue Crack Growth in ARMCO Iron Under High Pressure of Gaseous Hydrogen*. in *Proc. Int. Hydrog. Conf.(IHC 2016) Mater. Perform. Hydrog. Environ.* 2016.
179. Birenis, D., et al., *Interpretation of hydrogen-assisted fatigue crack propagation in BCC iron based on dislocation structure evolution around the crack wake*. Acta Materialia, 2018. **156**: p. 245-253.
180. Roy, A., et al., *Hydrogen enhanced fatigue crack growth in an HSLA steel*. Materials Science and Engineering: A, 2013. **588**: p. 86-96.
181. Krauss, G., *Steels: Processing, Structure, and Performance*. 2nd ed. 2015: ASM International.
182. Ronevich, J.A., B.P. Somerday, and C.W. San Marchi, *Effects of microstructure banding on hydrogen assisted fatigue crack growth in X65 pipeline steels*. International Journal of Fatigue, 2016. **82**: p. 497-504.
183. Slifka, A., et al., *Summary of an ASME/DOT Project on Measurements of Fatigue Crack Growth Rate of Pipeline Steels*. American Society of Mechanical Engineers, Pressure Vessels and Piping Division (Publication) PVP, 2014. **6**.



184. Drexler, E.S., et al., *FCGR of pipeline steels in pressurized hydrogen gas: A comparison of cyclic loading rates*. 2014.
185. Matsuoka, S., et al., *Peculiar temperature dependence of hydrogen-enhanced fatigue crack growth of low-carbon steel in gaseous hydrogen*. Scripta Materialia, 2018. **154**: p. 101-105.
186. Fassina, P., et al., *Effect of hydrogen and low temperature on fatigue crack growth of pipeline steels*. Engineering Fracture Mechanics, 2013. **103**: p. 10–25.
187. Drexler, E., et al., *Fatigue Testing of Pipeline Welds and Heat-Affected Zones in Pressurized Hydrogen Gas*. Journal of Research of the National Institute of Standards and Technology, 2019. **124**.
188. Che, Z., *FATIGUE CRACK GROWTH IN HYDROGEN PIPELINE STEELS*. 2018, University of Illinois: Urbana, Illinois.
189. Amaro, R., et al., *FATIGUE CRACK GROWTH OF PIPELINE STEELS IN GASEOUS HYDROGEN-PREDICTIVE MODEL CALIBRATED TO API-5L X52\**. 2012.
190. Keller, J., Someday, B. P., *Hydrogen Embrittlement of Structural Steels*, in *FY 2011 Annual Progress Report*. 2011. p. 299-302.
191. Sciuccati, A., *Mechanical behaviour of high toughness steels in extreme environments: influence of hydrogen and low temperature*. 2012, Polytechnic University of Milan, Italy.



Technology for a better society

[www.sintef.no](http://www.sintef.no)